UNIVERSIDADE BEIRA INTERIOR

G-Quadruplex Aptamer Beacon for Detection of Prostate Cancer Biomarker

André Filipe Rodrigues Miranda

Dissertação para obtenção do Grau de Mestre em
Biotecnologia
(2º ciclo de estudos)

Orientador: Prof. Doutora Carla Patrícia Alves Freire Madeira Cruz
Co-orientador: Prof. Doutor João Pedro Estrela Rodrigues Conde
Co-orientador: Prof. Doutora Virgínia Chu

junho de 2020

“I am among those who think that science has great beauty”

Marie Skłodowska Curie

For those who made me grow…

Acknowledgements

In the first place, I would to deeply thank to my supervisor, Professor Doctor Carla Cruz, for the opportunity to develop my work in your lab group, and also for stimulating to learn and make me like about science, even more.

To my co-supervisors, Professor Doctor João Pedro Conde and Professor Doctor Virginia Chu from Instituto Superior Técnico and INESC - Microsystems and Nanotechnologies, for the involvement in this work.

To Health Sciences Research Centre to provide all facilities and equipment to perform my experiments developed and presented in this dissertation, to project FCT-MIT Portugal BIODEVICE ref. MIT-EXPL/BIO/0008/2017 and the research fellowship "Rede Nacional de Ressonância Magnética Nuclear" ref. PINFRA/22161/2016-B4 funded by "Programa Operacional Competitividade e Internacionalização","Programa Operacional Regional de Lisboa", FEDER, and FCT.

A huge thank to G4 team for the enormous spirit of camaraderie, friendship and mutual aid among all, especially to Josué and Tiago for all tireless support along past year.

To Desertuna and to those who have been accompanying me for 5 years on the streets, stages and city of our country for teaching me and growing as a man and as a professional. Friendship and companionship will never be forgotten.

To my parents, for all support, patience and diary motivation. Your efforts will never be forgotten. To my little brothers, for being a daily challenge for me.

Finally, I would like to thank especially to my grandmother Adelaide, for the life example and for teaching me to fight and never give up on our dreams. You are and you will be always in my heart!

Resumo

A próstata é a maior glândula reprodutiva masculina e tem um papel importante nas vias moleculares relevantes para o sucesso da fertilização. Infelizmente, em Portugal o cancro da próstata é o cancro mais comum entre os homens, sendo assintomático em estadios iniciais. Assim é imperativo a deteção precoce da doença.

A nucleolina (NCL) é uma proteína multifuncional envolvida em múltiplos processos biológicos sob condições fisiológicas e patológicas, podendo ter várias localizações celulares. A sobre-expressão da proteína na superfície das células é apenas encontrada em células cancerosas, nomeadamente as do cancro da próstata. Assim a NCL pode ser considerada como um potencial biomarcador para o diagnóstico e tratamento do cancro da próstata. O AS411 é um aptamero capaz de reconhecer e ligar especificamente a esta proteína, e de ter um efeito terapêutico nas células cancerosas ao induzir atividade antiproliferativa. Além do uso terapêutico, a sequência pode ser utilizada na imagiologia e diagnóstico, particularmente através do desenvolvimento de aptasensores. Uma das características mais relevantes do aptamero AS1411 é a capacidade de adotar a configuração de G-quadruplex (G4), uma estrutura secundária dos ácidos nucleicos. As estruturas G4 conferem estabilização à sequência e capacidade de ligar à NCL quando adota esta estrutura.

Assim, neste trabalho é apresentada uma primeira abordagem do uso do AS1411 no diagnóstico do cancro da próstata, nomeadamente através da construção de uma sonda a partir da sequência deste aptamero designado por AS1411N5. Inicialmente foi efetuada a caracterização biofísica do AS1411-N5 a nível da estrutura e interação com o alvo, recorrendo às espectroscopias dicroísmo circular e ressonância magnética nuclear, e ensaios fluorométricos. Adicionalmente foram efetuadas experiências de microfluídica, para o uso do AS1411N5 como sonda de deteção da NCL.

Estes resultados demonstraram, que o AS1411-N5adota a estrutura G4 e é capaz de ligar especificamente e com seletividade com a NCL, mesmo em amostras biológicas.

Palavras-chave

Cancro da Próstata; G-quadruplex; Sonda; Ensaios Biofísicos; Nucleolina; Microfluídica.

Resumo Alargado

A próstata é a maior glândula reprodutiva masculina e desencadeia vias moleculares relevantes, nomeadamente para a produção de proteínas, iões e nutrientes que contribuem para o sucesso da fertilização. Além disso oferece proteção ao trato urinário. Infelizmente, em Portugal o cancro da próstata é o cancro mais comum entre os homens. A incidência deste cancro pode ter fatores hereditário ou esporádicos, resultantes do estilo de vida, sendo que em ambos se caracteriza por ser assintomático em estadios iniciais. Assim é importante a deteção precoce da doença para diminuir a mortalidade.

A NCL é uma proteína multifuncional envolvida em múltiplos processos biológicos sob condições fisiológicas e patológicas, podendo ter várias localizações celulares. O seu nome deve-se, em larga medida, ao facto de ser a proteína mais abundante no nucléolo. A sobre-expressão desta proteína, leva a alterações metabólicas que contribuem para a proliferação celular, metástase e agressividade dos tumores. Nas células cancerosas, nomeadamente as do cancro da próstata, a NCL está sobre-expressa na superfície das células. Assim a NCL pode ser considerada um potencial biomarcador para o diagnóstico e tratamento do cancro da próstata. O AS411 é um aptamero de 26 nucleótidos, reconhece e liga-se especificamente a esta proteína, apresentando efeito terapêutico nas células cancerosas ao induzir uma atividade antiproliferativa. Esta atividade é resultante do bloqueio da replicação do DNA ou da atividade citotóxica de produtos da degradação do oligonucleótido. Além do uso terapêutico, a sequência pode ser usada na imagiologia e diagnóstico, particularmente através do desenvolvimento de aptasensores. Uma das características mais relevantes é a capacidade de adotar uma configuração de G4, uma estrutura secundária dos ácidos nucleicos. As estruturas G4 conferem estabilidade à sequência e capacidade de ligar à NCL quando adota esta estrutura. Este tipo de estruturas apresentam relevância biológica nomeadamente nos telómeros e regiões oncogénicas.

Assim, neste trabalho é apresentada uma primeira abordagem do uso do AS1411 no diagnóstico do cancro da próstata, nomeadamente através da construção de uma sonda a partir da sequência do aptamero designada por AS1411N5. Para isso foi adicionada uma porção de nucleótidos e um fluoróforo em cada extremidade do aptamero.

Inicialmente foi efetuada a caracterização biofísica do AS1411-N5a nível da estrutura e interação com a NCL, recorrendo às espectroscopias dicroísmo circular e ressonância magnética nuclear, e os estudos de interação foram realizados ensaios fluorométricos,

FRET-melting e ensaios *in vitro*. Adicionalmente, recorrendo à microfluídica, foram efetuadas experiências de reconhecimento da NCL pelo AS1411N5, e outros possíveis interferente biológicos. Esta foi a primeira abordagem na translação e do uso do AS1411N5na deteção da NCL que está sobre-expressa e é circulante no cancro da próstata.

Os resultados obtidos demonstraram que o AS1411-N5 adota estrutura G4 maioritariamente com topologia paralela comprovada por dicroísmo circular e ressonância magnética nuclear. Através dos ensaios fluorométricos e FRET-melting mostrou-se que o AS1411N5 interage especificamente com NCL, em valores concordantes com os já descritos para o aptamero. Esta seletividade também foi verificada com as amostras biológicas nos ensaios microfluídicos e nos ensaios *in vitro*.

Abstract

The prostate is the major male reproductive gland involved in male fertility and plays an important role in triggering of molecular pathways relevant to fertility success. Unfortunately, in Portugal prostate cancer is the most common cancer type among men, being asymptomatic in earlier stages. Thus, is important early detection of disease.

NCL is a multifunctional protein involved in multiple biological processes under both physiological and pathological processes and can have several cellular localizations. Cell surface protein overexpression was found restricted to cancer cells, namely in prostate cancer cells. Thus, we can consider NCL as a potential biomarker for cancer diagnosis and a target for cancer treatment. The AS1411 is an aptamer capable to recognise and binds specifically NCL and have a therapeutic effect on cancer cells through of induction of antiproliferative activity. Beyond its therapeutic use, AS1411 can be used in imaging and diagnostic, particularly on aptasensors development. One of the most relevant characteristics of this aptamer is the ability to fold in a G4 conformation, a secondary structure of nucleic acids. G4 structure confers stabilization to sequence and availability to bind NCL.

Thus, in this work is presented the first approach of use AS1411 aptamer to prostate cancer diagnosis, namely through the design of molecular beacon (MB) designated by AS1411N5. Initially, biophysical characterization of AS1411-N5 was done by circular dichroism, nuclear magnetic resonance or fluorometric spectroscopies. Additionally, it was performed microfluidic experiments, to detect NCL using AS1411-N5 in biological samples.

The results demonstrated that the proposed AS1411-N5 adopt a G4 structure and it is capable to bind with specificity and selectivity NCL, even in plasma of human patients with prostate cancer.

Keywords

Prostate Cancer; G-quadruplex; Molecular Aptamer Beacon; Biophysical techniques; Nucleolin; Microfluidics.

Index

List of Figures

List of Tables

List of Acronyms

5'-UTR	5´-untranslated regions
A	Adenine
AgNOR	Argyrophilic nucleolar organizer regions
BSA	Bovine serum albumin
C	Cytosine
CD	Circular dichroism
CTC	Circulating tumour cells
CZ	Central zone
DABCYL	4-(dimethylaminoazo)benzene-4-carboxylic acid
DHT	Dihydrotestosterone
DMS	Dimethyl sulphate
DNA	Deoxyribonucleic acid
DRE	Digital rectal examination
DSC	Differential scanning calorimetry
EDTA	Ethylenediaminetetraacetic acid
EMSA	Electrophoretic mobility shift assay
ESI	Electrospray ionization
FAM	6-carboxyfluorescein
FBS	Fetal bovine serum
FRET	Fluorescence resonance energy transfer
G	Guanine
G4	G-quadruplex
IDS	Isothermal difference spectra
ITC	Isothermal titration calorimetry
K_D	Dissociation constant
LoC	Lab-on-chip
LUTS	Lower urinary tract symptoms
MAB	Molecular aptamer beacon
MALDI	Matrix-assisted laser desorption/ionization
MB	Molecular beacon
MEMS	Microelectromechanical system
MS	Mass spectrometry
NCL	Nucleolin

NMR	Nuclear magnetic resonance
NOE	Nuclear overhauser effect
PBMC	Peripheral blood mononuclear cells
PC-3	Prostate carcinoma
PCa	Prostate cancer
PCA3	Prostate cancer antigen 3
PCR	Polymerase chain reaction
PDMS	Poly-(dimethylsiloxane)
PGMEA	Propylene glycol monomethyl ether acetate
PMMA	Poly-(methylmethacrylate)
PoC	Point-of-care
PQS	Putative G-quadruplex forming sequences
PSA	Prostate-specific antigen
PZ	Peripheral zone
RBD	RNA-binding domain
RGG	Arginine-glycine-glycine
RNA	Ribonucleic acid
SELEX	Systematic evolution of ligands by exponential enrichment
STD	Saturation transfer difference
T	Thymine
TAMRA	Carboxytetramethyl rhodamine
TDS	Thermal difference spectra
T_m	Melting temperature
TRUS	Transrectal ultrasonography
TZ	Transition zone
U	Uracil
UGE	Urogenital sinus epithelium
UGM	Urogenital sinus mesenchyme

List of Publications

Submitted manuscripts (part of the dissertation)

1) Miranda A. ; Santos, T. ; Carvalho, J. ; Alexandre A. ; Jardim A. ; Caneira C. ; Vaz V. ; Pereira B. ; Godinho R.; Brito D. ; Chu, V. ; Conde, J.P. ; Cruz, C. “Aptamer-based microfluidic assay to detect nucleolin in prostate cancer”, 2020, submitted to Biotechnology and Bioengineering.

Conferences presentations (part of the dissertation)

1) Miranda, A. ; Santos, T. ; Carvalho, J. ; Chu, V. ; Conde, J.P. ; Cruz, C. - "G-Quadruplex Aptamer Beacons for the Detection of Nucleolin". XIV Annual CICS-UBI Symposium (04/07/2019).
2) Miranda, A. ; Santos, T. ; Carvalho, J. ; Chu, V. ; Conde, J.P. ; Cruz, C. - "AS1411 Derived Molecular Beacon to Nucleolin Detection". 2nd Portuguese Symposium on Research and Innovations in Urology (09/11/2019).
3) Miranda, A. ; Santos, T. ; Carvalho, J. ; Chu, V. ; Conde, J.P. ; Cruz, C. - "Molecular Beacon Derived from AS1411 for Nucleolin Detection". III International Congress in Health Sciences Research Towards Innovation and Entrepreneurship: Trends in Aging and Cancer (15/11/2019).

Submitted manuscripts (others)

1) Santos, T. ; Miranda A. ; Campello M.P. ; Paulo A. ; Salgado G. Cabrita E ; Cruz, C. “Recognition of nucleolin through interaction with RNA G-Quadruplex” 2020.

Chapter 1

Introduction

1. The Prostate

1.1 Anatomy and Physiology

The prostate is the major male reproductive gland involved in male fertility [1]. This organ provides proteins, ions and nutrients [2], forming prostatic fluid. The latter plays an important role in triggering of molecular pathways involved in ejaculation, in sperm activation and your capacitation, and also an antimicrobial protective effect on the lower urinary tract [1], [3]. Also, it is essential in processes for the fertility success, namely semen gelation, coagulation and posterior liquefaction, allowing interaction of spermatozoa with cervical mucus (coating and uncoating) [2].

This structure is a walnut-sized organ [4] located beneath the bladder, in front of the rectum and surrounds the prostatic urethra, which is the conduit for urine flow from the bladder to penile urethra [5], [6]. Figure 1 illustrates prostate localization in the male reproductive system.

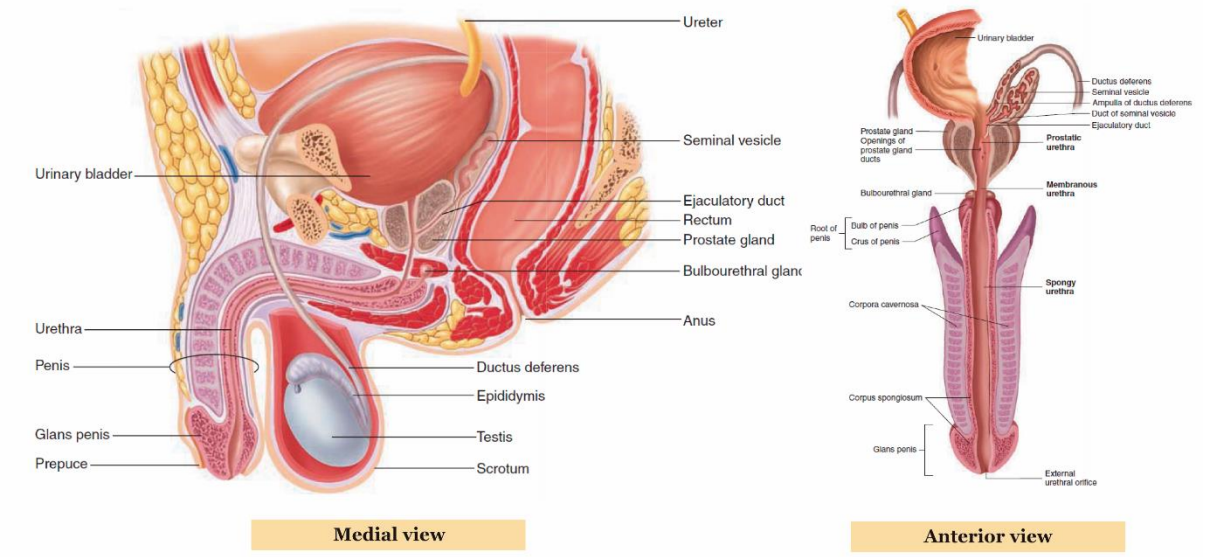

Figure 1. Medial and Anterior view of the male reproductive system showing anatomical localization of the prostate gland. Adapted from [7].

Prostate organogenesis is a complex process and can be divided into four stages: 1) Organ determination by androgens; 2) Epithelial budding of urogenital sinus

epithelium (UGE) into the surrounding urogenital sinus mesenchyme (UGM); 3) Branching morphogenesis, and 4) Cytodifferentiation [6].

Human prostate development begins about 10 to 12 weeks of gestation and is a dependent process of the action of sex steroid hormones [8]. Primarily, an androgenic stimulus, consequence of prior events, as the production of testosterone by Leydig cells of the fetal testis (around 8 weeks) [6], [9], acts to develop the embryonic precursor of the prostate, the urogenital sinus (UGS) [4].

Curiously, prostatic tissue development is not determined by fetal genetic sex, but rather by exposure to androgens. UGS from either male or female foetuses can form functional prostatic tissue if stimulated by androgens during the appropriate developmental period [2]. Thus, the absence of these hormones or appropriate receptors, due to an absent testis, lack of testicular function, or a mutation in the androgen receptor gene, the foetus will develop a female phenotype [4]. Specifically, testosterone reaches the UGS and is converted into its more potent metabolite dihydrotestosterone (DHT), under the action of 5α-reductase localized in the surrounding mesenchymal tissue [6], [8], [9]. Finally, DHT binds to an androgenic receptor and promotes prostatic genesis [8], [10].

Organogenesis of the prostate is a continuous and lengthy process under the influence of circulating androgens, since birth stage, until the organ maturation during puberty resulting of rising levels of hormones [4], [6], [10]. It should be noted that, while androgens drive the development and growth of the prostate, they also play a key role in maintaining a growth quiescent adult organ [4]. Furthermore, studies demonstrate that adult prostate remains exquisitely sensitive to the withdrawal of circulating androgens resulting in prostatic tissue atrophy [10].

When differentiated and mature, the prostate can be categorized and classified. Current nomenclature used to define the prostate are a result of centuries of studies in the anatomic field and science, in general. The anatomic model nowadays in use has been established by the American urologist John McNeal in 1981 [11]. This author divided this gland histological and anatomically, into three major glandular zones: peripheral zone (PZ), transition zone (TZ) and central zone (CZ) [4], [5], [9]–[11].

The PZ constitutes 70% of the tissues and constitutes the outer portion of the prostate (apical, posterior and lateral), being an origin site for most prostate cancers [5], [11], [12]. Already TZ surrounds the urethra proximal to the ejaculatory ducts, making up about 5% of the prostate [1], [5], [12]. Finally, the CZ is a cone-shaped region that comprises 25% of prostate volume and is not described as a place of origin of any disease process [5], [12]. Figure 2A illustrates the prostatic anatomic zones.

However, the gland has a stroma zone that surrounds epithelium [1] and is composed of fibromuscular tissue, namely smooth muscle cells mixed with fibroblasts, blood vessels and nerves [5], [6]. The main function of the stromal compartment is to ensure the appropriate microenvironment for the epithelial compartment and exhibits contractile activity to aid the expulsion of prostatic fluid into the ejaculate [1], [4], [6]. Therefore, the glandular epithelium compartment has the main function as it secretes prostatic fluid [1] and can be divided into three types of cells that differ in their function and morphology: luminal, basal and neuroendocrine [5], [6]. These cells are very particular which compared with other somatic healthy cells: are the only ones with the capacity to produce energy by glycolysis (a hallmark of proliferating cancer cells) rather than the Krebs cycle [1]. Figure 2B illustrates the cellular anatomy of the prostatic gland.

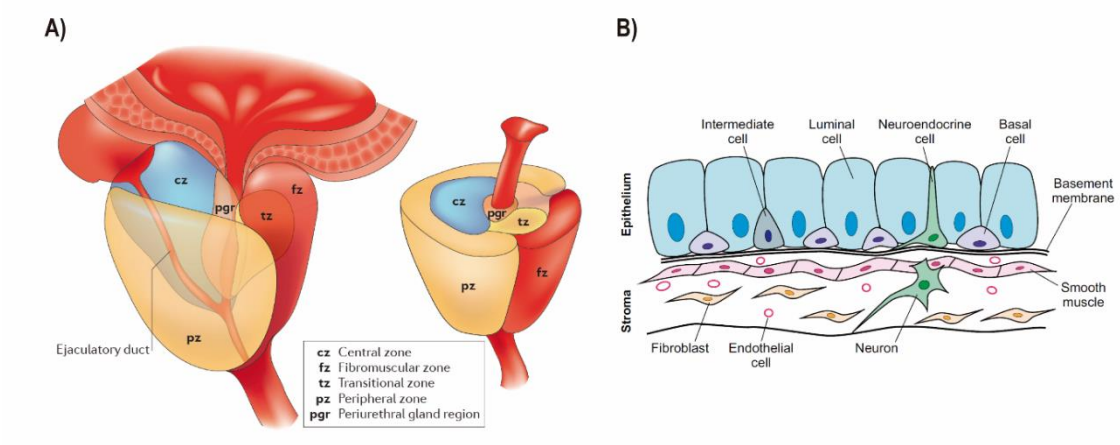

Figure 2. Anatomical and histological division of the prostate gland. A) Anatomical division of adult human prostate in distinct anatomical zones B) Differentiated cell types in adult prostate. Edited from [1], [6].

1.2 Prostate Cancer (PCa)

Cancer is considered a public health problem, and, unfortunately, are growing up worldwide, earning relevance each day. Although Europe only represents 9,85% of the total world population, it carries 23,39% of cancer cases, indeed a significant proportion [13].

Prostate cancer (PCa), like any other cancer, is characterized by abnormally dividing cells in the prostate gland resulting in aberrant growth of the organ. The higher mortality rates from PCa is due to metastasis in other areas of the body, in consequence of the migration of tumour cells to other tissues and organs [14].

According to GLOBOCAN data, and considering worldwide, PCa is the second most common noncutaneous cancer type among men (13,5%), being responsible for 358 989

death (correspondent to 6,7% of deaths by cancer) [13], [15]. Already in Portugal, PCa is the most prevalent cancer in men community [16], with a representation of 10,7% deaths, an equivalent to 1 879 persons [13], [17]. In short, approximately 1 in 8 men will be diagnosed with PCa, and 1 in 40 will die from this disease, and it is expected that until 2030 these rates increase as a result of global population growth and increased life expectancy [8]. Figure 3 shows the GLOBOCAN data representation.

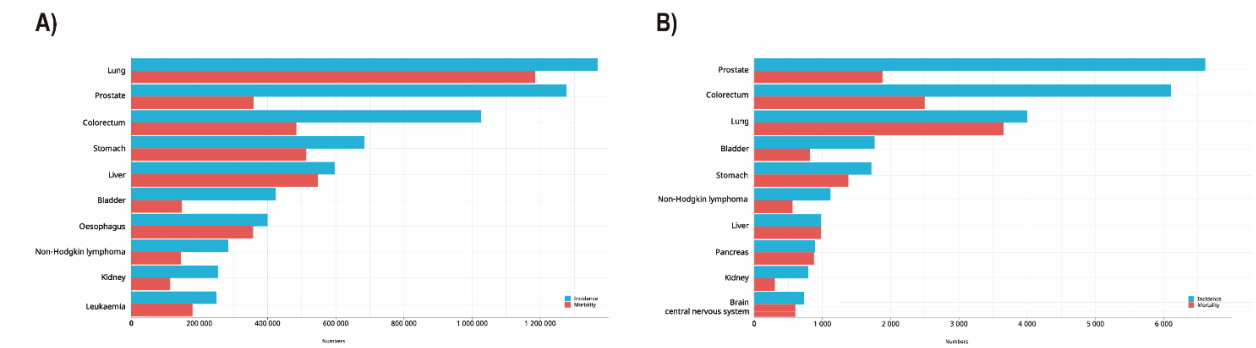

Figure 3. Cancer statistics in the World (A) and Portugal (B) in men community according to GLOBOCAN data (2018). Blue and Red bars represent tumours incidence and mortality, respectively. Adapted from [13].

However, although these values are references to cancer pathologies between countries, we cannot directly compare different countries. It is not correct and difficult. The reasons are due to the difference's health-care access, screening practices, gaps in knowledge. Also, culture has a fundamental role in rates variation, namely in awareness and attitudes toward PCa in each country, affecting a distinct application of effective national cancer control plans [8], [16], [18]. Thus, taking into account the aspects above demonstrated, can see higher incidence rates in developed countries while in developing countries the mortality rates are highest [18]. Variability in rates also can be explained by socioeconomic status, lifestyle or the prevalence of key risk factors for specific cancers between regions [8], [16].

PCa can be divided into sporadic or hereditary cancers, as a result of exposure of a combination of several exogenous and endogenous risk factors during life, like lifestyle habits, dietary, and environment, or ageing, ethnicity, genetic and endocrines factors, respectively [1], [3], [4], [19].

Research suggests the highest influence of hereditability when compared with any major cancer and that familial genetics has an important role in the origin and evolution of PCa [8], [20]. The risk to develop PCa increase according to the number of affected family members and their degree relatedness [8], [21]. Beyond this, the ability

to define hereditary PCa syndromes and identify hereditary genes associated with PCa pathology has been limited due to a significative polygenetic inheritance in the aetiology of PCa [8], [20]. Moreover, epidemiologic studies demonstrate that incidence varies by race/ethnicity, like African-Americans, experiencing the higher risk of developing PCa at any age and earlier in 73% when compared with Caucasians [8], [18], [22].

The most common age for diagnosis, on average above 60 years old, suggests that the appearance of cancer may result from changes in cellular metabolism, namely in the development of abnormalities to process reactive oxygen species, with advancing age, which impairs cell detoxification, leading to PCa disease [14].

Furthermore, lifestyle habits like smoking can be an important connection with PCa, although was not found a consistent association between them. However, has demonstrated an increase in mortality by PCa and more metastasis among current smokers [8]. Diet and obesity are also considered by your influence and alterations in normal metabolic and hormonal pathways, being important improving diet and physic exercise [3], [21].

1.3 PCa Diagnosis

According to statistics one in seven men will be diagnosed with PCa during your life [6]. Due to the initial stages of PCa typically asymptomatic [14], [19], [23], is important an efficient and prior detection of disease, to not allow carcinogenesis progression. Instead, the advanced or metastatic PCa which can present local or distant symptoms, such as bone pain and spinal cord compression or obstructive and irritative lower urinary tract symptoms (LUTS) [4], [19], [23]. The early detection of PCa allows the appropriate treatment and consequently decrease mortality and morbidity [14], [18], [19]. The survival rate varies depending on how far PCa has metastasized at the time of diagnosis: if localized, patients have a 5-year relative survival rate of almost 100%, however, drop to 31% if PCa has spread [24].

Conform American Cancer Society recommendations, PCa screening must begin at 50 years old, for average-risk men, and before 50 years of age for high-risk groups [8], [24].

The most common PCa screening tests are prostate-specific antigen (PSA) quantification in blood and digital rectal examination (DRE), and due to widespread of tests was possible a prediction of lifelong risk of patients to develop locally advanced and metastatic disease [8], [14], [25].

PSA contribute to a dramatic increase of PCa cases [26], but, consequently made it possible a curative intervention or an application of active surveillance [23], resulting in decreased mortality (40%) and reduction of advanced-stage disease (75%) [8], [25]. Active surveillance has defined as an alternative to therapy for PCa, and allow a decreasing of the overdiagnosis, overtreatment negative effects and inadequate therapies in benign disease or advanced metastatic PCa [14], [15], [22].

PSA is a glycoprotein from the kallikrein family [14], produced by prostatic epithelial cells, being the most well-known PCa tumour marker [8], [22]. Physiologically have a role in the dissolution of the gel-forming proteins (semenogelin and fibronectin) in the ejaculated semen [23]. This prostatic protein, it is gland specific but not PCa-specific, because it is present both in normal and cancerous cells, in small and elevated quantities, respectively. Also, levels can be elevated by other pathologic conditions, promoted by a disruption of cellular architecture (basal layer) such as benign prostate hyperplasia (BPH), LUTS inflammation and trauma [8], [23]. These lack of specificity and sensitivity are considered a disadvantage and the cause of false-positive and false-negative tests [14], [19].

Usually, the upper limit of normal PSA levels is 4 ng/mL, but this value can include patients with PCa or other's pathologies [19], [25], [27]. Besides, clinicians observed a variation in the PSA quantity according to age, race and prostate volume [8]. Following values in Table 1 present an age-specific reference ranges for PSA in serum.

Table 1. Reference ranges of serum PSA according to the age of men [23].

Age range	PSA reference range
40-49	0 – 2.5 ng/mL
50-59	0 – 3.5 ng/ mL
60-69	0 – 4.5 ng/ mL
70-79	0 – 6.5 ng/ mL

Commonly, PSA testing is followed by DRE [23], [27]. The DRE enabling the size of the prostate gland and allows detection of nodules, and evaluate possible extensions of the tumour to neighbour organs, being an essential part of the urological examination [19]. PCa can be detected by DRE even in the early disease stage through the palpation of a firm nodule, however, when the physician feels irregular and distorted anatomy, it is suggestive of advanced disease [23]. Experience of examiner has a role in reliability, reproducibility and effective detection of PCa [8]. Additionally, perform this diagnostic method reveal great importance in the complement of PSA test and on mitigation of false-negatives [23]. Although the serum PSA level can increase due DRE the change in

values falls within the standard error of the assay and rarely causes false-positive test results [8]. Thus, used PSA and DRE in a complementarity form will improve the detection rate [21].

Beyond biochemistry techniques, several methods and technologies for the detection of PCa are available, such as transrectal ultrasonography (TRUS), magnetic resonance imaging (MRI), radionuclide imaging (RI), computed tomography (CT), colour ultrasonography with power Doppler, positron emission tomography (PET) and PET/CT [8], [14], [21].

In the case of clinical or biochemical suspicious to PCa, the diagnosis can be confirmed by a biopsy [14], [23]. Histological diagnosis of PCa is made by biopsy with guidance from imagological methods and is most commonly performed by following the TRUS and/or MRI [21]–[23]. Biopsies establish sundry parameters like volume, grade and multifocal nature of the tumour, for a better prediction of outcome [23]–[25]. However, the biopsy is an invasive procedure and can cause complications including haematuria, urinary retention, haematospermia, urinary tract infection perineal discomfort and septicaemia [23].

By this way, it is important to develop new biomarkers. The urinary prostate cancer antigen 3 (PCA3), a long non-coding RNA involved in PCa cell survival, is one of the most sensitive and specific PCa biomarker [8]. PCA3 is not detected in normal prostate tissue but exhibits a high expression level in PCa being expressed in more of 95% of the primary and metastatic cases [25], [27].

The PCA3 in the urine is also being assessed after prostate massage (with DRE, for example), and massage frees some prostate cells which then are caught via a urine sample for analysis [14], [19], [25].

Unlike PSA, levels of PCA3 are independent of prostate size [8]. The PCA3 score has a higher specificity than serum PSA, and higher PCA3 score is associated with a high prevalence of PCa. Nonetheless, its sensitivity is lower but results can be improved by adding PSA test [14], [27].

2. Nucleic Acids

Nucleic acids are macromolecules that store, transmit and express the genetic information of a cell. These molecules are formed by elementary units called nucleotides (Figure 4), resulting from phosphorylation of a nucleoside (constituted by a pentose linked by a glycosidic bond to nitrogenous base) [28], [29]. The pentoses (sugars) can appear in 2-deoxy-D-ribose or D-ribose form, if are a deoxyribonucleic acid (DNA) or ribonucleic acid (RNA), respectively, being the key factor to define nucleic acid. Already the nitrogenous bases can be divided into purine and pyrimidine bases according to the number of carbon rings presented in their structure. Both DNA and RNA present same two purine bases Adenine (A), Cytosine (C), however, pyrimidine bases can vary between acids, being in DNA the Guanine (G) and Thymine (T), and the last, in RNA is substituted by Uracil (U) (Figure 4).

So, the nucleotide is chemically stable and adjacent nucleotides of a sequence are covalently connected among together by a phosphodiester bond between 5'-phosphate and 3'-hydroxyl of nucleotides [28], [29].

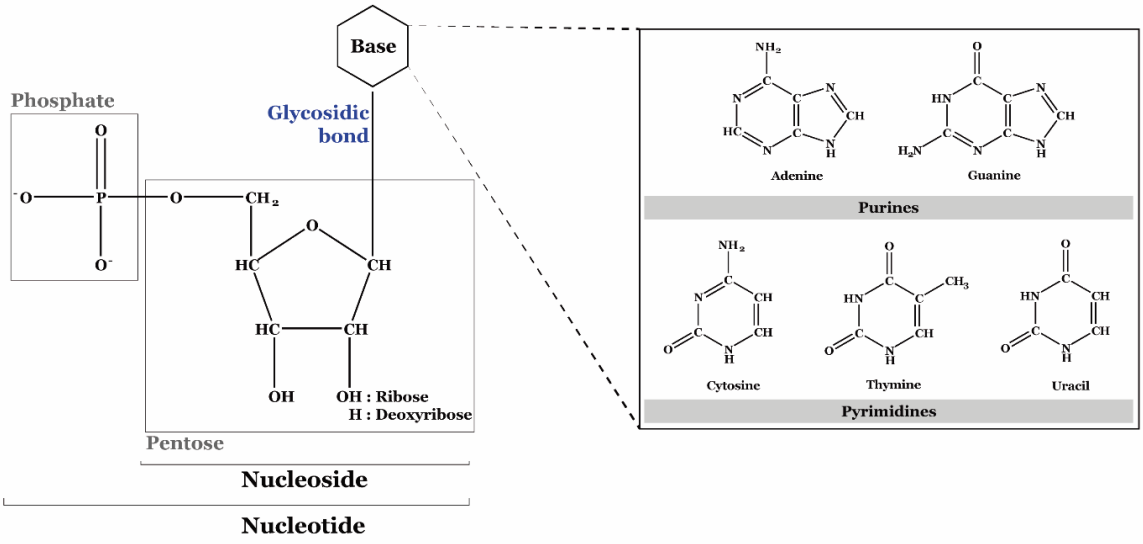

Figure 4. Elementary constitution of the basic unit of nucleic acids (nucleotides) and discrimination of nitrogenous bases according to your chemistry. Purines (A and G) present two rings, unlike Pyrimidines (C, T and U) which are composed by one ring.

2.1 Secondary Structures of Nucleic acids

After some developments in DNA study, particularly in structure, Rosalind Franklin and Maurice Wilkins used X-ray diffraction like a new approach for the study. They observed a pattern and concluded that DNA molecules are helical with two periodicities

along their long axis, a primary one of 3.4 Å (between bases) and a secondary one of 36 Å (one turn of the helix) [29].

With these information's, in 1953, James Watson and Francis Crick proposed a three-dimensional model of DNA structure consisting of two helical DNA antiparallel chains wound around the same axis to form a right-handed double helix. Additionally, they defined a pattern in nucleic acids interaction, namely which G bonds to C and A bonds specifically to T (or U), through hydrogen bonds, as the most common mode of interaction between these nucleotides and consequently nucleic acids (Fig. 5A) [28], [30].

According to the proposed model, due the nucleotide bases present a hydrophobic and insoluble profile, the hydrophilic portions of deoxyribose and phosphate groups are on the outside of the double helix, facing the surrounding water [29]. The base stacking and the interactions dipole-dipole and Van der Waals arise like an alternative to minimize contact of bases with solvent [29]. The base-stacking interactions, which are largely nonspecific, make the major contribution to the stability of the double helix and implicated in the formation of multistranded structures [29], [31].

The duplex model proposed previously, or B-form of DNA, it is the most prevalent in cellular DNA, however, DNA can be present others structural variants: A and Z forms [28], [31] described and illustrated in Figure 5B and Table 2, respectively.

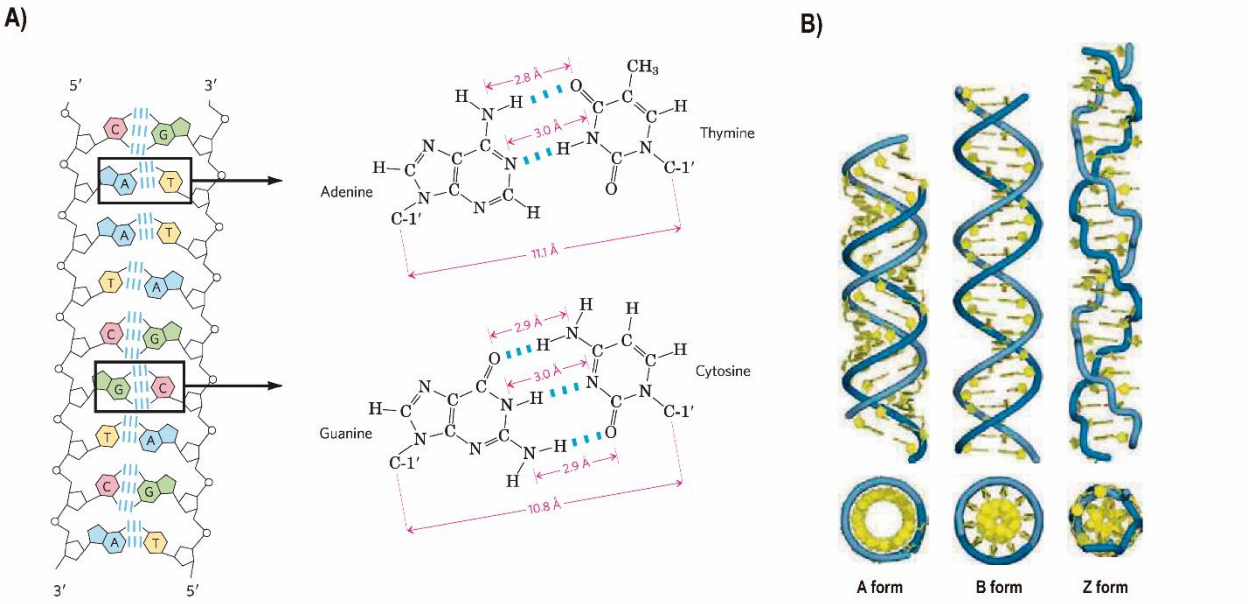

Figure 5. Illustrations of interaction between nucleotides in Watson and Crick model through of hydrogen bonds (A) and structural variants of double-helix DNA (B). Adapted from [29].

Table 2. Comparison of biophysical characteristics of double helix conformations [28], [29], [31].

	B	A	Z
Helical sense	Right-handed	Right-handed	Left-handed
Diameter	~20 Å	~26 Å	~18 Å
Base pairs per helical turn	10.5	11	12
Helix rise per base pair	~3.4 Å	~2.6 Å	~3.7 Å
Twist	36.7º	32.7º	-10/-50 º
Bases tilt normal to the helix axis	6º	20º	7º
Groove width	11.7/5.7 Å	2.7/11 Å	8.5 Å
Sugar pucker conformation	C2'	C3'	C2'/C3'
Glucosyl bond conformation	Anti	Anti	Anti/Syn

Primary structure of DNA and environmental conditions will influence the adoption of other secondary structures [31]–[33]. Phosphate groups are the most susceptible elements to the effects of solvent (salt concentrations and hydration), affecting nucleic acid structure [28].

The phenomenon's like palindromes and inverted repeats in the DNA sequence may cause mutations and consequently errors of synthesis, inducing structurally formation of bulges, a hairpin or cruciform structures [29], [31], [32].

Furthermore, it was well established that DNA can adopt alternative secondary structures to duplex [34], called non-canonical structures, through the new interactions of several chains. Nucleotides can form additional hydrogen bonds to link another chain through the Hoogsteen positions, allowing the formation of triplexes or quadruplexes [29], [33]. In the case of triplex, the third strand is included in the major groove of duplex DNA [28], [32]. Already, quadruplex associate interaction between four strands. Normally the association is made between sequences riches in G or C, leading to the formation of G quadruplexes (G4) or i-motifs [31], [34], [35].

Briefly, and since these structural configurations also are observed in the RNA's, which present a single strand, we can conclude that nucleic acids are highly polymorphic, assuming several secondary structures, always depending on external and internal factors.

Figure 6 represents the secondary's structures explained above.

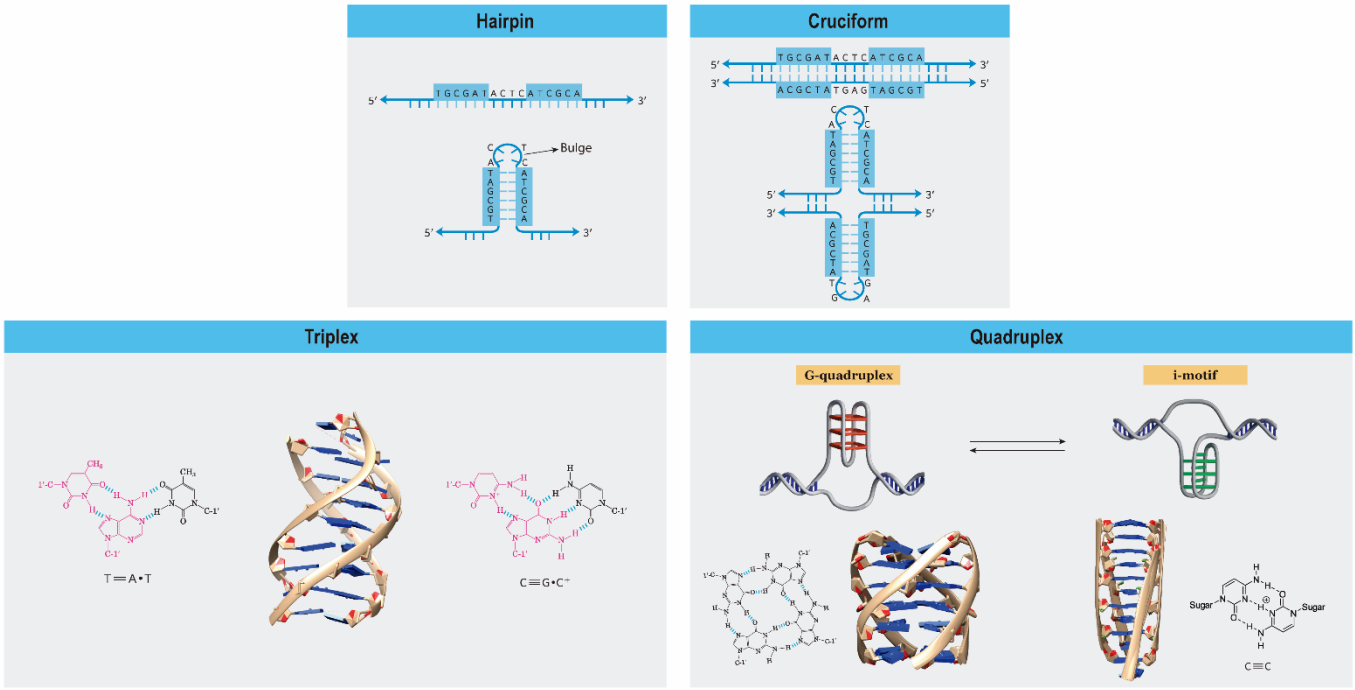

Figure 6. Schematic illustration of possible secondary structures of nucleic acids. Three-dimensional nucleic acids pictures are downloaded from Protein Data Bank (PDB) and generated by UCSF Chimera 1.12. Triplex PDB code: 134D; G-quadruplex PDB code: 2CHJ; i-motif PDB code: 2N89. Adapted from [29], [35].

2.2 G-quadruplex (G4)

Historically, at beginning of 19th century, was first described the capacity of formation of polycrystalline gels in solutions with a high-level concentration of guanosines, suggesting the capacity to form order structures and auto-association phenomena [28], [36], [37]. Just in 1962, middle century after, through crystallographic methods, Gellert and collaborators clarified the arrangement of nucleotides, namely G, and proposed a G-quartet structure, the basic motif of G4 [28], [38], [39]. Since then, this non-canonical structure has been the best studied around all secondary structures, being reported to have critical regulatory roles in biological processes (replication, transcription, and translation) as present in telomeres, gene promoter (5´-untranslated regions (5'-UTR)) and oncogenic regions [33], [34], [36], [38]–[40]. Several researchers evidence that G4's can play a role in the growth and progression of cancer, due to higher telomerase activity in cancerous cells [31], [36].

2.2.1 G4 Structure

As mentioned before, G4 is formed only by G and is resulting of stacking of G-quartets (also named G-tetraplex, G-tetrads or just tetrads). This basic structural motif, represented in Figure 7, is an outcome of linkage and stabilization via Hoogsteen

hydrogen-bonded of G to form a square co-planar [28], [31], [36]. Until now, G4 is the unique known structure resulted entirely by Hoogsteen-type base pairing [31].

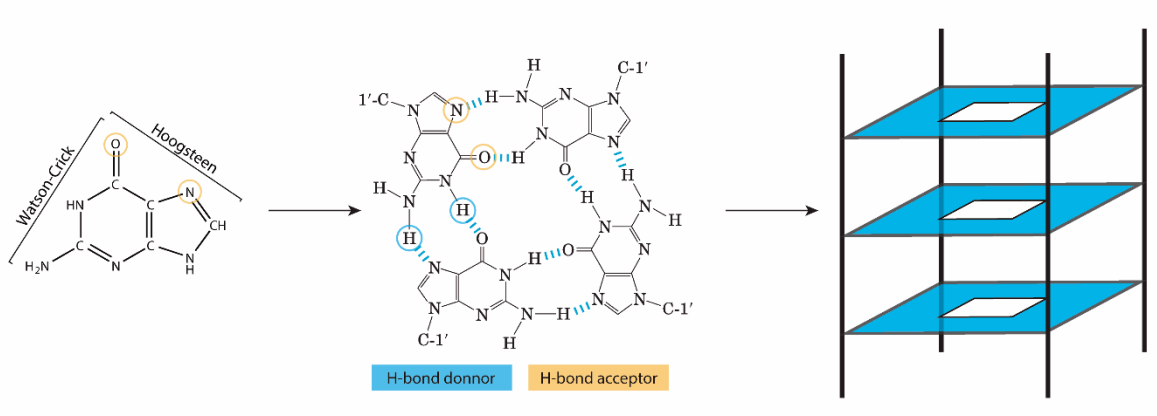

Figure 7. Illustration of G-tetrad formation through Hoogsteen bonds between G with and tetrads staking.

Hoogsteen linkage, proposed by Karst Hoogsteen in 1963, consists in an unusual pairing of guanines [29] through the utilization of both the N1 and N2 of one face with the O6 and N7 of the neighbouring guanine. These producing eight hydrogen bonds per planar tetrad and an angle of 90º between G [28], [39], [41]. G4 are stabilized intraquartet, like described above by hydrogen bonds, and interquartet, by stacking of hydrophobic quarters and cation coordination (Figure 7) [38], [41].

The self-assembly of G-tetrads is enhanced further by the hydrophobic character of square tetrads, that creates a large π-surface that favours stable π-π stacking [42]. According to X-ray studies, tetrads, when stacked, have a distance of 3.3 Å between them, forming a right-handed helix appearance due to phosphate backbones [28], [36], [39]. Helix torsion, in consequence of tetrads stacking, will confer chirality to structure, that defines the maximum of absorption in circular dichroism [42], [43].

G4s also can be stabilized by cations, preference for alkali-metal cations, located between two G-quartets and centrally coordinated to G [36], [38], [39], [44].

2.2.2 Cations

As before elucidated, cations have an important effect in G4 stabilization. Cations can bind to G4 structures through two distinct modes: a nonspecific and a specific.

The specific binding mode, suggested by Arnott *et al.*, consists on the coordination of cations to O6 of G in the G4 axial channel, involving electrostatic and donor–acceptor interactions with the free electrons of the oxygen [28], [41], [44]. Without this linkage, the nucleic acids (polyanions) arrangement would be electronically unfavourable, due

to negatives charged cavities between tetrads, thus denoting the fundamental role of chemical coordination on stabilization of G4 [37], [45].

Factors like different cation species, intrinsic properties (as size and charge) and concentration determine the folding of G4 and, consequently, its stability [28], [37]. Cations such as potassium (K^+), with larger ionic radii, locates between successive layers of quartets dissimilarly of smaller cations, and sodium (Na^+), which can coordinate within the plane of individual tetrads (Figure 8A) [37], [41].

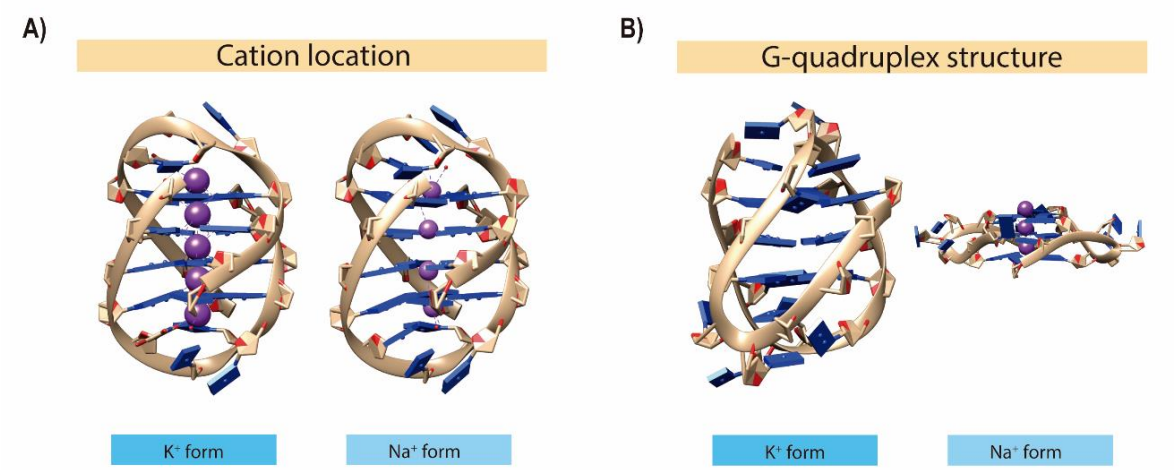

Figure 8. Cations in G4. A) Different locations of cations in G4 (between tetrads or inside tetrads) according to ionic radii in the structure (PDB entries: 1JPQ and 1JB7 to K^+ and Na^+ respectively). B) Influence of cations in topologies of quadruplex (PDB entries: 143D and 1KF1 to K^+ and Na^+ respectively). Three-dimensional pictures generated by UCSF Chimera 1.12. Adapted from [28].

A range of monovalent and divalent cations (alkali) can stabilize G4 formation in different degrees [28]. Largy *et al.* proposed a hierarchical order for G4 stabilization by cations explained in Table 3.

Table 3. Hierarchical order to stabilization and ionic radii of cations used to stabilize G4 [28], [41].

Order									
Element	**Sr^{2+}**	**K^{2+}**	**Ca^{2+}**	**NH_4^+**	**Na^+**	**Rb^+**	**$Mg2^+$**	**Li^+**	**Cs^+**
Ionic radii (Å)	1,18	1,53	0,99	1,43	1,16	1,66	0,72	0,9	1,81

The cations K^+ and Na^+ are the most used due to the physiological role and presence of them in the cells [28]. Li^+ have sometimes been considered as G4-destabilizing ions, and just like Mg^{2+}, can be considered as "indifferent/neutral" toward G4 formation and stabilization [37], [41], [46]. Nuclear magnetic resonance (NMR) titrations can be used to provide insights about the thermodynamics of the cation selectivity exhibited by G4 [44].

Ionic strength is required to compensate the electrostatic repulsion between the phosphate oxygens in a G4 structure, and cation radii can be an important factor. Fujii and colleagues revealed that metal ions bind and stabilize specific topologies with the proper size metal ion cavities [37], [47]. However, the optimal cation fitting does not explain selectivity by certain ions (K^+ and Na^+, for example) and are being suggested that electronic factors perform a role [41], [45].

The G4 positive charge core promotes hydration of G4 and reduces the electrostatic repulsions of negative phosphate groups along the backbone, induce the double helix appearance previous described [41], [44]. Like cations, small synthetic molecules, called ligands, which can be positively charged, can have a stabilizing effect on the structure of G4.

Briefly, nature and characteristics of ions and binding mode, allied to structural studies, suggest that G-rich sequences can adopt different topologies with different cations (Figure 8B) depending on their formation environments inside the cells [37], [45], [47].

2.2.3 G4 polymorphism

G4 are highly polymorphic and this structural diversity results from many intrinsic and extrinsic variables. Conformations are firstly dependent of the number of quartets and number of strands (stoichiometry), but the major source of variation comes from the polarity of strands, correlated with the glycosidic torsion angles of G. Although, the presence of cations, as explained above, pH, length and location of the loops in the nucleotide sequence can be considered other factors affect the folding [36]–[39], [41], [42], [48].

2.2.3.1 Number of Strands and Sequence

G4s can fold into distinct modes: intramolecularly or intermolecularly. In the first case, G-stacking and subsequent G4 formation occur in the same strand (unimolecular). Unlike, when G4 formation involves hybridization of two or four strands, can be classified to a class of bi- or tetramolecular structures, respectively (Figure 9) [33], [42], [49], [50].

Most biologically relevant G4s forms intramolecularly, for example in telomeres [42]. Usually, these sequences with potential to form G4 are denominated by putative G4 forming sequences (PQS) [33], [37]. A typical PQS is defined by $G_mX_nG_mX_oG_mX_pG_m$,

where *m* represents the number of G in each G-tract usually involved tetrad interactions. X_n, X_o and X_p can be any combination of nucleotides, including G, forming the loops and bulges. G-tracts can be of unequal length, and if one of the short G tracts is longer than the others, G nucleotides will be located in the loop or bulge regions [28], [42], [50], [51].

PQS needs to have at least four stretches of G residues were each comprised of at minimum guanines [33], [37]. To help the prediction of potential G4 sequences in the genome, many algorithms using PQS motifs are used. Some of these include Quad-Parser, G4P Calculator, G4 Hunter, QuadBase, QGRS Mapper and cGcC score [33], [36], [49], and revealed that the PQS are enriched or overexpressed at 5'-UTRs and promoters regions of genomes [52].

However, the prediction of intermolecular G4's is more complex because it requires consideration of both strands enfolded, length and composition[33]. Thus, bimolecular G4 is the result of the association of two identical sequences $X_n\ G_m\ X_o\ G_m\ X_p$, where *n* and p may or may not be zero. Already tetramolecular G4's are formed by the association of four strands together with the motifs $X_n\ G_m\ X_o$ or $G_m\ X_n\ G_m$ [50].

Although intramolecular G4 involves only one strand presents several and complex topologies [28]. A schematic representation of uni-, bi- and tetramolecular is presented in Figure 9.

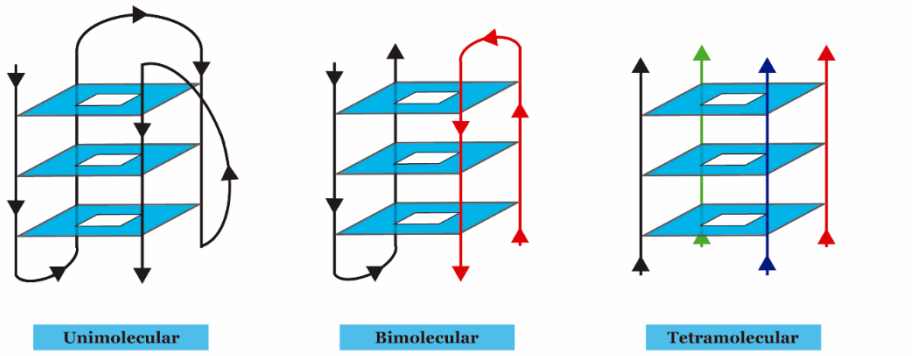

Figure 9. The number of strands in G4 folding. Intramolecular assemble just with one strand and intermolecularly assemble with two or four strands if are bimolecular or tetramolecular, respectively.

2.2.3.2 Polarity of Strands

The orientation of strands also determines the topological classification of the G4 structure. A G4 is designated parallel if the polarities of all the strands are oriented in the same direction. In contrast, if each strand has an opposite polarity concerning the two adjacent strands, the quadruplex is termed anti-parallel. However, it is possible the formation of hybrid or mixed orientations (parallel and antiparallel strand) [37], [42],

[46], [48], [51]. In the case of hybrid and anti-parallel topologies, have one and two G-tracts are anti-parallel, respectively [43], [49] [51]. All orientations topologies are represented in Figure 10A.

At the molecular level, differences in the polarity of strands are associated with the glycosidic bond angle between the G-bases and the sugars that can adopt [46] [42]. This angle can display two forms: *syn* and *anti* conformations (Figure 10B) [48].

In parallel G4 all angles have an anti glycosidic profile, causing homopolar G-tetrad stacking interactions [51], [53]. Grooves between the backbones are all of the equal sizes and running in the same direction, promoting an entirely C4 symmetric system [28], [46]. However, some studies shown if some quartets can flip from all-anti to all-syn conformations preserve parallel orientation [53].

The majority of G4s which naturally occurs adopt a parallel conformation [42], [48]. Contrarily, antiparallel or hybrid G4 topologies has both glycosidic bond angles in your structure [51]. The reversion of the strand direction induce changes in the glycosidic angle, from *anti*-to-*syn*, for the hydrogen bonds to be formed correctly, resulting in heteropolar tetrad interactions [46], [53].

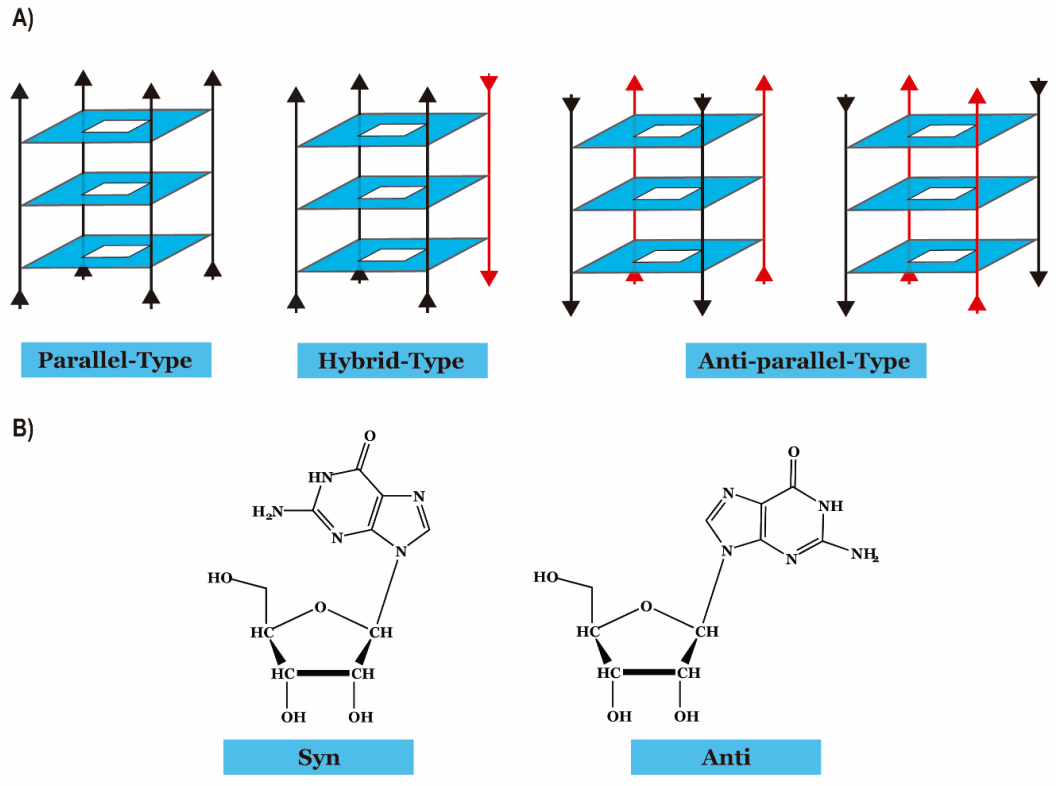

Figure 10. Conformations of G4s according to strands polarity (A) and justification of this event (B). Polarity differences are associated with an angle between the G-bases and the pentose.

2.2.3.3 Loops and Bulges

The polymorphism of G4 is also dependent on loops and bulges. Loops are sequences that connect the G-tracts on G4s [37], [43], [51], being exclusive from unimolecular and bimolecular G4.

There are different types of loops which will on the folding topology of G4 [53]. The propeller loop links the bottom G-tetrad with the top G-tetrad in adjacent parallel chains [43], [50]. Antiparallel strands are connected by lateral or diagonal loops, if G-tracts are located adjacent or opposite each other, respectively [50], [51], [53].

Lateral loops (or edge-wise loops) in bimolecular quadruplexes can be classified like head-to-tail type, when all adjacent strands are anti-parallel, or head-to-head type when adjacent strands are both parallel and anti-parallel [50]. These antiparallel loops can discriminate the G4 according to shape, dividing in chair or basket if structure presents a lateral or diagonal loop [43], [51]. Besides, the hybrid topology can differ in the order of the chains and loops and adopt two G4 hybrid forms, form-1 and form-2 (Figure 11) [43].

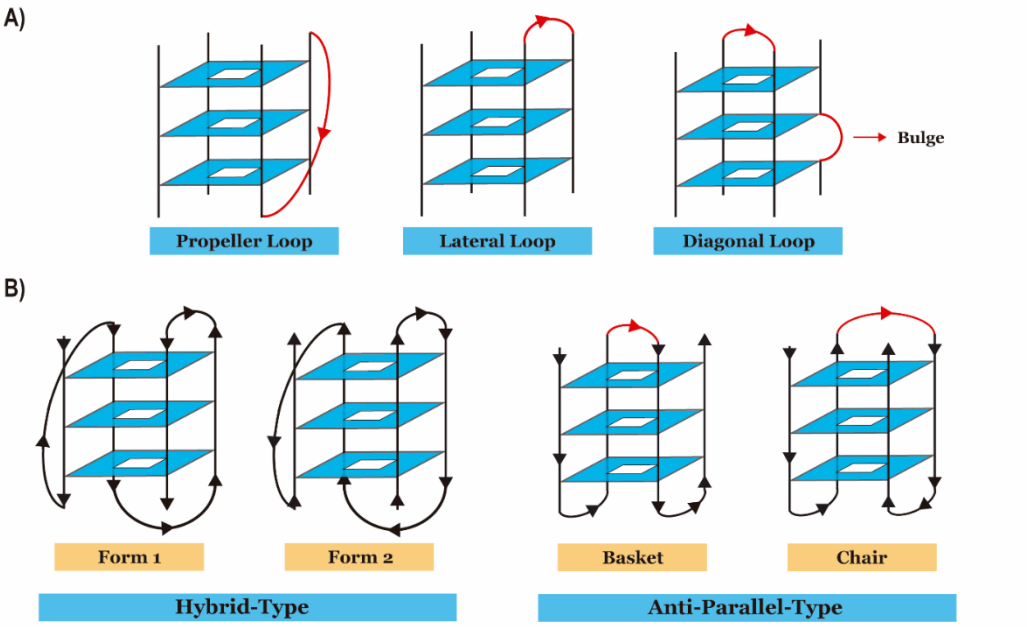

Figure 11. Loops and bulges in G4 polymorphism. Different types of loops (A) and influence in the characterization of the structure of quadruplex (B).

Nonetheless, the length and nucleotide composition of the loops play a crucial role in determining the stability of G4 structures, because the formation of favourable loop interactions has influence in topological preferences [37], [51]. The presence of long loops, formed by sequences of 3 more nucleotides in length occur predominantly in antiparallel and hybrid topologies, that is, in structures with the presence of lateral

loops [48], [51]. Curiously, these loops due to secondary interactions in the loops or interactions between loops and the G-tetrads can increase DNA-G4, however, not all loops contribute equally this. Distinctively, shorter looped structures are responsible for parallel loop formation [48].

In contrast, RNA-G4 exhibit a lower diversity of strand orientations, and all RNA strands run in a parallel orientation independent of loop length [41], [52]. This polarity is justified by the locking of the hydroxyl groups in the ribose sugar, which impose steric constraints that favour anti-conformation of G's and the facilitate formation of parallel topologies with shorter loops [37], [42], [48]. RNA G4s are more thermodynamically stable and compact structure compared to DNA, because the energy barrier for interconversion between the *syn* and *anti*-conformations is much higher for RNA than for DNA [37], [51], [53].

Additionally, and similarly to loops, some G4 structures with long sequences lengths and discontinuities between tetrads in the same strand, induce the formation of bulges (Figure 11A) [36], [41].

In the figure below, the main characteristics presented on G4 are summarized schematically (Figure 12).

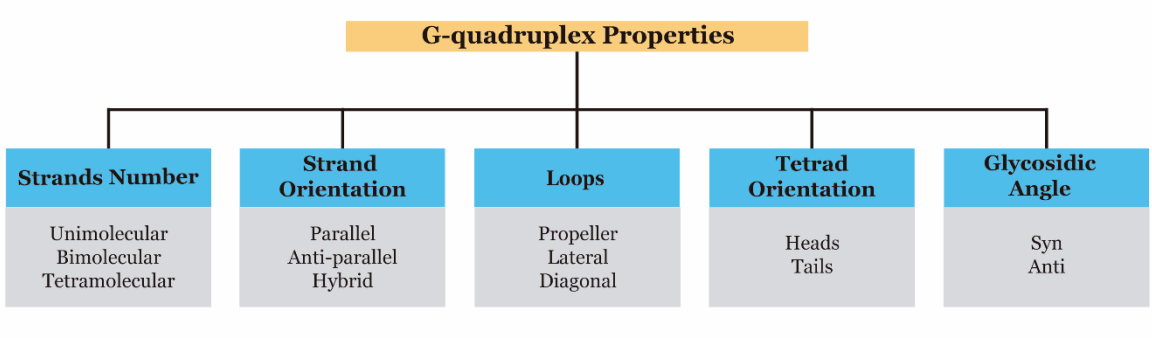

Figure 12. Schematic representation of G4 properties discussed in the present section.

2.3 AS1411 a G4 aptamer for Nucleolin

The term aptamer derives from the words "*aptus*", meaning "to fit," and the "*meros*" meaning "part" or "region", from Latin and Greek vocabulary respectively [54], [55]. In science, it is defined as a small nucleic acid that can fold into a three-dimensional structure similar to antibodies [55]. These motifs provide high affinity, selectivity and specific binding sites towards small molecules and macromolecules (cells, proteins, bacteria's and viruses) [33], [54].

Commonly, aptamers are synthesized using systematic evolution of ligands by exponential enrichment (SELEX) technology. Briefly, SELEX is an iterative process which begins with the construction of a random library of nucleic acids sequences. Each sequence is unique and contains two conserved primer binding sites, which are used for polymerase chain reaction (PCR) amplification by hybridizing primers, and a randomized region in the middle (20–50 nucleotides) [54], [55]. The traditional method involves three main steps: selection, partitioning, and amplification (Figure 13).

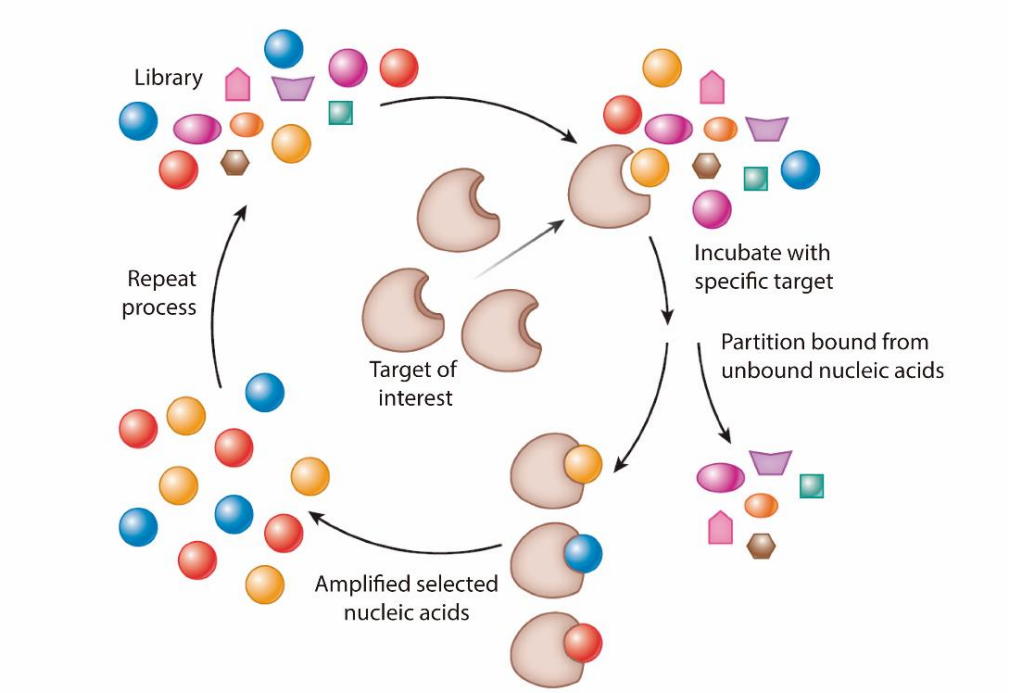

Figure 13. Systematic evolution of ligands by exponential enrichment (SELEX). Modified from [55].

In the selection step, sequences of the library are incubated with target molecules, and then, unbound nucleic acids are separated [54], [55]. The last stages are the same for both DNA and RNA; however, the amplification step will be different. The DNA, amplification of target-bound sequences is performed by polymerase chain reaction (PCR), than reverse transcription PCR in RNA [54]. In each round, the amplified molecules build a new enriched nucleic acids library, and after many rounds (8–12) sequences have a high affinity for the target, being necessary, in the final, the identification of highest affinity sequence [55].

Specifically, the aptamers formed from G-rich sequences, besides recognizing the target, are capable to fold into G4 structures and take out advantages (nucleases resistance, low immunogenicity, enhanced cellular uptake and chemical and thermodynamic stability) [33], [54].

Due to these advantages, several applications are developed since therapeutic agents for cancer therapy, aptasensors and nano-devices [54].

The AS1411 is an example of a G4-aptamer that binds specifically to protein nucleolin (NCL) (both detailed in below sections) and, interestingly, was aleatory discovered [41], [54]–[57].

2.3.1 AS1411

AS1411, formerly known as AGRO100, is an aptamer capable to fold in a G4 configuration. Was officially discovered in 2000 by Paula Bates and colleagues randomly, from the optimization of a G-rich sequence named GRO29A [58].

This aptamer is a synthetic G-rich DNA oligonucleotide with 26 nucleotides (5′-GGTGGTGGTGGTTGTGGTGGTGGTGG - 3'), and one of the most promising and studied aptamers [41], [55], [57]. Also, one of the main characteristics of this aptamer is the high degree of structural polymorphism [54], [59]. For this reason, is hard to determine the biologically relevant structure(s) and define the three-dimensional structure of AS1411. Researchers discovered that the majority of conformations displays the classical parallel quadruplex, except an unusual fraction that presents a left-handed quadruplex form (Z-G4), and they are different according to the solution content, namely with the presence of K^+ [38], [57]. Despite that, considering the number of G in sequence, we can infer the presence of four tetrads.

As previously mentioned, AS1411 recognises and binds specifically to RBD´s of NCL [56]. This binding and the formation of AS1411-NCL complex induce aptamer endocytosis and consequent inhibition of DNA replication or the arresting the cells in the S phase of interphase, resulting in cytotoxicity and antiproliferative activity in cancerous cells [38], [41], [54], [55]. Other hypotheses explain that when degraded in the presence of serum, generate cytotoxic products to cells, due G-rich based nature of products [57].

The antiproliferative activity of AS1411 was shown in several cancer cell lines such as breast, glioma, lung, and PCa cell lines [54]. Also, presented antiviral and antileukemic activity and decrease the aggressiveness of tumour and resistance to antineoplastic therapy, due to the downregulation of expression level of mRNA's [56].

Clinical trials of AS1411 (*clinicaltrials.gov* identifier: NCT01034410) for renal cell carcinoma and acute myeloid leukaemia [41] showed the ability to induce responses in patients with intractable cancers [57]. However, AS1411 have presented a disadvantage of a rapid human body clearance [54], [57].

To improve AS1411 low pharmacokinetics, modifications on the sequence were performed and generated new derivatives such as the APTA 12, AT11 and AT11-Lo (Table 4) [54]. These modifications can be through of nucleotides and chemotherapeutics insertion inside the sequence.

Table 4. Sequence comparison of AS1411 and some derivatives.

Aptamer	Sequence
AS1411	5′ - GGTGGTGGTGGTTGTGGTGGTGGTGG - 3'
APTA12	5′ - GGTGGTGGTGGTT**Z**TGGTGGTGGTGG - 3'
AT11	5′ - **T**GGTGGTGGT**T**GTTGTGGTGGTGGTGG**T** - 3'
AT11-Lo	5′ - **T**GGTGGTGGT**T**GTTG_GG**T**GGTGGTGG**T** - 3'

**Z – Gemcitabine phosphoramidite*

Another strategy to improve AS1411 pharmacokinetics is used small molecules, as acridine derivatives, or drugs to confer more stability to aptamers [54].

Already nano approach uses the aptamer targeting properties to deliver drugs or molecules and aims at the attachment of AS1411 into a wide range of nanostructures (Figure 14) [41], [54], [56]. However, the parallel folding is maintained [57].

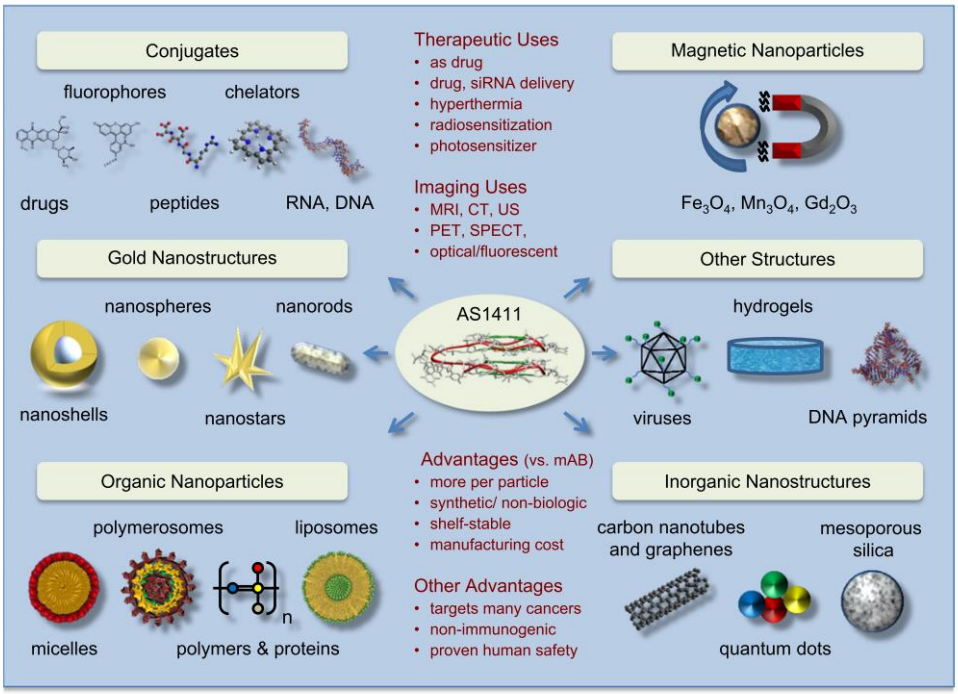

Figure 14. Alternative approaches of AS1411 in therapeutic and imagological uses. Reproduced from [57].

Conjugations offer an improvement in therapeutic efficacy against nucleolin-overexpressing cells [56] by increasing its cellular uptake and accumulation resulting in cytotoxicity and antiproliferative activity in both in cell lines and in in vivo models [41], [54].

Beyond therapeutic, this sequence was used in imaging and diagnostic by delivering drugs or contrast agents selectively to cells, allowing cancer-selective imaging [41], [57] and also for developing aptasensors [54]. Furthermore, it is possible to use AS1411 as a theragnostic agent allowing the delivery of drugs and diagnosis.

2.3.2 Nucleolin

The NCL was firstly described in 1973 in cells of Chinese Hamster Ovary cells and Novikoff hepatoma cells by Orrick *et al* [56], [60]. NCL can be classified as belonging to the class of phosphoproteins and representing 10% of nucleolar proteins, being the most abundant protein of the nucleolus [56], [60], [61]. Beyond this, NCL can be found in other cellular localizations like nucleoplasm, cytoplasm and membrane [61], [62].

The human NCL genes are composed of 13 introns and 14 exons on chromosome 2q12-qter and, as in other species when NCL was discovered, genes are well conserved along with evolution [61]. The NCL has 707 amino acids and a predicted molecular mass around 77 kDa [56], [61].

Structurally, are divided into three multi-domains: N-terminal, the central domain and the C-terminal. The N-terminal is involved in transcription and regulation of rRNA and rDNA, respectively, and also interact with the pre-rRNA processing complex [56], [61]. This is possible due to acid regions, rich in glutamic and aspartic acids, negatively charged, which increase the molecular weight of NCL to 100-110 kDa [61]. Furthermore, this region suffers posttranslational modifications, like phosphorylation and acetylation, allowing protein-protein interactions [60]. Then, the central domain acts as a chaperone on pre-RNA processing, and are composed by four motifs to RNA-recognition, also called RNA-binding domains (RBDs) [56], [62]. Some investigations showed that the number of RBD varies according to specie and demonstrated that specific interactions with RNA are mostly given through first two RBDs [60], [61]. The last multidomain is C-terminal. This is rich in amino acids residues, similarly to N-terminal, and comprised several repetitions of arginine-glycine-glycine (RGG) [56], [60], [61]. The RGG domain is subject of posttranslational methylation which facilitates the interaction of RBD with nucleic acids [60]. Additionally, are responsible for interactions with proteins, namely with ribosomal proteins, being crucial for assembly

and nuclear importation of them [56], [61]. Unfortunately, to date, the three-dimensional structure of the complete NCL has not been resolved.

The NCL also can be considered multifunctional, because are involved in multiple biological processes under both physiological and pathological situations, but analysis of its functions can be difficult due several factors, like as tripartite structure and range of cellular localizations and mechanisms [60]–[62]. For each cellular localization, some functions were schematically described in Figure 15.

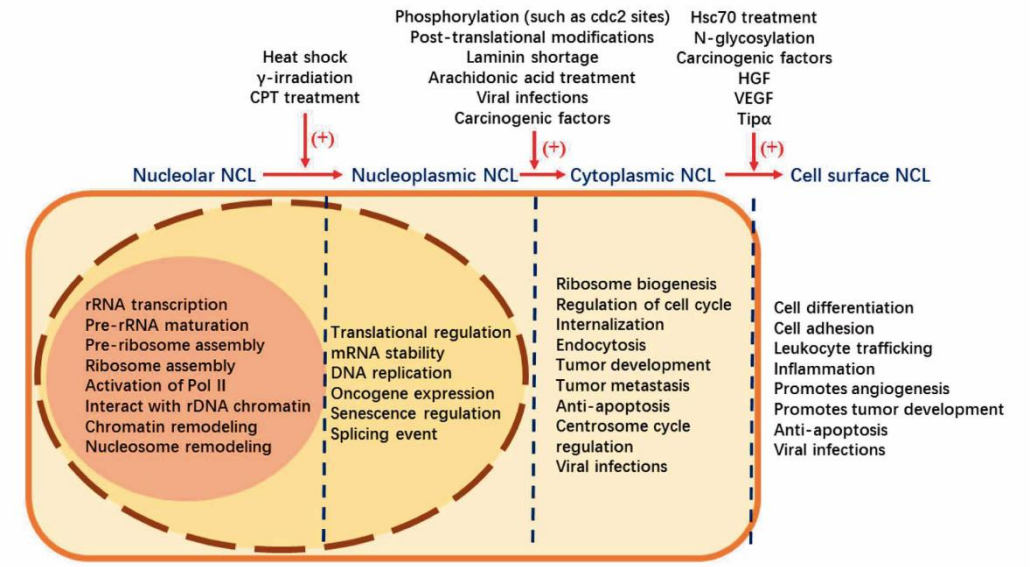

Figure 15. Stimulation factors induce NCL distribution for cellular compartments, being associated with distinct biological functions according to place. Taken from [61].

As reported previously, NCL is prevalent in the nucleolus. This accumulation is caused by RBDs and RGG domains of the primary structure. However, stress conditions or biochemical stimulus and modifications (posttranslational) can induce the shuttling of nucleolar NCL to other locations [61].

Thus, NCL can act as a bridge or a shuttle [63] between cellular compartments and is suggested that lead to metabolic changes: increasing the transcriptional activity, through regulation of oncogenes expression, contributes to cell proliferation, invasiveness, metastasis and aggressiveness of many kinds of tumours. Also, NCL may also protect cancer cells from senescence [56], [60], [61].

Modifications in the expression of NCL, particularly in the cell surface, was found specific to cancer cells [56], [62]. The presence of NCL in advanced PCa has been shown by silver staining of argyrophilic nucleolar organizer regions (AgNOR), indicating the involving in PCa progression (carcinogenesis) [61], [62]. Therefore, NCL

has gained interest as a potential biomarker for cancer diagnosis and a target for cancer treatment.

Additionally, evidences showed that deregulated expression has been associated with a higher risk of cancer recurrence and the multifactorial oncogenic effect of NCL could reflect the multiple functions of this protein [56], [60].

Beyond the presence in solid tumours, has been discovered the existence in cancer cells that have entered the circulation, also called by circulating tumour cells (CTCs) [61]. Additionally, can be founded overexpressed in peripheral blood mononuclear cells (PBMC) of sick individuals, as described in the study conducted by Doctor Carla Cruz (submitted article part of the dissertation).

2.4 Methods for G4 structure determination and interactions study

Different techniques have been developed to study G4. Some of these techniques are biophysical, biochemical, molecular biology, and cellular methods [33], [64]. The biophysical methods (spectroscopic, spectrophotometric and spectrometric) are used in this dissertation to determine structure, morphology, thermodynamics, kinetics, stability and interactions with G4 sequences. Biochemical and molecular biology methods are mostly used to study the formation and understand the role of G4s in function and interaction with other molecules [64]. Each technique examines different characteristics and gives particular information about these structures, being important to complement each other [46], [65].

Thus, in the present section, will be described the different techniques commonly used to study G4. Firstly, it will be mention methods to determine G4 structure followed by methods to study interaction with the targets.

2.4.1 X-ray Crystallography

X-ray crystallography is capable to give information at an atomic-scale resolution of G4, including the cations in the central channel, water molecules, and binders, requiring the production of an ordered crystalline lattice (crystals) of the sequence to be studied [46], [64], [65].

The solid nature of crystals confers the main disadvantage for the method because only report the structure adopted in this state, which is not the same as the adopted in solution. Another handicap, and particularly relevant in G4 due to highly polymorphic

structures, is that crystal structure will be the form that crystallizes most easily rather than most favoured, being able to induce errors in the analysis [46].

Some types of G4s, namely antiparallel-stranded and hybrid are difficult to generate crystals, because packing forces induce conversion to other folds, contrary to what happens in parallel topology [65]. The process to obtain a crystal is considered slow and uncertain [46]. To obtain a sequence that crystallizes and diffracts well, it may be necessary, a base modification with heavy-atom addition (e.g. 5-bromo-thymine) and loop/flanking sequence changes [64], [65]. Beyond this, solvents, cations, ligands (need to be soluble in aqueous media at millimolar concentrations) and annealing conditions play a role in successful crystallization [64], [66]. As reported in studies, small molecules can play as co-precipitating agents because some G4-crystal are obtained only when the ligand is in the crystallization drop [66].

After crystallization X-ray diffraction generated an electron density maps [65]. Good-quality diffraction data (less than 2.5 Å) allows see and quantify linkages in- and out-G4 [64].

2.4.2 Nuclear Magnetic Resonance

Nuclear Magnetic Resonance (NMR) spectroscopy also gives information at the atomic scale and is widely used for the structural study of macromolecules and their interactions [64]. NMR allows determination of structures with high-resolution in solution and relevant physiological conditions, unlike crystallography. Additionally, can provide information about the topology, kinetics and dynamics studies, as well as molecular interactions investigations simultaneously [51], [64], [67], [68].

An NMR experiment requires high-concentration and purity and can be performed without structural modifications, as the inclusion of fluorophores, becoming a least-perturbing technique [46], [51].

The ^{1}H NMR spectrum show and discriminate the type of pairing of nucleic acids. Canonical base-pairing shifts (Watson-Crick) appears low-field to 13–14 ppm, dissimilar of G4, which is revealed by the presence of guanine imino protons of Hoogsteen hydrogen-bonded Gs in the 10–12 ppm range (Figure 16A) [51], [65], [67], [68]. Imino protons of a G4 structure exchange slowly with the deuterated solvent when compared to non-hydrogen-bonded protons, being the hallmark to characterize this secondary structure [46]. Furthermore, imino protons of central G-tetrad exchange more slowly with deuterons when compared outer tetrads due to steric protection resulting in sharp peaks (Figure 16B) [65], [67].

Imino protons associated with folding and times of decay gives information's relatives about kinetics, thermodynamics and unfolding mechanisms [51]. Already, the number of imino protons can be correlated with the number of tetrads. If the number of peaks is equal to the number of G's, we can infer the number of tetrads (4 G's = tetrad), whereas if the number of peaks is superior to G's number, G4 present polymorphism [65], [67].

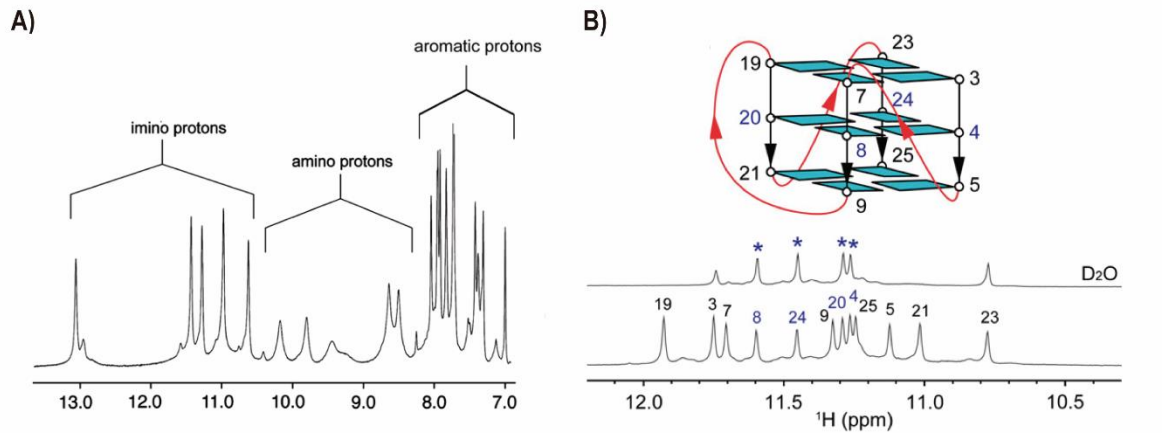

Figure 16. Signals achieved in a proton spectrum (A) and slowly exchange of imino protons with deuterium of central tetrads when in contact with D_2O (B). Adapted from [67], [68].

To solve the full structure of G4, there are many types of NMR experiments which can provide information to assign sugar-phosphate backbone through the interpretation of heteronuclear and multidimensional (bi- and three-dimensional) spectra [46], [65], [68].

The nuclear overhauser effect (NOE) of imino and aromatic regions, through imino-imino and imino-aromatic correlations, can be used to assign topology [51].

Due to the highly polymorphic character of G4, some of this structural information can cause doubts and limit conclusions. Thus, to facilitate and improve NOE experiments, modifications especially through nuclear enrichment (^{13}C, ^{15}N and ^{31}P) and base swap (typically, guanine to inosine or bromo-guanine, or thymine to uracil) or base flanking on sequence can be done [46], [50], [65]. Nucleotide substitution locks the molecules into the isomer and prevents the G4 adopt multiple conformations, improving a clear spectrum analysis [51].

To evaluate interactions between G4 and targets, like proteins or ligands, the NMR technique called saturation transfer difference (STD) can be applied [67].

2.4.3 Mass Spectrometry

Mass spectrometry (MS) is an analytical tool used to identify nucleic acid assemblies [64]. MS requires a minimal sample, is rapid, and versatility [69].

Electrospray ionization (ESI), which ensure non-denaturing conditions, accoupled to MS is used to determine G4 properties like stoichiometry, kinetics and thermodynamics of folding of quadruplexes, but also to show G4-ligand interactions due to ability to preserve and detect non-covalent interaction [64], [65]. ESI-MS produce an aerosol by application of high voltage to a liquid sample [64].

Matrix-assisted laser desorption/ionization (MALDI) is another variation of MS used on folding and consist on a matrix that absorbing laser energy to create ions, which can induce denaturation, unlike ESI-MS [64], [65].

2.4.4 Circular Dichroism

Circular dichroism (CD) spectroscopy is one of the most frequently and straightforward low-resolution method used in biophysics and biochemistry [65]. CD analyses structure, conformation changes, in resulting of the interaction with cations, ligands or proteins, or analyse the thermal denaturation (CD-melting) of nucleic acids (Figure 17A and 17B) [64], [70]. The CD is a rapid and useful method which requires low sample concentration allowing to examine a wide range of conditions that influence G4 formation and stabilization [46], [50].

CD phenomena occur when linearly polarized light passes through optically active species that will rotate and divide the polarized light into left and right circularly polarized components, due to refractive indices [46], [64], [65]. Thus, the CD is defined by the difference in the absorption of the left and right circularly component polarized light, being expressed quantitatively, in degrees, by ellipticity (θ) [64], [65]. CD spectra are measured in the ultraviolet region of light and the different profile result from the different stacking orientation beget by the guanine electronic transitions, more precisely π- π transitions (dipole-dipole interaction) [64], [65].

Hence G4 topology can be predicted from the CD spectrum by analysis of the pattern bands. The parallel topology has a characteristic positive band at 260 nm and a negative band at 240 nm, antiparallel topology presents positive bands at 290 nm and 245 nm, and negative band at 260, whereas hybrid arrangements have a positive band at 290 nm, and a shoulder at 260–270 nm [33], [50], [65], [70]. Polymorphic forms contain a superposition of bands in CD spectra [46].

In Table 5 and Figure 17C are summarized and represented the different topologies and their characteristic wavelengths, respectively.

Table 5. Comparison of CD spectral characteristics of G4.

Topology	Parallel	Anti-Parallel	Hybrid
Positive peak (nm)	260	290 245	290 Shoulder 260-270 nm
Negative peak (nm)	240	260	240
Glycosidic Angle	Anti	Anti/Syn	Anti/Syn

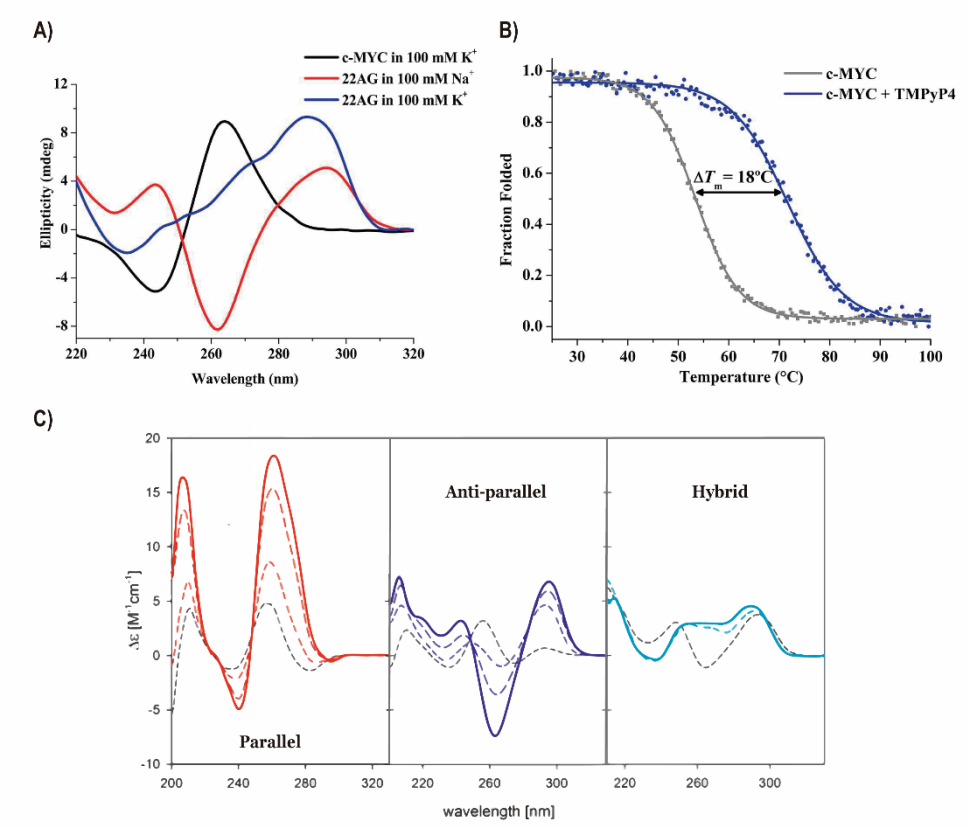

Figure 17. G4 studies in CD. A) Study of cation effect on topology of quadruplex; B) CD-melting assay reporting a stabilization effect of a ligand; C) CD spectra of distinct G4 topologies: Parallel, Anti-Parallel and Hybrid. Adapted from [64], [70].

2.4.5 UV Absorption Spectroscopy

Nucleic acids, as other biomolecules, absorb ultraviolet light. UV absorption spectra slightly differ varies with their base-stacking (topologies) and temperature effect on macromolecules [46]. G4 displays a local maximum at 240, 255, and 275 nm, and a minimum at 295 nm, allowing a ratio construction (ΔA240nm/ΔA295nm) which are capable to discriminate among parallel, antiparallel and hybrid topologies [65].

Thermal difference spectra (TDS) allows studying temperature effect on secondary structure, namely the presence or not of folding or unfolding state. Melting temperature (T_m), by definition is the temperature at which half the nucleic acids has denatured, can be calculated monitoring the absorbance of UV light at 295 nm due to lesser hypochromic shift (i.e. lower absorbance) enabling a thermodynamic analysis using Van't Hoff evaluation [46]. UV-melting is a common methodology to assess the stability of G4 structures [65].

Already, isothermal difference spectra (IDS), allows studying cation effect on secondary structure and folding and it is determined by the difference of spectra in the presence and absence of cations [65]. Beyond this, also can assess ligand effects on the three-dimensional structure.

2.4.6 Biochemical experiments

Biochemical methods such as electrophoretic mobility shift assay (EMSA) and dimethyl sulphate (DMS) footprinting can be used to study G4 formation/stabilization and G4-ligand formation and complement biophysical techniques.

EMSA is based on the separation of G4-target complex according to the different electrophoretic mobilities, on a native polyacrylamide or agarose gel, due to distinct size and a charge showed by the complex [64]. Slower migration indicates interaction and complex formation. Through radioisotope labelling, the method can be improved allowing the use of lower concentrations and determine apparent equilibrium constants for binding reactions [64].

DMS is a powerful biochemical method capable to measure the reactivities of individual nucleotides with DMS which can provide structural characteristics of the nucleic acids. [33], [64]. Briefly, the test is initiated by methylation of the N7 position of G and N3 of A due DMS, which lead to depurination, and then, the piperidine addition leads of cleavage of nucleotide (Figure 18). After this, the sample is running on the gel and cleaved fragments are visualized, corresponding to each guanine in a sequence [46].

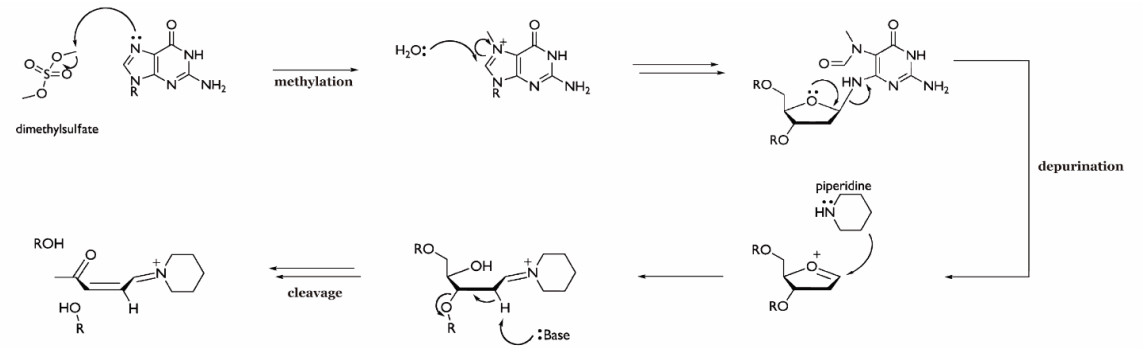

Figure 18. Chemical reactions of DMS and piperidine on purine bases in DMS footprinting assay. Adapted from [46].

G bases are five times more methylated than A bases, promoting more rupture and consequent darker bands (due to ^{32}P labelling) when the gel is resolved [64]. In G4, taking into account its secondary structure, N7 of G involved on Hoogsteen bonds among G is protected of the effect of DMS and piperidine, creating a shelter pattern for G involved on G-tetrad [33], [46].

Additionally, DMS footprinting can be used to predict nucleotides or residues involved on interactions with biomolecules, through analysis of changes on gel bands profile [64].

2.4.7 FRET assay

Fluorescence resonance energy transfer (FRET) is a technique widely employed in biomolecules, such as proteins and nucleic acids, to obtain structural information [71]. FRET-melting is used to evaluate G4 conformation, interactions with ligands and proteins and more recently, are a powerful high-throughput screening tool to drug research [64].

FRET was firstly defined by Theodor Förster in 1948, as a dipole-dipole coupling process among two molecules with the transference of non-radiative energy from excited-state of a donor molecule to an acceptor molecule [64], [71]. To maximize FRET phenomena, the distance between donor and acceptor must be considered, varying between 10–100 A° range [46], [64]. Similarly, to CD-melting, which examine the folding and unfolding state, FRET melting assay can be performed to inquiry this process. In folding state, donor and acceptor are so close, within Förster radius, and fluorescence is quenched by the acceptor. With temperature increase, interactions between the base pairs that stabilize nucleic acids are broken, and molecule starts to unfold, separating the dye and quencher and is emitted donor's fluorescence (Figure 19) [46], [71]. Fluorescence maximum is achieved when biomolecule is completely unfolded.

Energy transfer efficiency decreases rapidly with separation of dyes, as a result of G4 disruption and the donor-acceptor distance can be determined to assess structural information about G4 [46], [71].

To perform the FRET assay, the sequence needs to be labelled to a donor and an acceptor (Figure 19). Acceptors can be classified as dark quencher or fluorescence acceptors, taking into account whether they absorb and transmit the energy as heat to the environment or just re-emit part of the energy transferred from the donor,

respectively [72]. The only requirement is that the excitation spectrum of the acceptor probe is overlaid by the fluorescence emission spectrum of the donor probe [64].

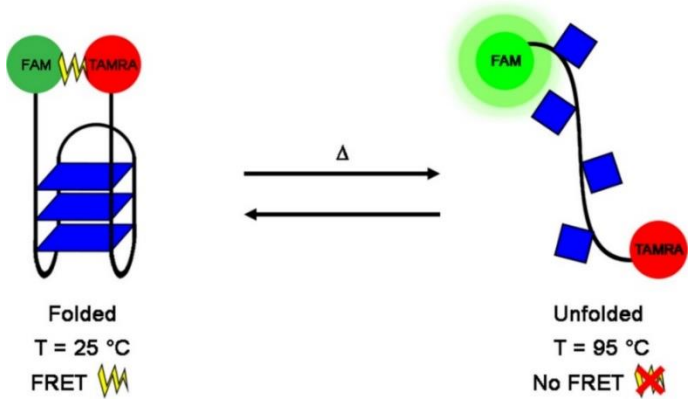

Figure 19. Illustration of temperature increase effect in G4 during FRET assay: structure start to unfold and stop FRET phenomena among donor and quencher, resulting in donor's fluorescence. Taken from [71].

Popular FRET pairs include 6-carboxyfluorescein (FAM)-black hole quencher 1 or 6-carboxytetramethyl rhodamine (TAMRA), FAM-Cy3, Cy3-Cy5, and FAM-rhodamine dyes, as donors and acceptors respectively [64], [71].

2.4.8 Calorimetric methods

Calorimetric methods are divided into Isothermal Titration Calorimetry (ITC) and Differential Scanning Calorimetry (DSC).

ITC is used to study and characterize G4-ligand interactions and can provide binding enthalpies through a direct measurement of heat associated with complex formation. [64]. This method does not require a van't Hoff analysis such as to UV Absorption Spectroscopy, for example [73]. ITC allows determining energetic contributions of complex formation (intermolecular, hydrophobic and electrostatic contributions) from a thermodynamic profile (ΔH, ΔG, ΔS) [64], [73].

DSC is used to obtain kinetic and thermodynamic parameters of G4 formation. The main feature of DSC is temperature variation, unlike ITC, and thus predict stability and conformational behaviour of the G4 sequence at different physical and chemical conditions (temperature, pH, cations and ligands) [64].

3. Molecular Beacons

Understand molecular mechanisms associated to pathologies plays an important role in diagnostics and therapeutics.

In 1996 was firstly reported the term "molecular beacon" (MB) by Tyagi and Kramer [74]. In this study, the authors intended to create a new strategy to measure the degree of nucleic acid hybridization, allowing to study the organization and function of genes and apply to the diagnosis of diseases. In short, they proposed a stem-and-loop structure of a single-stranded DNA molecule, doubly labelled with a fluorophore and a quencher group on each end of the sequence [74]–[77].

The basic principle of operation is based on a structural change of the MB and can be compared as switches. In the absence of target, MB stay in the "off" position (stem-loop structure), due self-hybridizations at the stem [72], [75], [76]. The target hybridizes with the MB causing spontaneous conformational changes that broken stem and open the hairpin, separating the fluorophore from the quencher resulting in a fluorescence restoration [74]–[77]. The MB presents dose-dependent signal, high sensitivity and specificity than linear nucleic acids [72], [75]. Figure 20 shows the schematic representation of the MB, as well as the opening mechanism of the hairpin.

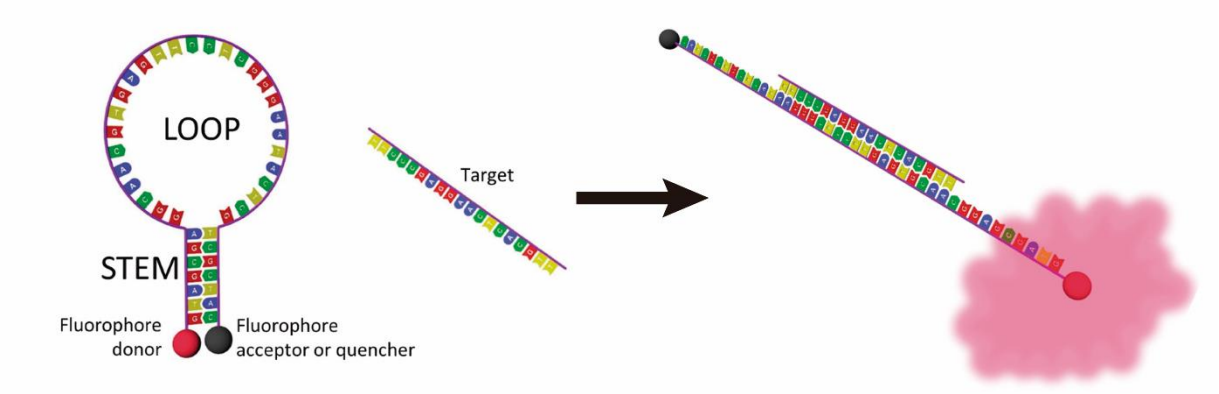

Figure 20. Working principle of MB. When recognize a target occurs fluorescence emission. Adapted from [72].

The conventional MB probe has 25-35 nucleotides and can be divided into four parts: loop, stem, fluorophore and quencher [75].

First, the loop is an 18–30 single-strand region and is the complementary region of the target [72], [74], [75]. The selection of nucleotide sequence and its length determine probe specificity and sensitivity [75], [77]. An increase of the length improve the affinity, nonetheless, reduce specificity [77]. Additionally, adjustments in the GC content of sequence is another approach to optimize sensitivity and specificity [75].

The stem is formed by two complementary oligonucleotides (5–7 nucleotides), commonly with GC content, that was attached to both terminus of probe sequence [75], [77]. The GC content and the length of the stem will influence the kinetics of hybridization (shorter stem = faster hybridization, and vice-versa) and the melting temperature, indicative of the MB stability [74], [75], [77]. Furthermore, when the length is short or long, MB is prone to produce false-negative results or false-positive results, respectively [72], [74], [77].

It is important that MB maintains the hairpin structure without a target because if the fluorophore and quencher are not closed, will emit fluorescence background, and consequently affect the assay [75], [77]. Figure 20 presents MB sequence with the fluorophore and quencher in 5'-end and 3'-end, respectively, and the energy transfer between them lead to the absence of fluorescence.

MBs have two distinct forms of energy transference: the static (also called contact) and dynamic fluorescence quenching. The dynamic comprises FRET transfer (explained in Section 2.4.7) and Dexter transfer (collisional quenching or electron-transfer quenching). The static induces an intramolecular ground-state complex formation, resultant of close contact of dyes [75]. The energy received from the fluorophore is transferred to the quencher, that distorts the energy level of the excited fluorophore and dissipates them through heat, resulting in non-emission of fluorescence by fluorophore [74], [77]. This phenomenon can be explained due to the absorption spectrum of the acceptor overlap the wavelength emission of donor molecules [77].

Thus, to optimize the energy transfer mechanism among dyes and avoiding background, is consider relevant the combination of different fluorophore-quenchers or particles as gold nanoparticles which can act also as quenchers [77].

MB has limitations arose by environmental factors (temperature and environmental pH) which affect MB fluorescence in vivo, due endonucleases effect that generate false results and reduction of probe delivery in cells [77]. However, the major limitation is related to the incapacity to MB recognize other target types other than nucleic acids, such as proteins. Traditional MBs lack specificity in protein recognition, excepting nonspecific interactions [75].

Some of the obstacles mentioned above can be resolved by strategies like wavelength-shifting (presence of dual fluorophore in 5'-end), dual FRET MBs (donor and acceptors MBs), use of aptamers (discussed below in Section 3.1) and conjugation with peptides to improve cell permeation [77].

3.1 Molecular Aptamer Beacons

The aptamers, previously discussed in detail in Section 2.3, present an excellent selectivity and sensitivity to its target. Additionally, the recent interest for this field and application on diagnostics and therapy has grown due to easy manipulation of aptamers, and the tolerance for nonphysiologically conditions [72].

Molecular Aptamer Beacons (MABs) are aptamers conjugated with fluorophores and are highly sensitive, non-invasive, cost-effective with high reproducibility and allows visual detection [72], [75] and can be used electrochemical, optical and fluorescence sensors. MABs stand out from MBs because can adopt new structural designs, unlike the unique hairpin structure in MB. This is achieved using strategies as the creation of recognition subunits in MAB and/or in a variation of dyes place [75]. Already, the operation mode is similar to MBs, in which the target can stabilize the native structure of MAB and result in fluorescence variations [76]. Beyond nucleic acids, MABs can recognize ions, small molecules, and proteins [75].

Hamaguchi *et al.* firstly proposed the use of MABs, namely for proteins recognition [28], [76]. These researchers modified the sequence by adding nucleotides at the 5 'end, which destroy G4, and dyes in both extremities. Conformation is restored with binding to thrombin, creating a dose-dependent fluorescence, due quencher of chromophores (Figure 21A) [72]. Using same aptamer sequence, Takenaka and colleagues demonstrate the use of TBA for the detention of presence of K^+ ion in water. The author's attached pyrene in 5' and 3'-ends of the sequence, which in the presence of cation induces G4 formation leading to emission (Figure 21B) [28].

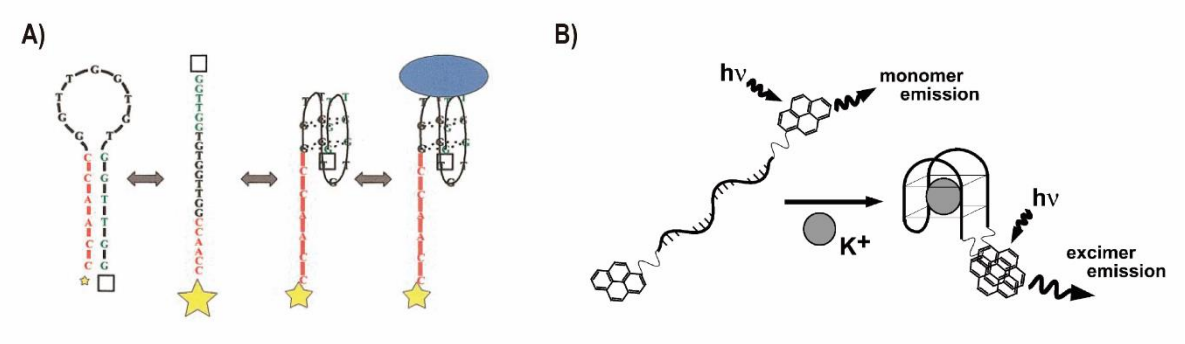

Figure 21. Molecular aptamer beacons to thrombin protein and K^+ ion detection proposed by Hamaguchi and Takenaka, respectively. Taken from [28], [72].

4. Biosensors

The biosensor is a device that combines a biological recognition element and a transducer providing analytical information [78]–[81].

In 1956 was proposed the first biosensor of history for oxygen detection by Professor Leland C. Clark Jr., also called the "father of biosensors" [80]–[82]. After this, the biosensors research line grown exponentially. This effect can be justified by the use of novel biorecognition molecules, miniaturisation and microfabrication technologies developments and the novel nanomaterials and nanostructured devices, allowing the improvement of sensitivity and limit of detection [83].

Nowadays, biosensors comprise since sophisticated high-throughput laboratory machines until easy-to-use portable devices to be used by non-specialists, according to the goals [81]. A wide range of application varies from medical diagnostic, drug discovery, forensics and biomedical research, food safety, process control, agricultural and environmental monitoring [78], [81]–[83]. Biosensors stand out by your several advantages. They are easier and fast, reliable, accurate, high specificity and selectivity, reusability, portable and economic compared with some conventional lab-techniques [78].

As previously mentioned, biosensor combines a bioreceptor with a transducer. These are the main important components of biosensors, and its characteristics allowing to distinguish in different classes [78], [79], [83]. The transducer connects with a complex electronic system responsible for signal amplification and processing of analogic signal into digital signal [82], [84]. Finally, the processed signal is presented in display [82]. The general structure of the biosensors can be visualized in Figure 22.

Figure 22. Schematic illustration of the general structure composition of biosensors and path from the molecule to the signal.

The biorecognition elements are responsible for the identification and interaction with an analyte [79], [82]. The biorecognition elements depend directly on the target of interest being responsible for the identification and interaction with an analyte [78], [79], [82]. Bioreceptors can be based in ligand-receptor interactions, binding and catalysis or involve biomimetic receptors [80]. Plus, allow the classification of sensor

type. Biosensors can be categorized as aptasensors, genosensors, immunosensors, enzymosensors and cell-, tissue-, or organelle-based biosensors when correspondent biomolecule/structure type are used [78], [79], [83]. The biorecognition sensing element dictates the response time, selectivity and specificity of the biosensor, determined by the catalytic or affinity properties, and affect biosensing functional strategy [78], [85]. In Figure 23 are summarized several types of bio-elements.

The transducer has the role of convert the physical, chemical, or biological effects, resultant of biomolecule-analyte interaction, into a measurable optical or electrical signal [78], [80], [82]. Most common type and the most cited in literature kind of transducers are the electrochemical, optical, and piezoelectric (Figure 23) [78], [80].

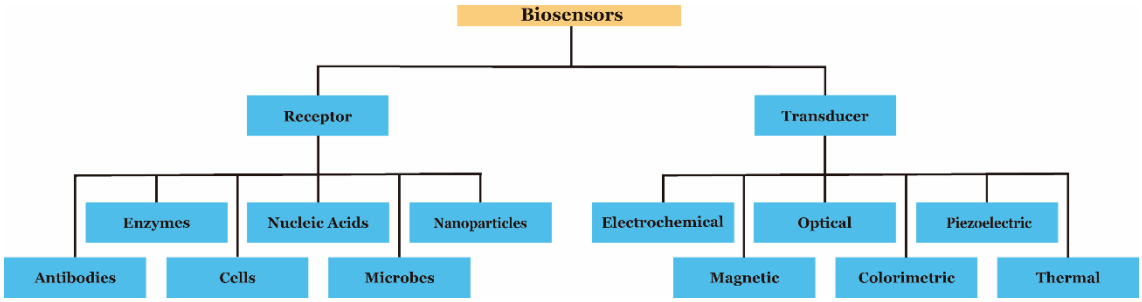

Figure 23. Diagram of type of biosensors according to biorecognition element and transducer.

As referred above, the miniaturization and microfabrication technologies have been used to improve the biosensors field. Thus, the application of microfluidics systems as gained interest on the conversion of biosensors into lab-on-chip (LoC) sensors, characterized by integrating and automate chemical and biological processes and perform full analysis in just on a single platform [78], [79]. This symbiosis of technologies offer an integrated and miniaturized alternative compared to the traditional methods because it offers a significant reduction in test samples and reagents required, energy consumption, test times (due to reductions in diffusion path lengths), and waste production [78], [79], [82]. Simultaneous analysis of several tests (multiplexing analysis) confers another main advantage [79]. These attributes enable a cost decreasing of tests and procedures.

The microfluidic biosensors have the advantage of enhancing the analytical performance by increasing specificity and detection sensitivity limit when compared to the regular detection methods [78]. The miniaturization increases the surface-to-volume ratio of the sensing active area and causes both reduced non-specific binding and an increased binding efficiency towards the target molecule [82]. Additionally, real-time detection, high throughput, fast reaction rates, portability, user-friendliness,

reduced power requirements, and reduced accessories required for their operation construct good qualities for adaptation of microfluidic biosensors in point-of-care (PoC) devices [78], [79].

Microfluidics is the technology of manipulation and controlling fluids in channels at micron-scale [86]–[88]. Fluids amount varies from microlitres to picolitres (10^{-6} t 10^{-12} litres) [88]–[91] which flow in microchannels, with dimensions between 1μm and 1 mm size, on a microelectromechanical system (MEMS) platform [90]–[92]. Currently, microfluidics is considered a multidisciplinary field that involves and links several different sciences as the chemistry, biochemistry, cell biology, biotechnology, engineering, physics and finally micro- and nano-technology, with a common duty of development of LoC devices [78], [87], [88], [91].

The microscopic scale of technique force fluids to adopt and exhibit unique flow patterns, providing precise control of fluids [86]. Microfluidic devices are characterized by the presence of laminar flow, unlike turbulent as is common at the macroscopic scale, due to the surface tension and viscous force that dominate inertial force and gravity [80], [86], [93]. This allows a prediction of flows and confers a control and an enhancement of reproducibility [86].

Therefore, gravity is not relevant in the microfluidic field, differently of intrinsic properties of the fluid. The mechanic of fluids, the rheology, can explain this phenomena and properties, as detailed discussed in the next section.

4.1 Mechanics of Fluids

The Navier-Stokes equation explains the motion of fluid particles taking into account the second law of Newton [87], [91]. Due to the specificities of microfluidic field, the equation can be simplified to:

$$\rho\,\partial t\,v \;=\; -\nabla\rho + \mu\nabla 2v + \rho g + \rho el\,E \qquad \text{Eq. (1)}$$

where ρ is the density of the fluid, p is the pressure field, μ is the dynamic viscosity, g is the acceleration due to gravity, ρ_{el} is the charge density of the fluid, and E is the external electric field.

In biological applications of microfluidics, dimensionless numbers discussed below are considered the most relevant, have importance and can explain some processes.

4.1.1 The Reynolds Number

In 1883 Osborne Reynolds correlated the inertial and viscous forces and proposed the next equation [80], [91]:

$$\mathrm{Re} = \frac{\rho v L}{\mu} \qquad \text{Eq. (2)}$$

Here, ρ is the density of the fluid, v is the bulk velocity, L is the characteristic linear dimension of the system and μ is the dynamic viscosity [80], [92] [91].

Reynolds number (Re) is the most critical number, and give a dimensionless ratio and describe among laminar and turbulent regime [86]. Laminar flow is dominated by viscous forces and fluids flow are parallel/linear to each other, only mixing through advective and molecular diffusion (Brownian fluid), having velocity invariant in time and space [80], [91]. In contrast, turbulent flow exhibit random motion in both space and time and advective mass transport occurs in all directions, being unpredictable and difficult to control [80].

The fluid has a laminar flow behaviour when Re<2000, in turbulent regime Re>3000, while for Re≈2000–3000 is in an intermediate regime [80], [87], [92]. Plus, computational modelling can predict the regime, especially the laminar [86]. In the particular case of microfluidics, the flow is virtually always laminar, unless the fluid is driven at very high velocity [80].

4.1.2 The Péclet Number

Molecules mix due to the motion of fluids. The mixing process can be divided into two conceptual mechanisms: diffusion and advection. The first is promotional to the degree of the kinetic energy of the system, and in the second molecules are mixed by the local velocity of the fluid, due to heat convection chains if heat is being transferred [80].

In microfluidic, the laminar nature of fluids leads to diffusion, which generates longer blending and interaction times of molecules, when compared to turbulent regimes [91].

Mixing mechanisms can be explained by the dimensionless Péclet number (Pe) [80], [91], [92], [94]. Mathematically, Pe correlates the advection and diffusion through of:

$$\mathrm{Pe} = \frac{vL}{D} \qquad \text{Eq. (3)}$$

where v is the fluid velocity, L is the characteristic channel dimension and D is the diffusion coefficient of the solute in the solvent. To Pe<1000 diffusion is more effective than stirring for mixing [80].

The Pe is an important variable to study interaction and to develop a microfluidic device. The microchannels have a compromise between a high rate of molecular capture and efficiency of capture [94]. Microbeads are used to increase the surface-to-volume ratio. This can avoid the increment of flow rates and the loss of a large fraction of molecules (>90%) [94]. Additionally, microbeads can be functionalized allowing immobilization of molecules on the surface.

4.2 Microfabrication

Development of microfluidic devices must take into the dimensions, geometry, surface properties, materials, and the method used for fabrication to improve the biocompatibility and wettability for the designed application [78], [86], [95].

Several types of materials are employed on the fabrication of microfluidic devices such as paper (nitrocellulose or cellulose), silicon, glass, ceramics, metals, elastomers, plastics (cyclic olefin copolymers, polycarbonate or polystyrene), and hydrogels [88], [89], [95], [96]. These will affect physical-chemical properties of the micro platforms, like thermal and electrical conductivity, chemical compatibility and surface properties [96].

Materials with low cost and easy fabrication steps, as the polymeric materials emerged in microfluidic devices fabrication [78], [92]. A large selection of them can be employed as teflon, photo-patternable silicon elastomers, thermoset polyesters, poly-(methylmethacrylate) (PMMA), patterned poly-(dimethylsiloxane) (PDMS), polyimide and SU-8 (negative photoresist) polymers [91]. The two most common materials used for the fabrication of microfluidic chips are the PDMS and PMMA since they provide transparency (230–1100 nm), good mechanical physical and chemical properties, easy fabrication procedures and are cheap [78], [88], [95], [96]. More, are ideal for swift prototyping, which enhances the potential to large-scale fabrication [91], [96].

The PDMS is the material most used in microfabrication of devices [90], [92]. This polymer revealed excellent properties as transparency, flexibility, gas permeability and biocompatibility, ideal for biological field, namely to cells assays [78], [91], [93]. The major challenge of PDMS based-structures is the susceptibility to collapse and deformation, owing to soft elastomer nature and consequently a low Young's modulus [90], [91].

Some drawbacks of PDMS is the adsorption of small molecules, which can affect the assays and the hydrophobic surface properties in the unprocessed state of PDMS [93]. However, there are methods capable to turn the surface more hydrophilic. This is

achieved by exerting external pressure with air/oxygen/argon plasma, UV/ozone or corona discharge to produce hydrophilic silanol groups (SiOH) on the unprocessed surface, in place of CH_3 group [95].

Currently, microfabrication of polymeric-based structures, particularly PDMS-based, is made by a process called Soft Lithography [88], [91], [96]. This denomination is due elastomeric nature of PDMS, and have advantages that are easier, and not require a cleanroom facility just a little bench and faster [92], [94], [95]. Nonetheless, is not an automated process and limit the adaptation to industrial-scale manufacture [92].

Briefly, soft lithography is based on transfer, by replica moulding, of photoresist patterns or silicon substrate, that was an etching by photolithography, to PDMS elastomer [86], [92], [95]. This technique is, represented in Figure 24 and are composed by 3 key steps: (i) hard mask fabrication: (ii) mould fabrication and, finally, (iii) PDMS casting and sealing [91], [94].

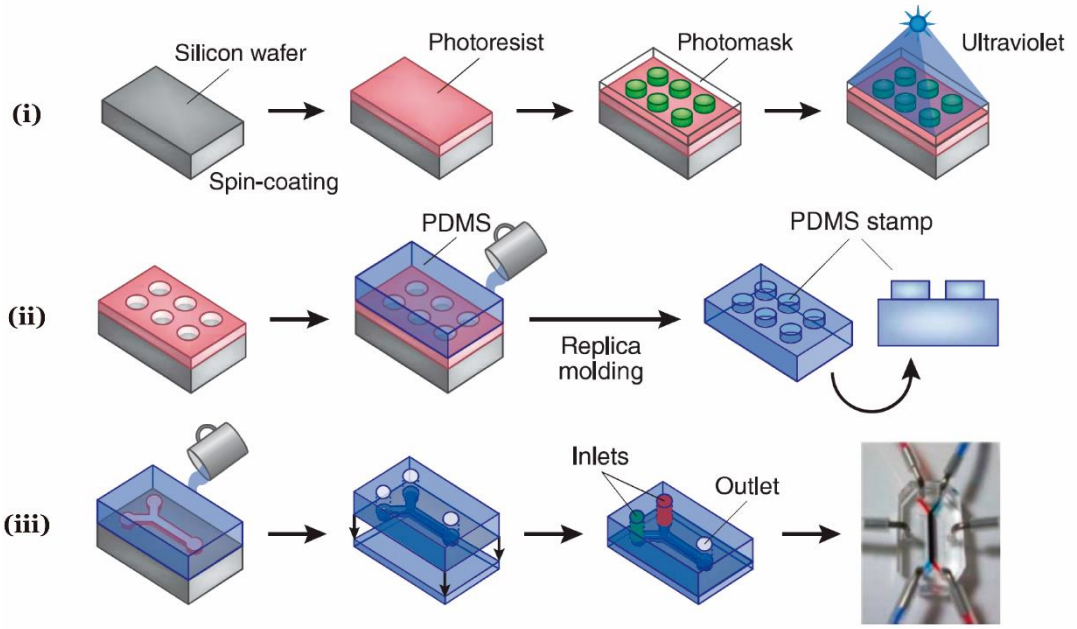

Figure 24. Schematic resume of type of biosensors according to biorecognition element and transducer. Adapted from [97].

Firstly microfluidic pattern is designed in computer software, as the AutoCAD, and then printed on the substrate (glass, silicon or plastic) creating the mask [88], [96]. Next, the microfluidic pattern is transferred to a photosensitive polymer or photoresist, by the photomask, due to the action of UV light that induces reticulation [88], [95]. The photoresist can be positive or negative and the microchannels deepness is determined by your thickness [88], [91]. After constructed mould, PDMS is poured in and baked for polymerization and is formed a well-defined replica of the master [91], [96].

Throughout the state of the art, several advances made in the different areas covered were described.

Starting with the growing problem of cancer, namely PCa, currently, society has faced this disease as a global problem. However, to combat PCa effectively, it is necessary to have early detection of the disease for a higher rate of treatment success and survival. However, the methods existing to date are fallible and have disadvantages.

Several studies reported that PCa cells overexpress NCL, and more recently have been found in large quantities in CTC's and PBMC's of patients with PCa. We can, therefore, consider NCL as a potential biomarker. Thus, facing the difficulties of conventional methods, the idealization of a new approach gains strength, namely using MB.

As discussed in this chapter, an aptamer has been discovered that recognizes and binds NCL with specificity. The aptamer has a high amount of G's in the sequence and thus the ability to form a G4 structure. The following practical component will focus on the use of this sequence in the construction of MAB and subsequent validation by biophysical methods.

Chapter 2

Aims of Work

To address PCa, and considering the advantages of G4 structures, aptamers and microfluidic applications, the objectives of this dissertation are conjugate their potentialities.

Thus, this work will be focused on the development and evaluation of MAB for the detection of circulating nucleolin in plasma and PCa cells.

The dissertation has the main goals:

1. MAB design;
2. Biophysical characterization of the MAB, namely by CD and NMR;
3. Molecular recognition assays of NCL by MAB by fluorescence spectroscopy, FRET-melting and microfluidic assays;
4. *In vitro* evaluation of recognition of MAB by NCL in a cancer cell line.

Chapter 3

Materials and Methods

1. Materials

The water used to prepare all solutions was ultrapure grade, purified with a Milli-Q system from Millipore (USA).

All MABs were synthesized by coupling FAM on 5'-end and a quencher group (DABCYL or TAMRA) on 3' -end of AS1411 (5´- GGTGGTGGTGGTTGTGGTGGTGGTGG -3'). Thus, AS1411-N5 (5´-6-FAM – GTTGGGGTGGTGGTGGTTGTGGTGGTGGTGGCCAAC - DABCYL -3'), and AS1411-N5T (5´-6-FAM – GTTGGGGTGGTGGTGGTTGTGGTGG TGGTGGCCAAC - TAMRA -3') were purchased lyophilized from Eurogentec (Belgium) with double-HPLC purification and used without further treatment.

The concentration of oligonucleotide sample was determined from the absorbance at 260 nm with a UV–Vis spectrophotometer (Thermo Scientific™ Evolution 220) using the molar extinction coefficient (ε) provided by the manufacturer.

Recombinant NCL peptide (RBD1,2 domains and RBD2,3 domains) was purchased from NZYtech (Lisbon, Portugal) and BSA and PSA were obtained from Abcam (Cambridge, UK).

2. Methods

2.1 Design of MAB's

As mentioned in Section 2.2.1 of Introduction, AS1411 is an aptamer with the capacity to specifically recognize NCL. Besides all applications on therapeutics, is possible the use of AS1411 for developing aptasensors [54]. Also, as explained in Section 3.1 of Chapter 1, Hamaguchi *et al.* [76] described an approach with thrombin aptamer sequence (TBA) extended by adding nucleotides to the 5'-end, to achieve a stem-loop structure and a fluorescence quencher pair at both extremities.

Based on this previous study, was modified the structure of AS1411 aptamer through the addition of five nucleotides at the 5´ end and the respective complementary strand at the 3´end. The 5-nucleotide stem generated the highest fluorescence intensity in Hamaguchi research [76]. Nucleotides inclusion form a stem-loop structure represented in Figure 25.

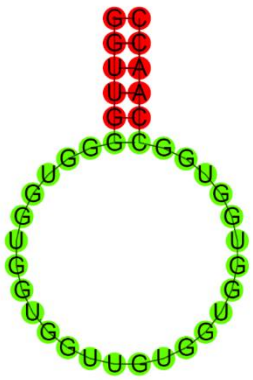

Figure 25. Schematic representation of the expected base pairing of MABs. Duplex-forming nucleotides represented in red while AS1411 sequence is represented in green.

At each end of the sequences, a fluorophore (FAM) and a quencher (DABCYL or TAMRA) were added. It is expected that the addition of NCL promotes conformational changes which result in the separation of the fluorophores, thus, resulting in the increase of fluorescence intensity by FAM as it is no longer quenched by DABCYL.

Sequences were named according to the number of nucleotides and the quencher group for which the G-score was calculated (Table 6).

Table 6. Aptamer beacons sequences derivatives from AS1411. At bold are marked all modifications.

Aptamer	Sequence	G-Score
AS1411	5′ - GGTGGTGGTGGTTGTGGTGGTGGTGG - 3'	21
AS1411 – N5	5´- **6-FAM – GTTGG**GGTGGTGGTGGTTGTGGTGGTGGTGG**CCAAC - DABCYL** - 3’	21
AS1411 – N5T	5´- **6-FAM – GTTGG**GGTGGTGGTGGTTGTGGTGGTGGTGG**CCAAC - TAMRA** - 3’	21

2.2 G4 MAB’s characterization studies

2.2.1 MAB’s preparation

Attending to the work of Hamaguchi *et al.* [76] all aptamers were diluted in 10 mM Tris-HCl pH 7.5. For all experiments, the MABs were annealed by heating to 99°C for 3 min, to dissociate any intermolecular interaction, and was slowly cooling down at room temperature.

However, and considering the results that will be discussed in the next chapter, a new buffer was used. Annealing was performed in 10 mM potassium phosphate buffer, pH 6.9, as already described.

2.2.2 Circular Dichroism (CD) Spectroscopy and CD Melting

CD experiments were performed on a Jasco J-815 CD spectropolarimeter equipped with a Peltier-type temperature controller (model CDF-426S/15). Readings were

performed in a 1 mm path-length quartz cuvettes at 20°C. Spectral width was set to 190–340nm, with a scan speed of 200 nm/min, 1 nm bandwidth, 1s integration time over 5 averaged accumulations. Before the CD spectra measurement, MABs were annealed as already described. During KCl titrations, the required volume of solution from a 1 M stock was added directly to the quartz cell.

After each titration point, a melting experiment was performed. The denaturation process was examined by monitoring the wavelength of maximum ellipticity (260 nm) through temperatures ranging from 20 to 100 °C with a heating rate of 1°C/min. Data were converted into fraction folded (f) plots according to Eq. (4) and fitted to a Boltzmann distribution using OriginPro2016:

$$f = \frac{CD - CD_{\lambda}^{min}}{CD_{\lambda}^{max} - CD_{\lambda}^{min}} \qquad \text{Eq. (4)}$$

The melting temperatures (T_m) were determined from a two-state transition model where CD is the ellipticity at each temperature and CD_{min} and CD_{max} are the lowest and highest ellipticities, respectively.

2.2.3 Nuclear Magnetic Resonance (NMR)

Standard zgesgp ^1H NMR spectra were acquired on a 600 MHz Bruker Avance III spectrometer with a QCI cryoprobe operating at a proton frequency of 600 MHz at chosen temperatures according to experiment.

Merely AS1411-N5 was used, at a concentration of 100 µM with a total volume of 180 µL in a 3mm NMR tube, and annealed as described above in different buffers, supplemented with 10% D2O. NMR titration was performed by adding increasing amounts of KCl directly to the 3 mm tube from a 1 M stock solution.

To Tris-HCl buffer was additionally studied the variation of structure with increasing temperatures.

Standard homonuclear 2D-NMR NOESY spectra were also recorded. Water suppression was achieved using excitation sculpting with gradients (noesyesgpph) pulse. NOESY was acquired with a mixing time (d_8) of 250 ms (SW = 20.03 ppm, TD = 2048, NS = 256, AQ = 0.09 s) and processed to 2048 × 1024 points using a *qsine* function (SSB = 2). All spectra were acquired and processed with the software Topspin 3.1. Images were prepared using MestReNova. Chemical shifts (δ) were measured in part per million (ppm).

2.3 Studies of G4/Nucleolin Interaction

2.3.1 CD Spectroscopy

In addition to CD experiments, a titration with NCL was also performed to study the interaction of NCL with MABs. Readings were did taking account all parameters above defined for Jasco J-815 CD spectropolarimeter. Protein was only added to previously annealed AS1411-N5.

2.3.2 Fluorescence Spectroscopy

Fluorescence titrations were conducted on a Horiba FluoroMax 4 fluorometer (Japan) equipped with a Peltier-type temperature control system, defined to 20 ºC. Reference and samples were scanned using a high-precision quartz suprasil cuvette (light path 10 mm × 4 mm) with an optimal volume of 700 µL.

Before the fluorescence titration experiments, AS1411-N5 at 1 µM concentration was annealed in both buffers containing 100 mM KCl.

The excitation wavelength was 495 nm, matching the maximum absorbance of FAM fluorophore. The fluorescence spectra were acquired between 500–700 nm with an integration time of 0.5 s, an emission and excitation slit fixed at 1 nm and step size of 1 nm, averaged over 3 scans.

To assess the AS1411-N5/NCL affinity, fluorescence titrations were conducted, measuring the change in fluorescence. AS1411-N5 was titrated with increasing concentrations of NCL. After each addition, the mixture was left for 5 min for equilibration and then acquired. The obtained data was converted into a fraction of bound ligand (α) plots using the following equation (Eq. 5):

$$\alpha = \frac{I - I_{\lambda}^{free}}{I_{\lambda}^{bound} - I_{\lambda}^{free}} \qquad \text{Eq. (5)}$$

where I is the fluorescence intensity at 568 nm at each NCL/AS1411-N5 ratio, and I_{free} and I_{bound} are the fluorescence intensity of the free and fully bound NCL, respectively. Data points were then fitted according to the most suitable model (two site bind, Michaelis Menten or Hill model), using Origin Pro 2016, according to following equations:

Table 7. Equations to proceed to fit data points in fluorometric assays.

Two site bind	Michaelis-Menten	Hill
$\alpha = \frac{B_{Max1}[AS1411-N5]^h}{K_{D1}+[AS1411-N5]^h} + \frac{B_{Max2}[AS1411-N5]^h}{K_{D2}+[AS1411-N5]^h}$	$\alpha = \frac{AS1411-N5}{K_D+[AS1411-N5]}$	$\alpha = \frac{[AS1411-N5]^h}{K_D+[AS1411-N5]^h}$

K_D is the apparent equilibrium dissociation constant, [AS1411-N5] is the concentration of the AS1411-N5 and h is the Hill constant which describes the cooperativity of NCL binding.

2.3.3 FRET-melting

Fluorescence resonance energy transfer (FRET) melting experiments were performed in a 96-well plate, in duplicate, using on a CFX Connect™ Real-Time PCR Detection System (Bio-Rad, USA), equipped with a FAM filter (λ_{ex} = 492 nm; λ_{em} = 516 nm).

Initially, the fluorescence measurements were performed in 10 mM Tris-HCl pH 7.5, containing 100 mM KCl. However, due the changing the buffer, as explained in the results, experiments were carried in 10 mM lithium cacodylate pH 6.9 supplemented with 100 mM KCl. Oligonucleotides were annealed before the experiment as described previously in the above sections with a concentration at 0.2 µM.

The samples were prepared by aliquoting 20 µL of MABs into each strip, followed by 5µL of the NCL or bovine serum albumin (BSA) solutions, at five different concentrations (0.1, 0.2, 0.4, 1 and 2 µM). Subsequently, samples were incubated 30 min at room temperature. To examine ligand effect, samples were prepared by aliquoting 15 µL of MABs into each strip, followed by 5 µL of C_8 ligand and 5 µL of the NCL or BSA, at concentrations previously described.

Below, in Figure 26, is presented a condensed schematic representation of the 96-well microplates used in all experiments and respective wells disposition.

	1	2	3	4	5	6	7	8	9	10	11	12
A	AS1411-N5 + Buffer	AS1411-N5 + Buffer	AS1411-N5 + 0,1 µM NCL	AS1411-N5 + 0,1 µM NCL	AS1411-N5 + 0,2 µM NCL	AS1411-N5 + 0,2 µM NCL	AS1411-N5 + 0,4 µM NCL	AS1411-N5 + 0,4 µM NCL	AS1411-N5 + 1 µM NCL	AS1411-N5 + 1 µM NCL	AS1411-N5 + 2 µM NCL	AS1411-N5 + 2 µM NCL
B	AS1411-N5 + Buffer	AS1411-N5 + Buffer	AS1411-N5 + 0,1 µM BSA	AS1411-N5 + 0,1 µM BSA	AS1411-N5 + 0,2 µM BSA	AS1411-N5 + 0,2 µM BSA	AS1411-N5 + 0,4 µM BSA	AS1411-N5 + 0,4 µM BSA	AS1411-N5 + 1 µM BSA	AS1411-N5 + 1 µM BSA	AS1411-N5 + 2 µM BSA	AS1411-N5 + 2 µM BSA
C												
D					AS1411-N5 + 0,2 µM C8	AS1411-N5 + 0,2 µM C8	AS1411-N5 + 1 µM C8	AS1411-N5 + 1 µM C8				
E												
F	AS1411-N5T + Buffer	AS1411-N5T + Buffer	AS1411-N5T + 0,1 µM NCL	AS1411-N5T + 0,1 µM NCL	AS1411-N5T + 0,2 µM NCL	AS1411-N5T + 0,2 µM NCL	AS1411-N5T + 0,4 µM NCL	AS1411-N5T + 0,4 µM NCL	AS1411-N5T + 1 µM NCL	AS1411-N5T + 1 µM NCL	AS1411-N5T + 2 µM NCL	AS1411-N5T + 2 µM NCL
G	AS1411-N5T + Buffer	AS1411-N5T + Buffer	AS1411-N5T + 0,1 µM BSA	AS1411-N5T + 0,1 µM BSA	AS1411-N5T + 0,2 µM BSA	AS1411-N5T + 0,2 µM BSA	AS1411-N5T + 0,4 µM BSA	AS1411-N5T + 0,4 µM BSA	AS1411-N5 + 1 µM BSA	AS1411-N5 + 1 µM BSA	AS1411-N5T + 2 µM BSA	AS1411-N5T + 2 µM BSA
H												

Figure 26. Condensed schematic representation of samples disposition in microplate during FRET-melting assay.

The thermocycler was set to perform a stepwise increase of 1 °C every 1 min, from 25 °C to 95 °C, and measurements of FAM emission were acquired after each step. The melting temperatures were determined from the normalized curves as the temperature for which the normalized emission was 0.5.

2.3.4 *In vitro* assays

2.3.4.1 Cell line

The cancer prostate cell line from prostate carcinoma (PC-3) was used in vitro studies.

The PCa line, according to the American Type Culture Collection (ATCC) information's, is a primary line of adherent cells near-triploid (with 62 chromosomes) capable to form clusters or growth individually. It was established in 1979 from bone metastasis of a grade IV prostatic adenocarcinoma from a 62-year-old male Caucasian.

2.3.4.2 Confocal Fluorescence Microscopy Imaging Studies

The PC3 cell line was grown in RPMI medium, supplemented with 10 % (v/v) fetal bovine serum (FBS) and 1 % (v/v) penicillin-streptomycin. The cell culture was maintained in a humidified chamber at 37 ºC and 5 % CO2. The cell line was subsequently harvested, counted using the trypan blue exclusion method and cultured, at same conditions of the humidified chamber during 24 h, with a density of 10×104 cells/well in treated 8-well µ-slides (IBIDI, Germany), during 24 h.

After cell adhesion, cells were incubated with 1 µM AS1411-N5, previously annealed as described in the above sections, for 1 day. Thereafter, the excess of AS1411-N5 was washed off by rinsing with phosphate-buffered saline three times.

For NCL detection, primary anti-NCL polyclonal antibody (1:100, ref. PA3-16875, Invitrogen, USA) was incubated for 2 h at room temperature. Following primary antibody incubation, cells were washed 3 times with PBS 1× and incubated with secondary antibody anti-rabbit IgG conjugated with Alexa Fluor® 647 (1:1000, Invitrogen, USA) for 1 h at room temperature. Afterwards, cells were washed 3 times with 1×PBS and stained with the nuclear probe Hoechst 33342 (1 µM, Invitrogen, USA) for 15 min, and before visualization, the excess of the probe was washed three times with 1×PBS.

Lastly, the cells were visualized using a Zeiss AxioObserver LSM 710 confocal laser scanning microscope, equipped with a plane-apochromatic 63×/DIC objective and

processed in Zeiss Zen Software (SP2, 2010). The fluorescence images were obtained at 63× magnification.

2.3.5 Human Blood Samples Preparation

Human fresh blood samples (~3-6 mL) from patients previously diagnosed with PCa, at different stages with and without treatment, and healthy volunteers.

Blood samples were collected for a tube coated of ethylenediaminetetraacetic acid (EDTA) (BD Vacutainer® spray-coated with K_2EDTA, BD) according to with the protocol approved by the Ethical Committee of University Hospital Center Cova da Beira (study number 93/2018) and IPO Coimbra (study number 31/PI/2019) and were given written informed consent.

The isolation of blood plasma was performed less than 8 h after the blood collection. Briefly, each blood sample tube was centrifuged at 3000 rpm for 15 min, at room temperature. After centrifugation, the maximum volume of plasma was collected with a micropipette and reserved in 1,5 mL tube. The plasma was stored at -80 ºC fridges until analysis.

2.3.6 Microfluidic Experiments

2.3.6.1 Microfluidic devices development

PDMS microfluidic devices were fabricated by replica moulding from a SU-8 master by INESC – Microsystems and Nanotechnologies (INESC-MN), as described [94]**.** The device was designed to have two-channel heights to allow the holding of the beads inside the channel, as shown in Figure 27A.

In Figure 27B is summarized all fabrication steps, by soft lithography techniques of microfluidic devices. Briefly, to obtain the master mould two aluminium masks were fabricated by direct-write lithography and wet etching to define each of the 20 and 100 μm tall features. The 20 μm tall layer was fabricated using SU-8 2015 (Microchem Corp., Newton, USA), spin-coated on top of a silicon substrate.

After development with propylene glycol monomethyl ether acetate (PGMEA) (Sigma-Aldrich), the second layer of SU-8 50 for the 100 μm tall layer was spin-coated on top of the first layer. The second hard mask was manually aligned with the 20 μm features prior to exposure to UV light.

Finally, exposed SU-8 was developed in PGMEA and hard-baked at 150 °C for 15 min. The PDMS structures were fabricated by mixing PDMS pre-polymer with curing agent in a 10:1 ratio (Sylgard 184 silicone elastomer kit, Dow Corning, USA). The PDMS was poured on top of the master mould and cured at 70 °C for 90 min.

After peeling PDMS of the master mould, access holes were punched using a 14 ga and 20 ga blunt needles for the inlets and outlets, respectively. The device was sealed against a 500 µm PDMS slab after treating both surfaces with an oxygen plasma (Harrick Plasma, USA).

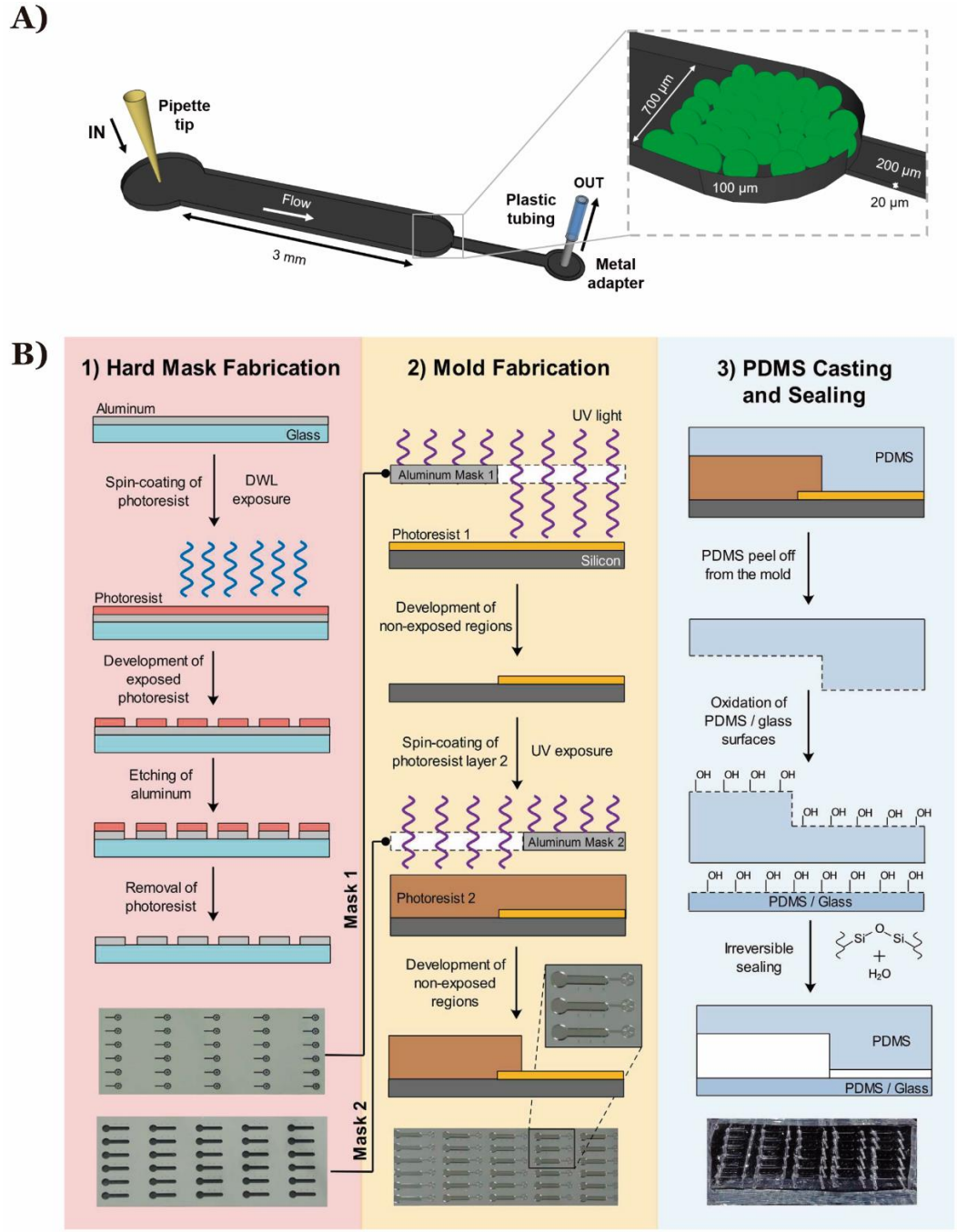

Figure 27. Microchannel platform design and fabrication. (A) Design of the two-height microfluidic structure and (B) Soft Lithography microfabrication of PDMS-based devices. Figure B was taken from [94].

2.3.6.2 Microfluidic structure packing

The description of the microfluidic working setup, fluid handling and packing of the CM Sephadex C-25 beads were carried out as previously detailed [94]**.** Briefly, the liquids were driven inside the microchannel using a syringe pump exerting a negative hydrostatic pressure at the outlet (NE-4002X, New Era Pump System Inc., USA). The negative pressure will provide a simplified operation, a gradual increase in liquid flow velocity, a minor distortion of the PDMS channel and a lower deformation of the beads.

The beads were first suspended in a solution of 20% (w/w) polyethene glycol 8000 (PEG) (Sigma-Aldrich) and packed inside the channel at a flow rate of 7 µL/min, followed by a washing step with 1×PBS at a flow rate of 7 µL/min.

Beads were used in the microfluidic platform to increase surface area and decrease the assay time.

2.3.6.3 Microfluidic assays and image acquisition

Microfluidic experiments were performed with MAB AS1411-N5. Firstly, the AS1411-N5 (8 µM) was incubated with NCL (5 µM) for 10 min. Thereafter, 0.1 M acetate buffer at pH 4.5 was added to change the surface charge of NCL. The experiment was carried out at a flow rate of 1 µL/min for 30 min. Lastly, the channels were washed with 1×PBS at a flow rate of 5 µL/min for 2 min to remove non-specifically bound molecules.

All fluorescence images were acquired with an exposure time of 2 sec in a Widefield Axio Observer Z1 inverted microscope using 488 nm as the excitation wavelength (BP 470/40 filter) and collecting the emission at 520 nm (BP 525/50 filter).

Images were processed with Zeiss Zen Software (SP2, 2010) and ImageJ (National Institute of Health, Bethesda, MD, USA). Fluorescence emission values were obtained by averaging the entire end-section of the micro-columns. For every individual experiment, new structures with fresh functionalization steps were performed.

Chapter 4

Results and Discussion

AS1411 is a G4-forming DNA oligonucleotide that functions as an aptamer of NCL, a protein overexpressed on the surface of PCa cells [98]. Besides, AS1411 can be used as a probe for the diagnosis of cancer due to its high affinity and specificity for cell surface NCL [99].

AS1411 aptamer was recently used as a recognition probe of an electrochemical aptasensor, which can distinguish cancer cells from normal ones by recognition of cell surface NCL [100]. Furthermore, the potential of AS1411 in novel cancer imaging techniques was shown in a study where a nanoparticle-based cancer-specific imaging probe using the AS1411 aptamer was developed to visualize the location of NCL protein in vitro and in vivo [101]. However AS1411 lack the built-in mechanism for signal transduction, not allowing the detection of conformational changes, upon NCL binding [102]. Thus, it is desirable to combine the binding specificity of AS1411 with the excellent signal transduction capability of a molecular beacon system to develop a novel protein-reporting probe for NCL detection and quantification.

Taking into account the Hamaguchi study [76], it was used MAB derivative of AS1411 (Table 7), able to signal conformational changes by fluorescence emission. Illustrative MAB design is represented in Figure 25. According to the calculated G-score, with the value of 21, we can predict that both AS1411 and MAB (AS1411N5) have the ability to adopt a G4 conformation.

It is expectable that fluorophore (FAM) and a quencher (DABCYL) provide weak fluorescence in the absence of the NCL, while, in the presence of NCL, the fluorescence intensity increases as a result of the structural switch of MAB. In this way, the quencher and fluorescence reporter was more distant, which led to fluorescence emission.

Thus, this chapter was divided into two parts, focus on structural and binding studies performed with MAB (AS1411N5) and NCL. In Part A, preliminary studies related with the optimization of G4 formation/stabilization in MAB are presented done by biophysical techniques, and in Part B the MAB (AS1411N5) was used to be applied in a microfluidic device to detect NCL by fluorescence emission using PCa samples.

PART A – Preliminary Studies

1. Characterization studies of G4 MAB

1.1 CD Spectroscopy

Firstly, the structural arrangement of the MAB was addressed by CD spectroscopy. This technique is a useful approach to examine the conformation of G4 structures.

The CD spectra of AS1411 and AS1411-N5 in the absence and presence of increasing amounts of KCl are presented in Figure 28.

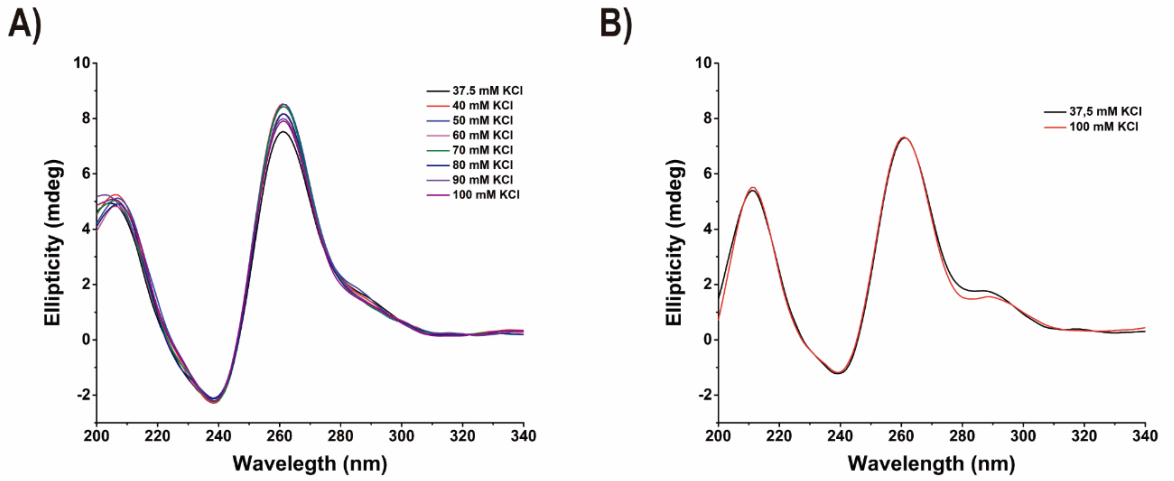

Figure 28. CD spectroscopy analysis of AS1411-N5 and AS1411 structures. CD spectra in the presence of increasing amounts of KCl (37,5 - 100 mM) of A) AS1411-N5 and B) AS1411.

Upon titration of AS1411-N5 with KCl, the formation of a parallel-stranded G4 is induced, as seen by the positive band around 260 nm and a negative band around 240 nm [70]. The AS1411, in the same buffer conditions, presents mostly a parallel conformation, however, it is visible a slight difference among CD spectra around 280-290 nm. These bands are due to antiparallel and/or hybrid topologies due to the previous characterization of the polymorphic nature of AS1411 [54], [59].

During titration, a slight increase in ellipticity was observed together with the retention of the characteristic bands, suggesting a dependence on K^+ for the stabilization of the G4 structure. This result was further corroborated by CD melting experiments.

The melting temperature (T_m) of AS1411-N5 and AS1411 was determined by monitoring the wavelength of maximum ellipticity at increasing temperatures. Figure 29 represents the CD melting curves with increasing KCl concentration to both sequences.

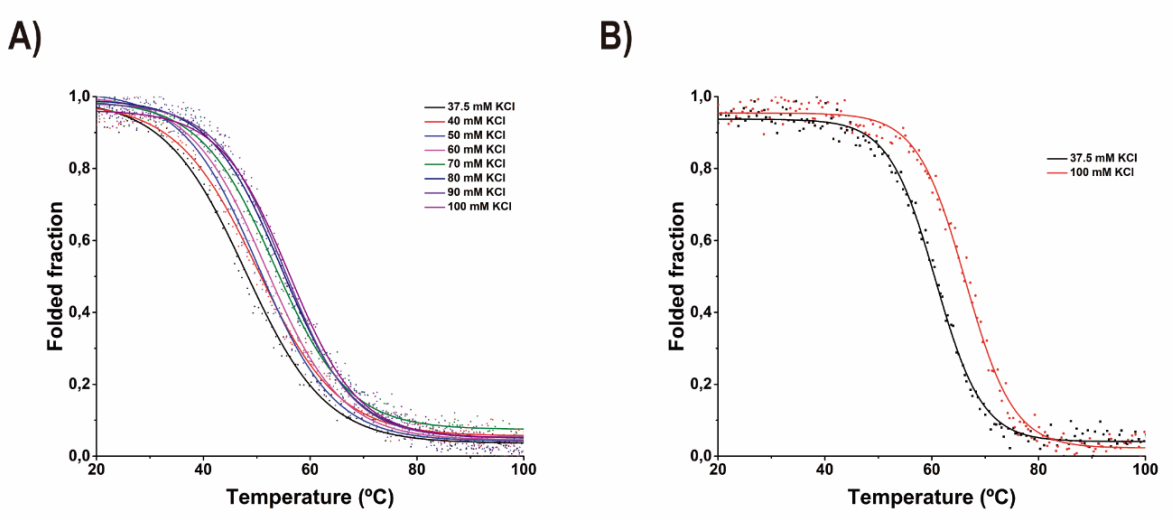

Figure 29. CD-melting spectroscopy analysis of AS1411-N5 and AS1411 sequences. A) CD melting curves in the presence of increasing amounts of KCl (37,5-100 mM) in AS1411-N5 and B) in AS1411 sequence.

As suggested by the CD melting data, K^+ seems to stabilize the G4 of AS1411-N5 by increasing T_m values from 47.7°C ± 0.23 to 56.08 °C ± 0.17 at 37.5 and 100 mM of KCl, respectively.

For G4 AS1411 the same effect was observed. T_m increases by 60.71 °C ± 0.11 to 66.29 °C ± 0.13 in the presence of increasing concentrations of K^+. Taking these data into account, we concluded that K^+ has a greater stabilizing effect on As1411, unlike AS1411-N5. The possible explanation is that the duplex stem portion of MAB can reduce the stability of G4 region.

1.2 NMR Spectroscopy

^{1}H NMR titrations of AS1411-N5 with increasing concentrations of KCl were performed at a temperature of 20°C to assess the cation effect on the structure. The spectra are shown in Figure 30.

With increasing amounts of KCl in the NMR tube, two well-defined sets of signals corresponding to the duplex extension (12.5 - 14 ppm) and the G4 structure (10 - 12 ppm) became clearly visible. This suggests that both structures can form in solution simultaneously, and the possible conformation formed is presented in Figure 31A. This conformation was also based on the previous CD results, evidenced a parallel topology for AS1411-N5.

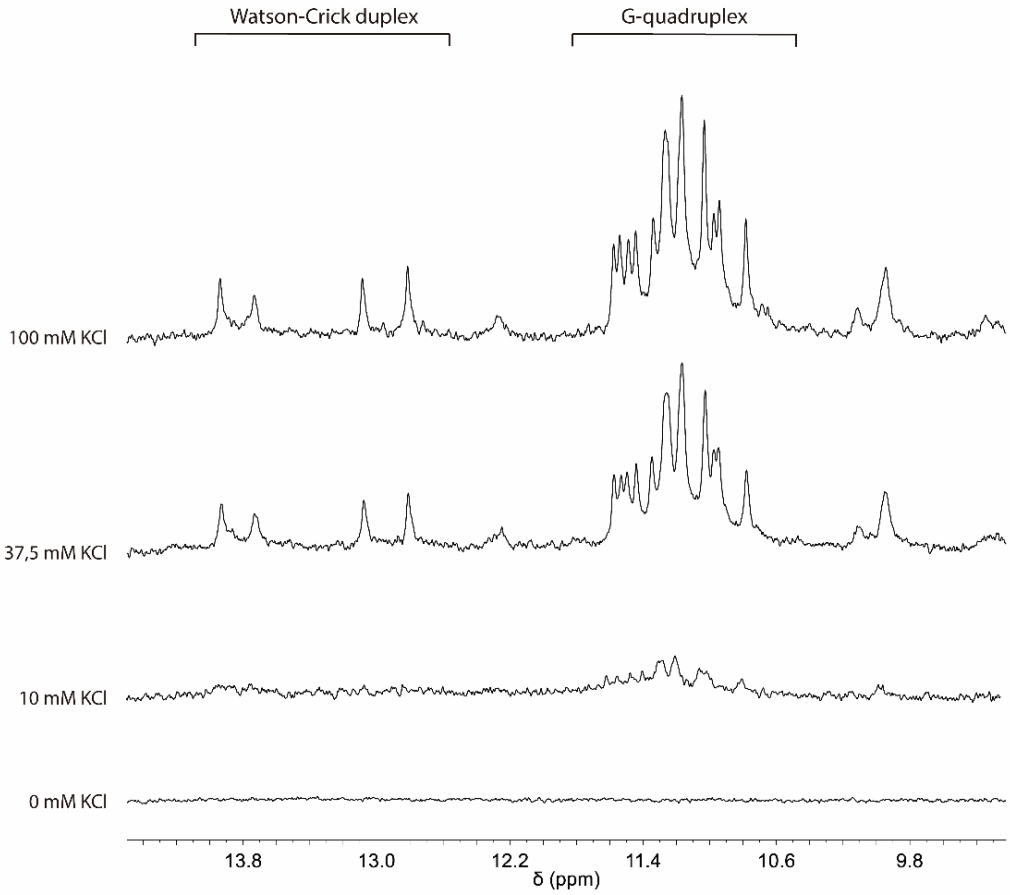

Figure 30. ^{1}H NMR titration of AS1411-N5 with increasing amounts of KCl salt. The sets of peaks corresponding to the duplex base pairing and the imino protons from the G4 structure is highlighted.

Unlike unmodified AS1411 which folds into multiple G4 structures [54], AS1411-N5 seems to fold into a major well-defined G4 conformation as shown by the existence of a single set of 17 well-defined imino signals. The imino signals match to guanines number of aptamer portion of MAB, concluding that all G's are involved in the formation of the G4. This may occur due to the duplex tail which potentially locks the structure in a single conformation hampering the polymorphism of the sequence.

Indeed, the imino region (Figure 31B) resembles AT11, AT11-Bo and AT11-Lo, derivatives of AS1411, which possess only a single G4 conformation due to the addition of thymine nucleotides to both 5'- and 3'-ends of AS1411 sequence and a G-to-T modification at position 11 [103], [104]. The ^{1}H NMR spectra of AS1411-N5 and AT11 are presented in Figure 31C to compare the imino signals.

The fact that AS1411-N5 adopts a single G4 conformation may enhance its NCL RBD1,2 recognition ability and enables the determination of AS1411 G4 structure without mutations in native sequence, unlike AT11.

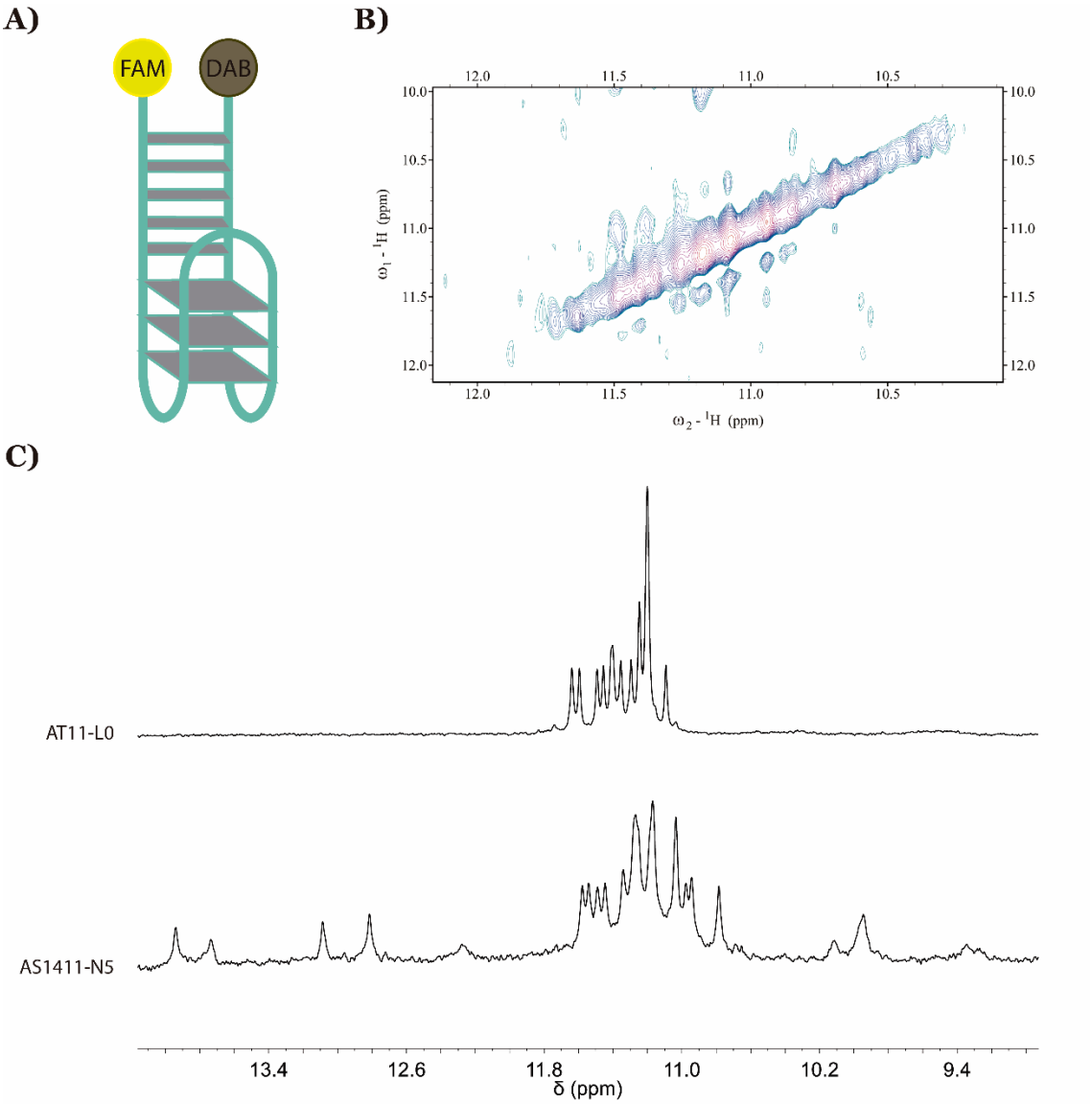

Figure 31. (A)Possible structure of MAB, (B) bidimensional NMR spectrum of G4 imino region and (C) comparison of ^{1}H NMR spectra among AS1411-N5 and AT11-L0.

2. Studies of G4/Nucleolin Interaction

After optimization of G4 formation in AS1411-N5 sequence, its ability to recognize NCL protein was assessed by CD, fluorescence spectroscopy and FRET-melting assay. The RBD domains 1, 2 and 3 (RBD1,2 and RBD2,3) of NCL were used to study the recognition by AS1411-N5 G4.

2.1 CD Spectroscopy

The NCL binding to G4 pre-folded AS1411-N5 was performed by CD titration. In Figure 32A, we observed a slight increase in the ellipticity near to 260 nm, possibly evidencing

the interaction between the protein and the aptamer. At 0,5 nM the negative band of NCL becomes evident at around 225 nm, showing the typical signature of a β-sheet secondary structure [105].

Remarkably, the analysis of the CD spectra of NCL RBD1,2 in the absence of AS1411-N5 shows the spectral features of a typical α-helix secondary structure, with a double negative band at around 210 and 220 nm (Figure 32B) [105]. This suggests that the RBD1,2 domains may undergo a conformational rearrangement in order to bind the G4 structure.

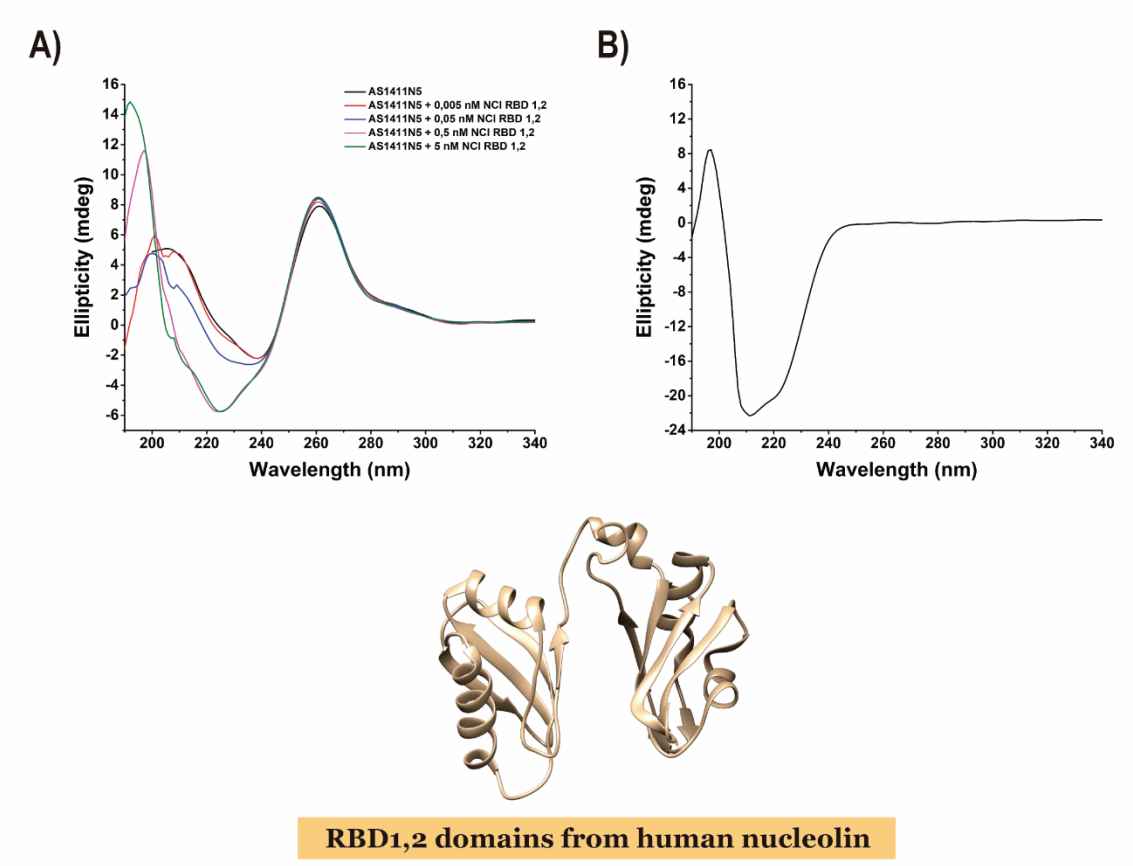

Figure 32. CD spectroscopy analysis of the interaction between AS1411-N5 G4 structure and NCL protein. A) CD spectra of AS1411-N5 in the absence and presence of increasing amounts of NCL RBD1,2 (0-5 nM) and B) CD spectrum of NCL RBD1,2 alone at 0,5 nM concentration. C) Solution structure of the RBD1,2 domains from human nucleolin. The three-dimensional picture was downloaded from Protein Data Bank (PDB entry: 2KRR) and generated by UCSF Chimera 1.12.

The solution structure of the human NCL RBD1,2 domains (Figure 32C) shows that it contains both α-helices and β-sheets in similar number [106], being therefore plausible that both signatures are observable in CD spectroscopy, depending on the adopted conformation in the absence and presence of AS1411-N5.

2.2 Fluorescence Spectroscopy

Following structural characterization, fluorescence titrations were employed to determine the binding affinity of the AS1411-N5 to NCL RBD1,2 and RBD2,3.

The fluorescence experiments were performed with AS1411-N5 labelled with 5'-FAM and 3'-DABCYL. Fluorescence emission spectra of AS1411-N5 were recorded at 568 nm, in the absence and presence of both increasing amounts of NCL RBD1,2 and NCL RBD2,3. The results are depicted in Figure 33A and 33C.

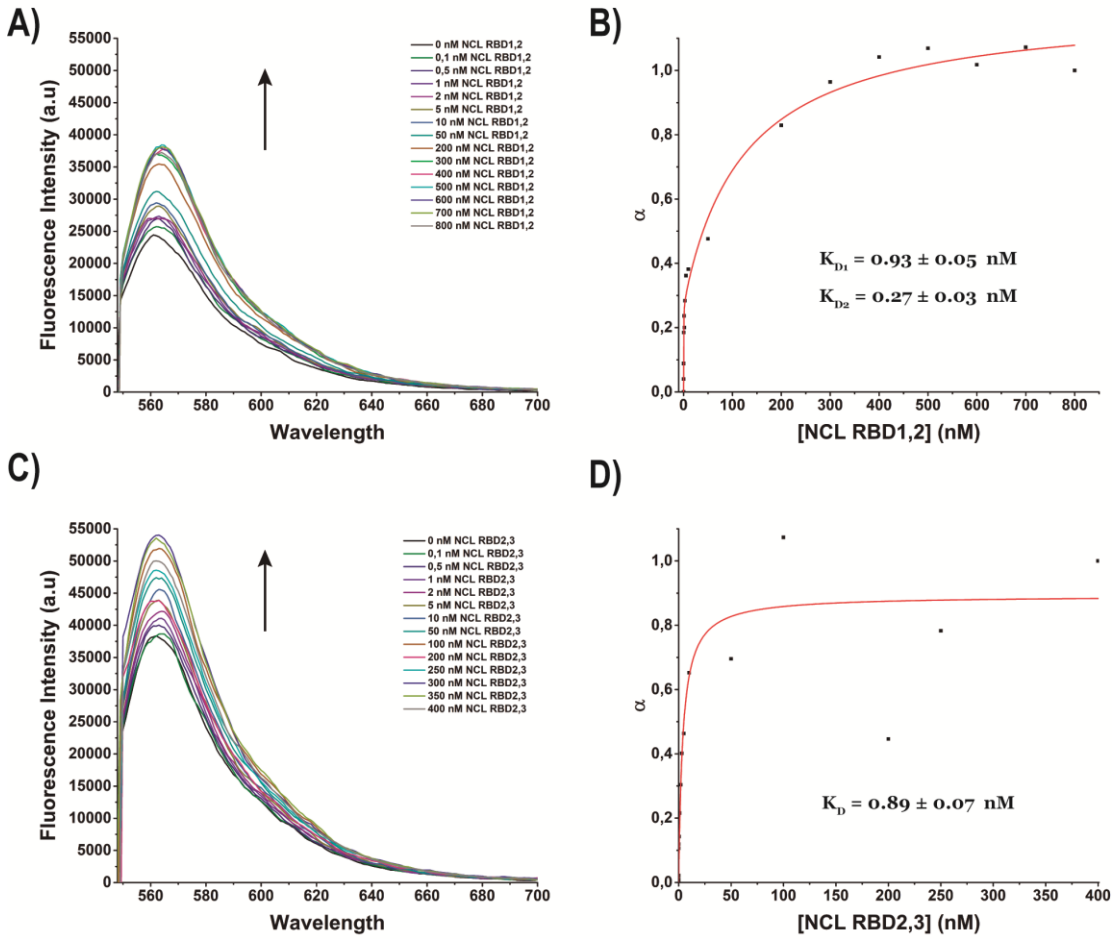

Figure 33. Fluorescence titrations of the AS1411-N5 with increasing amounts of NCL RBD1,2 and NCL RBD2,3. A) and C) Fluorescence emission spectra of AS1411-N5 (1 μM) with increasing concentration of NCL RBD1,2 and NCL RBD2,3, respectively, in 10 mM Tris-HCl buffer, pH 7.5 containing 100 mM KCl; B) and D) The fraction of ligand-bound plots fitted to the saturation binding equation (two site bind and Michaelis-Menten equation).

The K_D values indicated an increase in fluorescence units at saturating NCL concentrations. The binding plots were obtained by non-linear regression analysis applying the two site bind fit and Michaelis-Menten equation presented in Figures 33B and 33D.

Interestingly, the interaction between the AS1411-N5 and NCL RBD1,2 generate two dissociation constants. The K_D values were 0.27 ± 0.03 nM and 0.93 ± 0.05 nM, respectively corresponding to first and second constants. the two constants can be explained by the interaction of G4 AS1411-N5 with one domain at each time. These affinities, in the nanomolar range, agree with those constants reported in the literature for aptamer AS1411 [103], [107]. These results suggest that the binding to NCL RBD1,2 occurs mainly through AS1411-N5 G4 structure and that the five natural base pairs in the stem region do not affect negatively the interaction of NCL RBD1,2 to AS1411-N5.

Relatively to AS1411-N5/NCL RBD2,3, firstly was observed an increase of fluorescence when compared with RBD1,2 domain. As previously, we applied the Michaelis-Menten equation to determine K_D value and it was 0.89 ± 0.07 nM. This result is like that reported in the literature showing higher affinity in the nanomolar range.

2.3 FRET-melting assays

Additionally, FRET melting experiments were carried out to evaluate the stabilizing effects of NCL domains to G4 AS1411-N5. The assays were performed with the AS1411-N5 incubated to target and non-target proteins, NCL RBD1,2 and BSA. BSA is used as a negative control. Figures 34A and 34B present the FRET spectra.

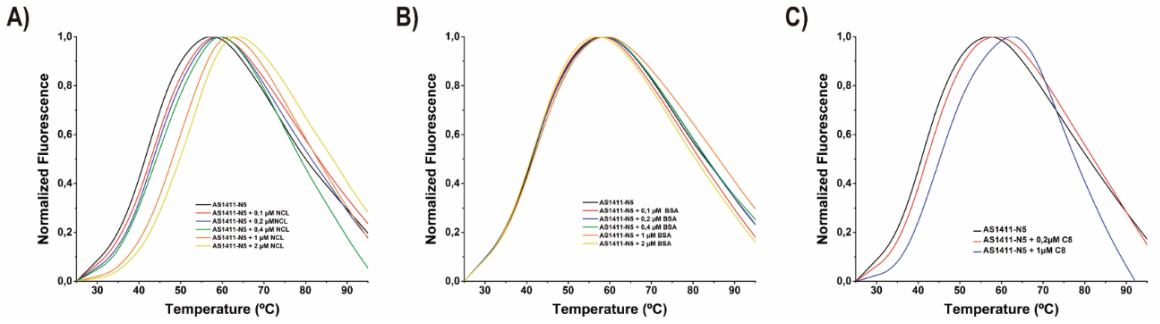

Figure 34. FRET-melting spectra of AS1411-N5 to study structure and specificity. Were performed several tests to NCL RBD1,2, BSA and C_8 acridine ligand.

According to the spectra, these results were not expected. Surprisingly, the FRET-melting spectra profile is not a typical denaturation curve with the two-fold-state transition. Thus, the melting temperatures, which commonly are determined from the normalized curves as the temperature for which the normalized emission was 0.5, were not possible to acquire. Also, with BSA the same curve profile was obtained.

After that, and to discard proteins precipitation or degradation in the assay was performed with a known potent stabilizer of G4 structures, the C_8 acridine derivative,

[54], [103]. We have obtained the same atypical FRET-melting spectrum profile. Similarly, to the theoretical stabilization of C_8, in the FRET-melting curves was visible an improvement on the thermal stability with increasing concentration of C_8 ligand.

After that, to elucidate the structural behaviour of AS1411-N5 especially near the flip point of the curve, we have acquired ^{1}H NMR spectrum at 50, 55 and 60ºC corresponding to flip point of the curve, respectively (Figure 35).

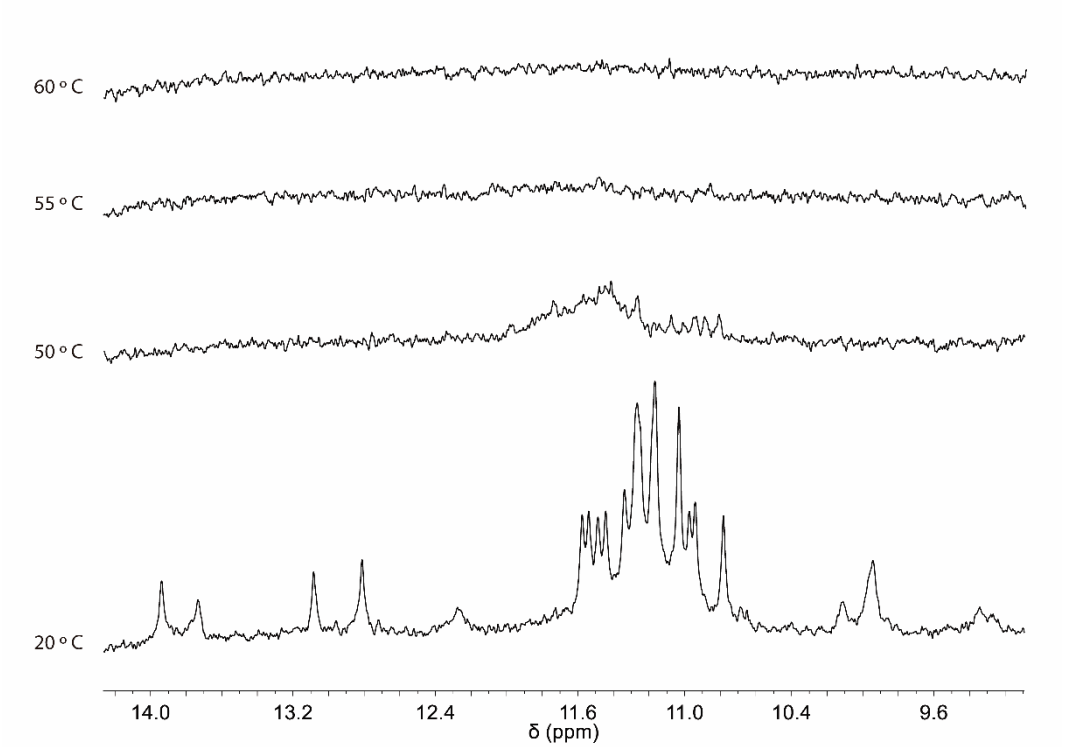

Figure 35. ^{1}H NMR of AS1411-N5 at different temperatures (20, 50, 55, and 60ºC). With an increase on temperature is visible growth of the unfolding state.

Figure 35 shows that with the increase of temperature, G4 AS1411-N5 is led to the unfolding state. To highlight that at the temperature of 50ºC (point before curvature), the structure was not completely unfolded and present a possible G4 structure, due to the presence of imino proton signals (from 10.6 ppm to 11.7 ppm).

After that and to elucidate the results obtained, we studied the structural changes by varying the temperature using fluorescence spectroscopy and are presented in Figure 36. The temperatures were chosen according to the range of the FRET-melting protocol.

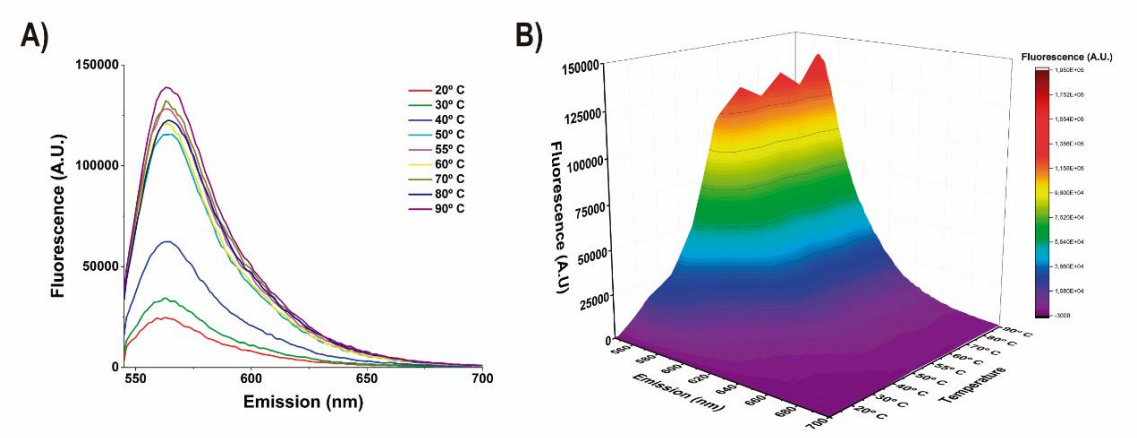

Figure 36. Temperature variation of AS1411-N5 determined by fluorescence spectroscopy. A) The bidimensional spectra which correlate fluorescence intensity with temperature; B) Surface response plot for all temperatures tested.

The results presented in Figure 36 showed an increase of fluorescence at high temperatures. Additionally, it was observed that in the lower temperatures the fluorescence phenomenon occurs. One explanation is the non-complete intramolecular hybridization of AS1411-N5. Besides, fluorescence increment can be associated with the intermolecular interactions between beacons molecules, that produce a steric effect, and not allowing the contact and existence of FRET phenomena among donor and quencher. However, the disruption of intermolecular interactions can cause the opposite effect, releasing dyes to produce fluorescence.

To evaluate if the structural changes in AS1411-N5 were due to the donor and quencher we change the quencher from DABCYL to TAMRA in position 3´. The sequence was designated by AS1411-N5T. The structural characterization of AS1411-N5T was performed by CD spectroscopy to evaluate if AS1411-N5T adopt a G4 topology using the same buffer conditions, that was, 10 mM Tris-HCl pH 7.5 supplemented with 100 mM KCl, Figure 37A presents the CD spectra of AS1411-N5T.

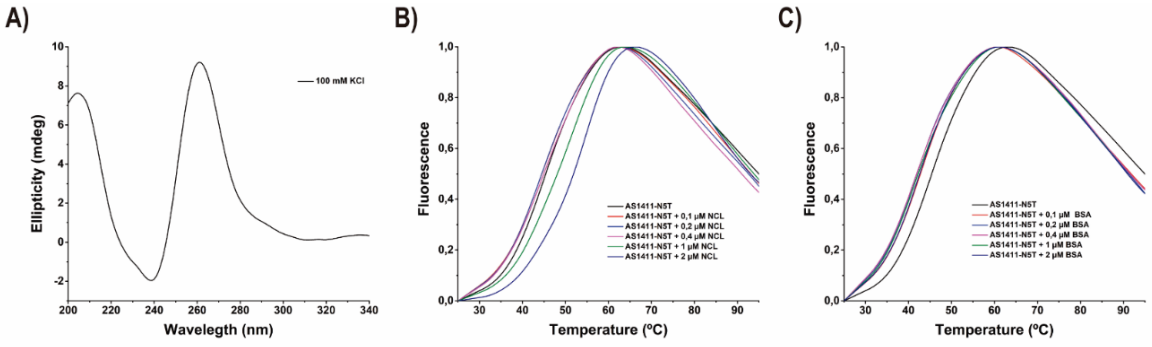

Figure 37. CD spectroscopy analysis and FRET-melting spectrum of AS1411-N5T. A) CD spectra of AS1411-N5T in the presence of 100 mM of KCl and B) Atypical FRET-melting curves of AS1411-N5T when incubated with NCL RBD1,2 and BSA.

The AS1411-N5T adopts a parallel-stranded G4, as denoted by the characteristic positive band around 260 nm and a negative band around 240 nm [70]. We conclude that the quencher TAMRA did not modify the G4 structure.

The FRET-melting assay was also performed with AS1411-N5T and the same atypical profile was obtained (Figure 37 B and C).

Mergny and Lacroix [108] were described that several buffers, as Tris-HCl, the pH value change with the increasing of temperature (until two pH units from 0 - 100°C). Hence this buffer is not appropriate for T_m experiments. Plus, the refractive index of some solvents can have the capacity to change the intensity emission of fluorophores [72], namely from FAM which is strongly pH-dependent [109].

Therefore, due to the negative contribution of buffer to the stability of G4 AS1411-N5 we change the buffer to potassium phosphate, already used for AS1411 derivatives [110]. Specifically and for FRET-melting assays, we selected lithium cacodylate buffer pH 6.9 at 10 mM because is the reference buffer for melting experiments due to not interact with the components of the solution and not absorb light of UV-region, and is temperature independent and the pK_a value is close to pH value [71], [108], [109].

PART B

All structural characterization and interaction of AS1411N5 to NCL were performed in potassium phosphate.

1. Characterization studies of G4 MAB

1.1 CD Spectroscopy

The structural arrangement of the AS1411-N5 in potassium phosphate buffer was addressed by CD spectroscopy. Similarly to CD experiment described in Part A, firstly the experiments were conducted in the absence and presence of increasing amounts of KCl (Figure 38A).

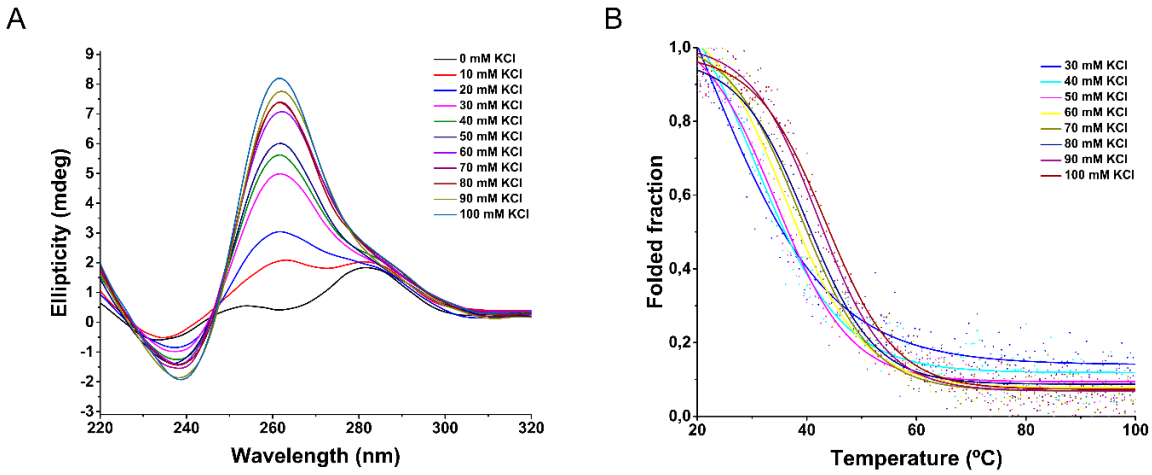

Figure 38. CD spectroscopy analysis of AS1411-N5 structure. A) CD spectra of AS1411-N5 in the absence and presence of increasing amounts of KCl (0-100 mM) and B) CD melting curves of AS1411-N5 in presence of increasing amounts of KCl (30-100 mM). No two-state transition was observed for CD melting experiments at 0, 10 and 20 mM KCl.

In the absence of KCl, the AS1411-N5 does not seem to adopt a G4 topology as suggested by the positive band centred at around 280 nm, which is characteristic of single-stranded nucleic acids [65].

Upon titrating KCl into the AS1411-N5 solution, the formation of a parallel-stranded G4 seems to be induced, as was registered in AS1411-N5 and AS1411-N5T in Tris-HCl buffer. During titration an overall increase in ellipticity was observed together with the retention of the characteristic bands, suggesting a strong dependence on K^+ cations for the stabilization of the G4 structure. This was further corroborated by CD melting experiments discussed below.

The CD spectra obtained for AS1411-N5 is clearly different from that of AS1411 spectrum in potassium phosphate buffer described previously [111]. Also, comparing As1411 spectra profile obtained (presented in Section 1.1 of Part A) and the described in the literature to both Tris-HCl and potassium phosphate buffers, respectively, it is denoted an influence on CD profiles spectra and consequently in the secondary structure of aptamer [38], [57]. This difference can be justified by the polymorphism of AS1411 [54].

Figure 38B represents the CD melting curves with increasing KCl concentration. T_m was determined by monitoring the wavelength of maximum ellipticity at increasing temperatures. As suggested by the CD melting data, K^+ seems to stabilize the G4 structure increasing its T_m values from 20.9 °C ± 5.0 to 43.4 °C ± 0.3 at 30 and 100 mM KCl, respectively.

1.2 NMR Spectroscopy

After attesting that G4 is formed in AS1411-N5 we have performed ^{1}H NMR titrations at 20°C with increasing concentrations of KCl to study the cation effect in G4. The spectra are shown in Figure 39A.

As obtained with Tris-HCl buffer, with potassium phosphate buffer an increase of K^+, the ^{1}H NMR spectra show signals corresponding to the duplex (12.5 - 14 ppm) and the G4 structure (10 - 12 ppm), suggesting the formation of both structures simultaneously. Comparing both spectra, the similarities are many among well-defined sets of signals of G4 structure, agreeing with the suggestion of G4 structure lock in a single conformation.

In bidimensional spectra (NOESY), similarities are also established (Figure 39B). The theory that the duplex portion has a blocking effect on G4 structure is reinforced, as we know that the buffer difference can induce structural polymorphism. Thus, possibilities to structural determination are exponentially boosted, open a way to first three-dimensional determination of native AS1411 G4 sequence.

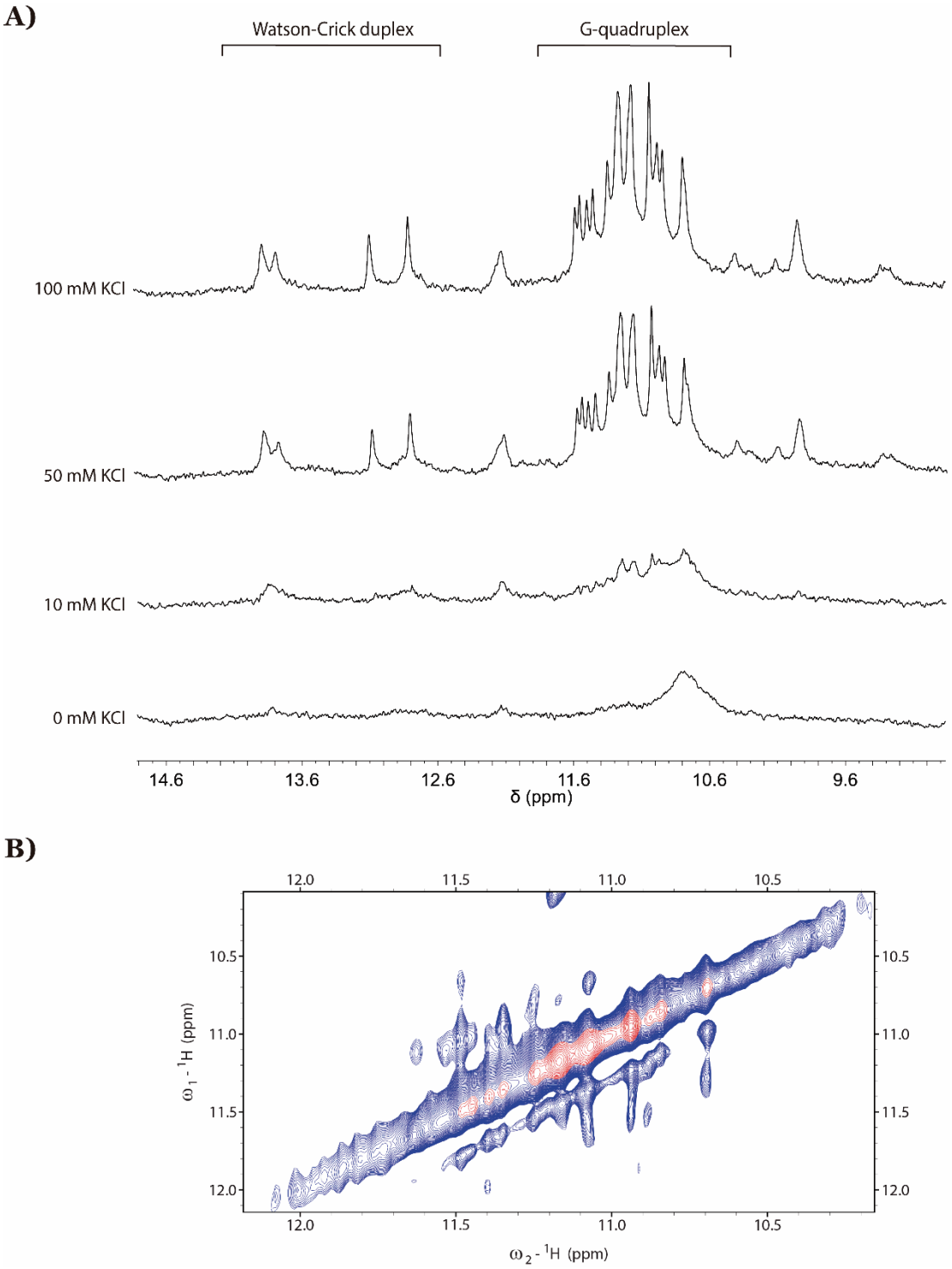

Figure 39. ^{1}H NMR titration of AS1411-N5 with increasing amounts of KCl salt. The sets of peaks corresponding to the duplex base pairing and the G4 structure as highlighted at the top. On the right, a schematic representation of the duplex/G4 hybrid showing the position of the fluorophores. The structure is merely representative and does not consider the actual topology and orientation of bases.

2. Studies of G4/Nucleolin Interaction

To follow experiments were carried out to study the interaction between AS1411-N5 and NCL RBD1,2 in potassium phosphate buffer.

2.1 CD Spectroscopy

Firstly, was performed a titration of NCL RBD1,2 into a solution of pre-folded G4 AS1411-N5 to evaluate the effect of NCL interaction on the G4 structure.

Possible evidence of interaction between NCL RBD1,2 and G4 AS1411-N5 was also demonstrated by the slight increase in the ellipticity at 260 nm in the spectrum (Figure 40).

Additionally, the idea of the RBD1,2 domain can undergo a conformational rearrangement in order to bind the G4 structure is also supported. Same variations on protein spectra were obtained in presence of G4 AS1411-N5 and show a signature of a β-sheet secondary structure, unlike in absence of G4 AS1411-N5, presents a typical α-helix secondary structure (Figure 32). These conclusions were also previously obtained in Part A, thus demonstrating a consistency of interaction among AS1411-N5/NCL.

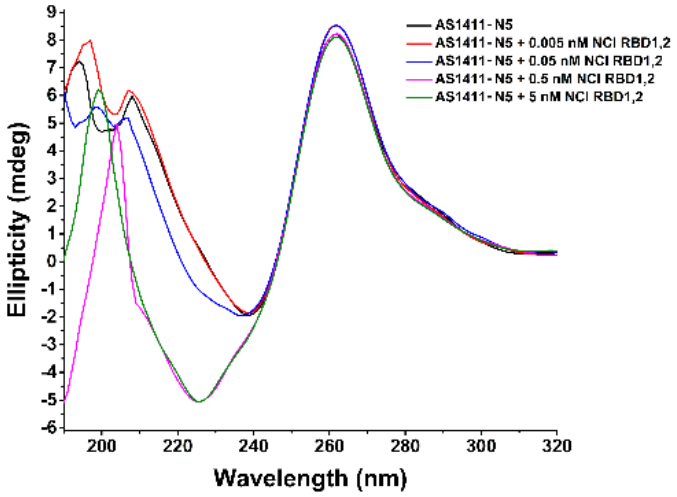

Figure 40. CD spectroscopy analysis of the interaction between AS1411-N5 G4 structure and NCL protein in the absence and presence of increasing amounts of NCL RBD1,2 (0-5 nM).

2.2 FRET-melting assays

The FRET melting experiments were carried out to determine the melting temperature of G4 AS1411-N5 with NCL RBD1,2. As a negative control, it was used BSA. These assays were performed in lithium cacodylate buffer because Li^+ has a neutral effect on G4 stability, unlike sodium cacodylate, where the Na^+ can modulate the stability or topology of G4 [108].

The obtained results perform a typical FRET-melting curve, mainly due to the influence of lithium buffer (Figure 41). After calculated the two-sate-transition point in

normalized data, was possible to conclude that T_m values of AS1411-N5 increase in the presence of increasing amounts of NCL RBD1,2.

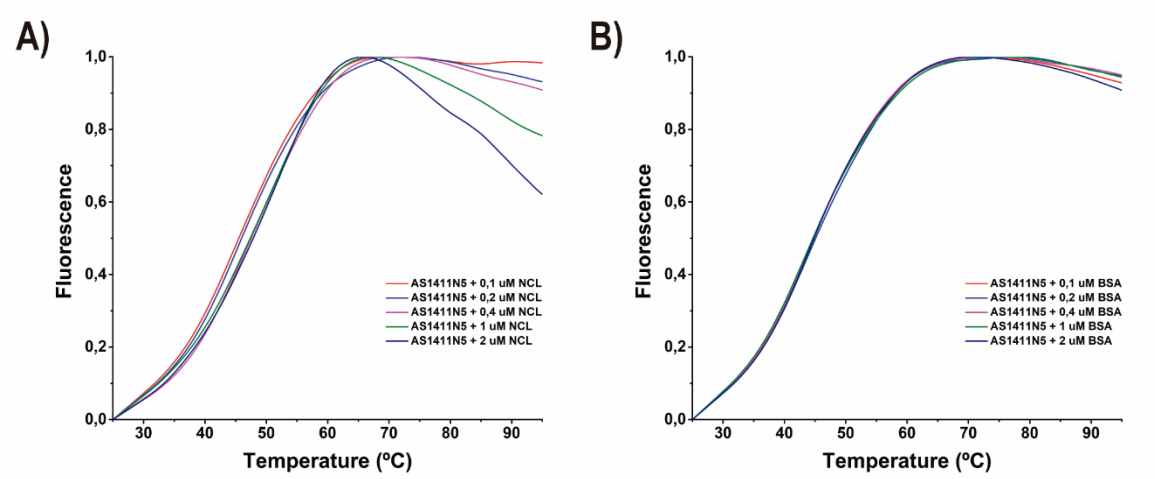

Figure 41. FRET-melting spectra of AS1411-N5 when incubated with NCL RBD1,2 and BSA with lithium cacodylate buffer.

As shown in Figure 41, NCL RBD1,2 has a stabilizing behaviour on the G4 AS1411-N5 structure, increasing its T_m values from 45.6 °C ± 0.1 to 47.4 °C ± 0.6 at 0.1 and 2 μM, respectively. Already, the decreasing of fluorescence in the spectrum, observed at high NCL RBD1,2 concentrations and temperatures remains unknown. Considering the importance of buffer composition in melting experiments discussed in Part A, it is hypothesised that the NCL buffer composition which has NaHEPES, can cause this effect. This buffer is also described by Mergny and Lacroix [108].

Unlike NCL RBD1,2, the negative control BSA did not show any stabilization effect in the G4 AS1411-N5 structure. T_m values were around 44.5 °C.

Similar results were observed during FRET-melting analysis of the stabilization of NCL RBD1,2 and BSA on the LTR G4 sequences [112]

2.3 Fluorescence Spectroscopy

Fluorescence spectroscopy was applied to assess the binding affinity of the AS1411-N5 to NCL RBD1,2. Fluorometric titrations were performed initially in the absence and the presence of increasing amounts of NCL RBD1,2. Fluorescence was recorded at 568 nm. Figure 42A displays the results.

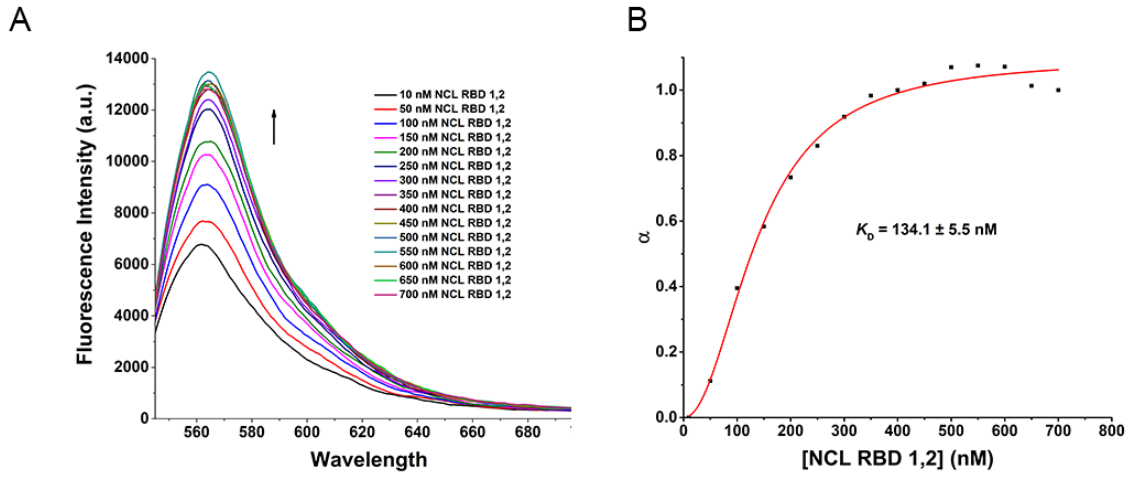

Figure 42. *Fluorescence titrations of the AS1411-N5 with increasing amounts of NCL RBD1,2. A) Fluorescence emission spectra of AS1411-N5 (1 μM) with increasing concentration of NCL in 10 mM potassium phosphate buffer, pH 6.9 containing 100 mM KCl. B) The fraction of ligand-bound plots fitted to the saturation binding equation (Hill equation).*

The values indicated a 2-fold increase in fluorescence units at saturating NCL RBD1,2 concentrations. This behaviour was also obtained in Part A. To denote that differences in fluorescence intensity can be explained due to the different refractive index of solutions, namely the buffers. The saturation binding plots were obtained by non-linear regression analysis (Hill equation) and are presented in Figure 42B. To highlight that it was used a different equation to do the fit and we have determined only one K_D. The K_D value for the binding interaction between the AS1411-N5 and NCL RBD1,2 was 138.1 ± 5.5 nM, indicating an affinity in the nanomolar range, in agreement with those previously reported in the literature and Part A.

2.4 In vitro assays

If NCL functions as a receptor for AS1411-N5 on PC3 cells, then it would be expected to be present on the surface of PCa cells. Thus, the colocalization and cellular uptake of the AS1411-N5 recognition probe in PC3 cells were evaluated by fluorescence confocal microscopy and depicted in Figure 43.

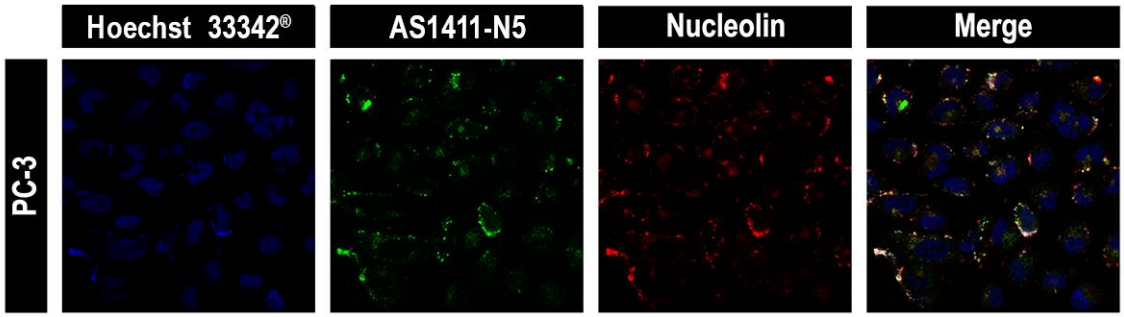

Figure 43. Confocal laser scanning microscopy images showing the colocalization of AS1411-N5 with NCL and the intracellular uptake of AS1411-N5 in PC3 cell line. For each panel, images showed the cells with

nuclear staining by Hoechst 33342® (1 μM, blue); AS1411-N5 (1 μM, green); and NCL (red). NCL was labelled with the primary anti- NCL polyclonal antibody (1:100) and detected with the secondary antibody against IgG conjugated with Alexa Fluor® 647 (1:1000).

The AS1411-N5 was localized through the intrinsic fluorescence of FAM. The primary anti-NCL antibody conjugated with the secondary antibody AlexaFluor 647® was used to localize cell surface NCL. Strong fluorescent signals were observed with the incubation of AS1411-N5 or NCL. Additionally, confocal microscopy indicated that AS1411-N5 appears to colocalize with NCL, suggesting their ability to recognize and bind NCL on the surface of PCa cells.

The results also confirmed the internalization of AS1411-N5 and its location in the cytoplasm, as previously reported for AS1411 [113]. The cellular uptake in the absence of any transfection agent, suggest a mechanism of internalization mediated by NCL. As NCL acts as a shuttling protein between the plasma membrane, cytoplasm, and nucleus [63], the AS1411-N5 would also be transported by NCL not only to the cytoplasm but also to the cell nucleus.

2.5 Microfluidic experiments

Once the suitability of using G4 AS1411-N5 as a capture probe was demonstrated, was fabricated a miniaturized NCL detection system for fast, low cost and user-friendly analyte monitoring.

The coming experiments were performed following the same methodology: i) beads are first packed in the microfluidic channel; ii) the capture G4 AS1411-N5 probe is incubated with the analyte sample in a tube; iii) the sample mixture has flowed through the beads channel and the fluorescence was recorded.

Firstly, the microfluidic device was used to detect NCL RBD1,2 from a purified sample. As seen from Figure 44, a significant fluorescence signal was detected when 5 μM NCL RBD1,2 was incubated with AS1411-N5 capturing probe. The signal was considered as being NCL RBD1,2-dependent as no signal was obtained when the probe alone was flowed in the pre-packed microchannel (blank), further indicating that there was no nonspecific adsorption of AS1411-N5 in the beads. The retention of NCL RBD1,2 onto the beads is to be due to electrostatic interactions given the cation exchange nature, promoted by carboxymethyl group on surface beads, of the CM Sephadex C-25 beads used.

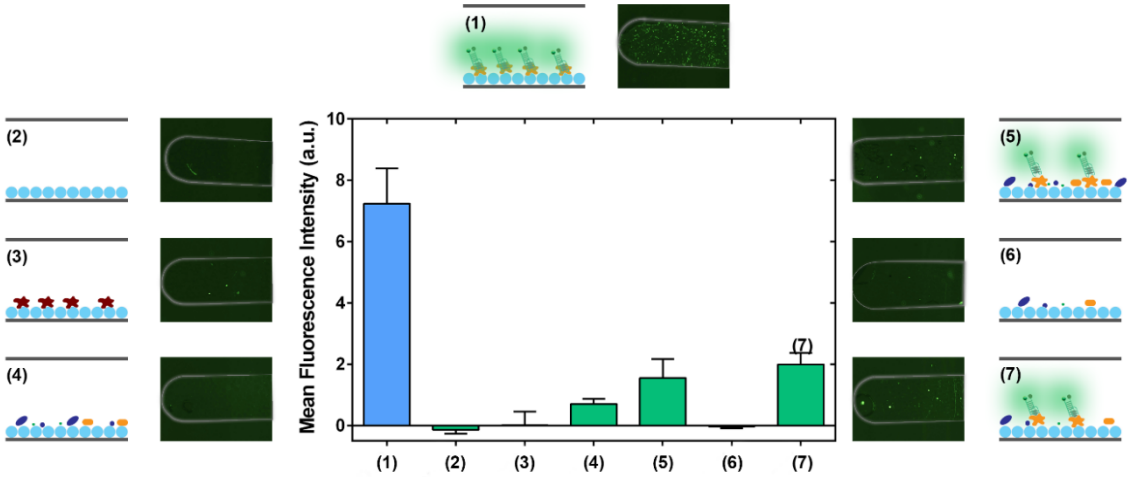

Figure 44. Selectivity studies for NCL measurement with AS1411-N5. (1) Fluorescence signal change when the complex NCL RBD1,2 /AS1411-N5 was flowed. (2) Control with AS1411-N5 at 1 μM. (3) Fluorescence signal change when PSA and AS1411-N5 was flowed. (4) Fluorescence signal change when plasma and AS1411-N5 was flowed. (5) Fluorescence signal change when plasma spiked with NCL RBD1,2 was flowed together with AS1411-N5. (6) Fluorescence signal change when diluted plasma (50%) and AS1411-N5 was flowed. (7) Fluorescence signal change when diluted plasma (50%) spiked with NCL RBD1,2 was flowed together with AS1411-N5.

As the development of a reliable biosensor and its potential applications depends on its selectivity, PSA protein was also used to assess whether the capturing probe was selective in the presence of other PCa relevant targets. The results shown in Figure 44 suggest that the probe did not recognize PSA at the same concentration used for NCL RBD1,2 (5 μM), showing the specificity of AS1411-N5 towards NCL RBD1,2.

Indeed, the probe was designed based on AS1411 sequence which is known for its specificity towards NCL protein [114] and the fact that the introduction of a duplex portion locks the G4 structure in a single conformation may enhance its specificity towards NCL.

From a PoC perspective, the NCL microfluidic detection system should allow and withstand the use of biological samples. Therefore, was tested human plasma samples non-spiked and spiked with NCL RBD1,2 to test the feasibility of using this microfluidic platform for the detection of NCL in liquid biological samples.

Full plasma presented low detectable fluorescence probably due to unspecific interactions with plasma constituents, yet significantly lower than NCL fluorescence. It should be noted that blood plasma is crowded with biomacromolecules (~ 100 mg/mL) [115]. This becomes evident when plasma was diluted 1:1 with buffer and the unspecific fluorescence was lowered to residual levels. Remarkably, in both cases (full and diluted plasma), when plasma samples were spiked with NCL RBD1,2 at 5 μM, a significant increase in the fluorescence was detected to a similar extent.

Compared to other described devices for protein detection [116], [117], this strategy is also able to detect NCL with desirable selectivity and specificity in complex biological samples. This shows the potential of using this approach to detect NCL in biological samples.

Chapter 5

Conclusions and Future Perspectives

The work proposed a new PoC microfluidic platform based on a derivative of the AS1411 sequence. This sequence was extended by the addition of five nucleotides to the 5' and 3'-end to achieve a stem-loop structure, and at each end were added a fluorophore (FAM) and a quencher (DABCYL). This molecular system has the NCL protein as a target which is highly expressed on the membrane of PCa cells.

Through the biophysical characterization, namely using CD spectroscopy, was observed the formation of a parallel-stranded G4 topology in the AS1411-N5 sequence, induced by K^+. NMR spectroscopy revealed important structural features such as the formation of a single major AS1411-N5 G4 conformation in presence of 100 mM K^+.

Was also have checked and demonstrated the interaction between G4 AS1411-N5 and NCL RBD1,2 by FRET-melting experiments. The fluorescence spectroscopy studies showed a strong affinity of G4 AS1411-N5 towards NCL RBD1,2 (K_D = 138.1 ± 5.5 nM). The colocalization of AS1411-N5 with NCL and its cellular uptake into PC3 cells were studied by confocal microscopy

Finally, the microfluidic assays proved the potential of using this approach to detect NCL with specificity and selectivity in biological samples such as human plasma of patients with a diagnosis of PCa. Altogether, these results pave the way for the development of a PoC device for the detection of NCL in human liquid biopsies, contributing to the advance of the state-of-art PCa diagnosis methods.

As future perspectives, experimental validation should be considered. First of all, structural characterization of G4 AS1411-N5, by several methods as NMR or crystallography, keep being highlighted. This will be important to allow computational modelling of AS1411-N5 with NCL RBD1,2. Additionally, can be useful to determine a first three-dimensional characterization of AS1411 aptamer without modifications in the middle of the native sequence. Furthermore, other techniques can be used, namely surface plasmon resonance or calorimetry, to optimize thermodynamic and kinetic parameters.

As future innovation, the alliance among the signalization/diagnostics approach, presented in this dissertation, with therapeutics can be performed. Thus, we would have a theragnostic system, that in the recognition moment of target produce fluorescence, and then deliver the drug.

References

[1] P. Verze, T. Cai, and S. Lorenzetti, 'The role of the prostate in male fertility, health and disease', *Nat. Rev. Urol.*, vol. 13, no. 7, pp. 379–386, Jul. 2016, doi: 10.1038/nrurol.2016.89.

[2] S. W. Hayward and G. R. Cunha, 'The prostate: development and physiology', *Radiol. Clin. North Am.*, vol. 38, no. 1, pp. 1–14, Jan. 2000, doi: 10.1016/S0033-8389(05)70146-9.

[3] A. R. Mundy, J. M. Fitzpatrick, D. E. Neal, and N. J. R. George, *The Scientific Basis of Urology*, 1st ed. Oxford: CRC Press, 1999.

[4] L. Aaron, O. Franco, and S. W. Hayward, 'Review of Prostate Anatomy and Embryology and the Etiology of BPH', *Urol Clin North Am*, vol. 43, no. 3, pp. 279–288, 2016, doi: 10.1016/j.ucl.2016.04.012.Review.

[5] M. Ittmann, 'Anatomy and Histology of the Human and Murine Prostate', *Cold Spring Harb. Perspect. Med.*, vol. 8, no. 5, p. a030346, May 2018, doi: 10.1101/cshperspect.a030346.

[6] R. Toivanen and M. M. Shen, 'Prostate organogenesis: tissue induction, hormonal regulation and cell type specification', *Development*, vol. 144, no. 8, pp. 1382–1398, Apr. 2017, doi: 10.1242/dev.148270.

[7] C. L. VanPutte, J. L. Regan, and A. F. Russo, *Seeley's Anatomy & Physiology*, 10th ed., vol. 2. New York, 2017.

[8] A. W. Partin, R. R. Dmochowski, L. R. Kavoussi, and C. A. Peters, *Campbell-Walsh-Wein Urology*, 12th ed. Philadelphia, PA 19103-2899: Elsevier, 2020.

[9] B. G. Timms, 'Prostate development: A historical perspective', *Differentiation*, vol. 76, no. 6, pp. 565–577, 2008, doi: 10.1111/j.1432-0436.2008.00278.x.

[10] J. C. Francis and A. Swain, 'Prostate Organogenesis', *Cold Spring Harb. Perspect. Med.*, vol. 8, no. 7, p. a030353, Jul. 2018, doi: 10.1101/cshperspect.a030353.

[11] G. H. Henry *et al.*, 'A Cellular Anatomy of the Normal Adult Human Prostate and Prostatic Urethra', *Cell Rep.*, vol. 25, no. 12, pp. 3530-3542.e5, Dec. 2018, doi: 10.1016/j.celrep.2018.11.086.

[12] C. H. Lee, O. Akin-Olugbade, and A. Kirschenbaum, 'Overview of Prostate Anatomy, Histology, and Pathology', *Endocrinol. Metab. Clin. North Am.*, vol. 40, no. 3, pp. 565–575, Sep. 2011, doi: 10.1016/j.ecl.2011.05.012.

[13] G. C. Observatory, 'Global Cancer Observatory', 2018. https://gco.iarc.fr/today/home (accessed Apr. 12, 2020).

[14] H. Schatten, *Cell & Molecular Biology Of Prostate Cancer: Updates, Insights and New Frontiers*, 1st ed. Gewerbestrasse 11, 6330 Cham, Switzerland: Springer, 2018.

[15] G. Wang, D. Zhao, D. J. Spring, and R. A. DePinho, 'Genetics and biology of prostate cancer', *Genes Dev.*, vol. 32, no. 17–18, pp. 1105–1140, Sep. 2018, doi: 10.1101/gad.315739.118.

[16] J. Ferlay *et al.*, 'Cancer incidence and mortality patterns in Europe: Estimates for 40 countries and 25 major cancers in 2018', *Eur. J. Cancer*, vol. 103, pp. 356–387, Nov. 2018, doi: 10.1016/j.ejca.2018.07.005.

[17] I. N. de Estatística, *Estatísticas da Saúde - 2018*, 1st ed. Lisboa: Estatística, Instituto Nacional de, 2020.

[18] H. E. Taitt, 'Global Trends and Prostate Cancer: A Review of Incidence, Detection, and Mortality as Influenced by Race, Ethnicity, and Geographic Location', *Am. J. Mens. Health*, vol. 12, no. 6, pp. 1807–1823, 2018, doi: 10.1177/1557988318798279.

[19] T. Swallow, S. Chowdhury, and R. S. Kirby, 'Cancer of the prostate gland', *Medicine (Baltimore).*, vol. 40, no. 1, pp. 10–13, Jan. 2012, doi: 10.1016/j.mpmed.2011.09.002.

[20] T. R. Rebbeck, 'Prostate Cancer Genetics: Variation by Race, Ethnicity, and Geography', *Semin. Radiat. Oncol.*, vol. 27, no. 1, pp. 3–10, Jan. 2017, doi: 10.1016/j.semradonc.2016.08.002.

[21] T. Grozescu and F. Popa, 'Prostate cancer between prognosis and adequate/proper therapy', *J. Med. Life*, vol. 10, no. 1, pp. 5–12, 2017, [Online]. Available: http://www.ncbi.nlm.nih.gov/pubmed/28255369%0Ahttp://www.pubmedcentral.nih.gov/articlerender.fcgi?artid=PMC5304372.

[22] M. J. Barry and L. H. Simmons, 'Prevention of Prostate Cancer Morbidity and Mortality', *Med. Clin. North Am.*, vol. 101, no. 4, pp. 787–806, Jul. 2017, doi: 10.1016/j.mcna.2017.03.009.

[23] P. Dasgupta, R. S. Kirby, and P. T. Sacardino, *ABC of Prostate Cancer*, 1st ed. Chichester, West Sussex, PO19 8SQ, UK: Wiley-Blackwell, 2012.

[24] A. C. Society, 'Prostate Cancer | Prostate Cancer Information and Overview', 2020. https://www.cancer.org/cancer/prostate-cancer.html (accessed Apr. 13, 2020).

[25] G. Attard *et al.*, 'Prostate cancer', *Lancet*, vol. 387, no. 10013, pp. 70–82, Jan. 2016, doi: 10.1016/S0140-6736(14)61947-4.

[26] C. H. Pernar, E. M. Ebot, K. M. Wilson, and L. A. Mucci, 'The Epidemiology of Prostate Cancer', *Cold Spring Harb. Perspect. Med.*, vol. 8, no. 12, p. a030361, Dec. 2018, doi: 10.1101/cshperspect.a030361.

[27] S. Saini *et al.*, 'PSA and beyond: alternative prostate cancer biomarkers', *Med. Clin. North Am.*, vol. 39, no. 1, pp. 97–106, 2016, doi: 10.1016/j.mcna.2017.03.009.

[28] S. Neidle and S. Balasubramanian, *Quadruplex Nucleic Acids*, 1st ed. Cambridge: Cambridge University Press, 2006.

[29] D. L. Nelson and M. M. Cox, *Lehninger - Principles of Biochemistry*, 6th ed. New York:

W. H. Freeman and Company, 2013.

[30] J. D. WATSON and F. H. C. CRICK, 'Molecular Structure of Nucleic Acids: A Structure for Deoxyribose Nucleic Acid', *Nature*, vol. 171, no. 4356, pp. 737–738, Apr. 1953, doi: 10.1038/171737a0.

[31] P. Belmont, J. F. Constant, and M. Demeunynck, 'Nucleic acid conformation diversity: from structure to function and regulation', *Chem. Soc. Rev.*, vol. 30, no. 1, pp. 70–81, 2001, doi: 10.1039/a904630e.

[32] A. Bacolla and R. D. Wells, 'Non-B DNA Conformations, Genomic Rearrangements, and Human Disease', *J. Biol. Chem.*, vol. 279, no. 46, pp. 47411–47414, Nov. 2004, doi: 10.1074/jbc.R400028200.

[33] C. K. Kwok and C. J. Merrick, 'G-Quadruplexes: Prediction, Characterization, and Biological Application', *Trends Biotechnol.*, vol. 35, no. 10, pp. 997–1013, Oct. 2017, doi: 10.1016/j.tibtech.2017.06.012.

[34] H. A. Day, P. Pavlou, and Z. A. E. Waller, 'i-Motif DNA: Structure, stability and targeting with ligands', *Bioorg. Med. Chem.*, vol. 22, no. 16, pp. 4407–4418, Aug. 2014, doi: 10.1016/j.bmc.2014.05.047.

[35] M. Zeraati *et al.*, 'I-motif DNA structures are formed in the nuclei of human cells', *Nat. Chem.*, vol. 10, no. 6, pp. 631–637, Jun. 2018, doi: 10.1038/s41557-018-0046-3.

[36] J. Spiegel, S. Adhikari, and S. Balasubramanian, 'The Structure and Function of DNA G-Quadruplexes', *Trends Chem.*, vol. 2, no. 2, pp. 123–136, Feb. 2020, doi: 10.1016/j.trechm.2019.07.002.

[37] D. Bhattacharyya, G. Mirihana Arachchilage, and S. Basu, 'Metal Cations in G-Quadruplex Folding and Stability', *Front. Chem.*, vol. 4, no. SEP, pp. 1–14, Sep. 2016, doi: 10.3389/fchem.2016.00038.

[38] M. Kaushik *et al.*, 'A bouquet of DNA structures: Emerging diversity', *Biochem. Biophys. Reports*, vol. 5, pp. 388–395, Mar. 2016, doi: 10.1016/j.bbrep.2016.01.013.

[39] J. T. Davis, 'G-Quartets 40 Years Later: From 5′-GMP to Molecular Biology and Supramolecular Chemistry', *Angew. Chemie Int. Ed.*, vol. 43, no. 6, pp. 668–698, Jan. 2004, doi: 10.1002/anie.200300589.

[40] K. C. Liu, K. Röder, C. Mayer, S. Adhikari, D. J. Wales, and S. Balasubramanian, 'Affinity-Selected Bicyclic Peptide G-Quadruplex Ligands Mimic a Protein-like Binding Mechanism', *J. Am. Chem. Soc.*, vol. 142, no. 18, pp. 8367–8373, May 2020, doi: 10.1021/jacs.0c01879.

[41] J.-L. Mergny and D. Sen, 'DNA Quadruple Helices in Nanotechnology', *Chem. Rev.*, vol. 119, no. 10, Jan. 2019, doi: 10.1021/acs.chemrev.8b00629.

[42] A. Pandith, R. G. Siddappa, and Y. J. Seo, 'Recent developments in novel blue/green/red/NIR small fluorescent probes for in cellulo tracking of RNA/DNA G-

quadruplexes', *J. Photochem. Photobiol. C Photochem. Rev.*, vol. 40, pp. 81–116, Sep. 2019, doi: 10.1016/j.jphotochemrev.2019.08.001.

[43] Y. Ma, K. Iida, and K. Nagasawa, 'Topologies of G-quadruplex: Biological functions and regulation by ligands', *Biochem. Biophys. Res. Commun.*, vol. 1051, Jan. 2020, doi: 10.1016/j.bbrc.2019.12.103.

[44] M. Sharawy and S. Consta, 'Effect of the chemical environment of the DNA guanine quadruplex on the free energy of binding of Na and K ions', *J. Chem. Phys.*, vol. 149, no. 22, p. 225102, Dec. 2018, doi: 10.1063/1.5050534.

[45] J. T. Davis, 'G-Quartets 40 Years Later: From 5′-GMP to Molecular Biology and Supramolecular Chemistry', *Angew. Chemie - Int. Ed.*, vol. 43, no. 6, pp. 668–698, 2004, doi: 10.1002/anie.200300589.

[46] J. L. Huppert, 'Four-stranded nucleic acids: structure, function and targeting of G-quadruplexes', *Chem. Soc. Rev.*, vol. 37, no. 7, p. 1375, 2008, doi: 10.1039/b702491f.

[47] T. Fujii, P. Podbevšek, J. Plavec, and N. Sugimoto, 'Effects of metal ions and cosolutes on G-quadruplex topology', *J. Inorg. Biochem.*, vol. 166, pp. 190–198, Jan. 2017, doi: 10.1016/j.jinorgbio.2016.09.001.

[48] H. L. Lightfoot, T. Hagen, N. J. Tatum, and J. Hall, 'The diverse structural landscape of quadruplexes', *FEBS Lett.*, vol. 593, no. 16, pp. 2083–2102, Aug. 2019, doi: 10.1002/1873-3468.13547.

[49] M. Popenda, J. Miskiewicz, J. Sarzynska, T. Zok, and M. Szachniuk, 'Topology-based classification of tetrads and quadruplex structures', *Bioinformatics*, vol. 36, no. 4, pp. 1129–1134, Feb. 2020, doi: 10.1093/bioinformatics/btz738.

[50] S. Burge, G. N. Parkinson, P. Hazel, A. K. Todd, and S. Neidle, 'Quadruplex DNA: sequence, topology and structure', *Nucleic Acids Res.*, vol. 34, no. 19, pp. 5402–5415, Nov. 2006, doi: 10.1093/nar/gkl655.

[51] R. W. Harkness and A. K. Mittermaier, 'G-quadruplex dynamics', *Biochim. Biophys. Acta - Proteins Proteomics*, vol. 1865, no. 11, pp. 1544–1554, Nov. 2017, doi: 10.1016/j.bbapap.2017.06.012.

[52] S. Asamitsu, M. Takeuchi, S. Ikenoshita, Y. Imai, H. Kashiwagi, and N. Shioda, 'Perspectives for Applying G-Quadruplex Structures in Neurobiology and Neuropharmacology', *Int. J. Mol. Sci.*, vol. 20, no. 12, p. 2884, Jun. 2019, doi: 10.3390/ijms20122884.

[53] J. Filitcheva, P. J. B. Edwards, G. E. Norris, and V. V. Filichev, 'α-2′-Deoxyguanosine can switch DNA G-quadruplex topologies from antiparallel to parallel', *Org. Biomol. Chem.*, vol. 17, no. 16, pp. 4031–4042, 2019, doi: 10.1039/C9OB00360F.

[54] C. Roxo, W. Kotkowiak, and A. Pasternak, 'G-Quadruplex-Forming Aptamers—Characteristics, Applications, and Perspectives', *Molecules*, vol. 24, no. 20, p. 3781, Oct.

2019, doi: 10.3390/molecules24203781.

[55] S. M. Nimjee, R. R. White, R. C. Becker, and B. A. Sullenger, 'Aptamers as Therapeutics', *Annu. Rev. Pharmacol. Toxicol.*, vol. 57, no. 1, pp. 61–79, Jan. 2017, doi: 10.1146/annurev-pharmtox-010716-104558.

[56] S. Romano, N. Fonseca, S. Simões, J. Gonçalves, and J. N. Moreira, 'Nucleolin-based targeting strategies for cancer therapy: from targeted drug delivery to cytotoxic ligands', *Drug Discov. Today*, vol. 24, no. 10, pp. 1985–2001, Oct. 2019, doi: 10.1016/j.drudis.2019.06.018.

[57] P. J. Bates, E. M. Reyes-Reyes, M. T. Malik, E. M. Murphy, M. G. O'Toole, and J. O. Trent, 'G-quadruplex oligonucleotide AS1411 as a cancer-targeting agent: Uses and mechanisms', *Biochim. Biophys. Acta - Gen. Subj.*, vol. 1861, no. 5, pp. 1414–1428, May 2017, doi: 10.1016/j.bbagen.2016.12.015.

[58] P. J. Bates, D. A. Laber, D. M. Miller, S. D. Thomas, and J. O. Trent, 'Discovery and development of the G-rich oligonucleotide AS1411 as a novel treatment for cancer', *Exp. Mol. Pathol.*, vol. 86, no. 3, pp. 151–164, Jun. 2009, doi: 10.1016/j.yexmp.2009.01.004.

[59] M. M. Dailey, M. C. Miller, P. J. Bates, A. N. Lane, and J. O. Trent, 'Resolution and characterization of the structural polymorphism of a single quadruplex-forming sequence', *Nucleic Acids Res.*, vol. 38, no. 14, pp. 4877–4888, 2010, doi: 10.1093/nar/gkq166.

[60] I. Ugrinova, M. Petrova, M. Chalabi-Dchar, and P. Bouvet, 'Multifaceted Nucleolin Protein and Its Molecular Partners in Oncogenesis', in *Advances in Protein Chemistry and Structural Biology*, 1st ed., vol. 111, Elsevier Inc., 2018, pp. 133–164.

[61] W. Jia, Z. Yao, J. Zhao, Q. Guan, and L. Gao, 'New perspectives of physiological and pathological functions of nucleolin (NCL)', *Life Sci.*, vol. 186, no. May, pp. 1–10, Oct. 2017, doi: 10.1016/j.lfs.2017.07.025.

[62] M. Masiuk, M. Lewandowska, E. Dobak, and E. Urasinska, 'Nucleolin and Nucleophosmin Expression in Gleason 3 and Gleason 4 Prostate Cancer With Seminal Vesicles Invasion (pT3b)', *Anticancer Res.*, vol. 40, no. 4, pp. 1973–1979, Apr. 2020, doi: 10.21873/anticanres.14152.

[63] A. G. Hovanessian *et al.*, 'The Cell-Surface-Expressed Nucleolin Is Associated with the Actin Cytoskeleton', *Exp. Cell Res.*, vol. 261, no. 2, pp. 312–328, Dec. 2000, doi: 10.1006/excr.2000.5071.

[64] D. Yang and C. Lin, *G-Quadruplex Nucleic Acids*, 1st ed., vol. 2035. New York, NY: Springer New York, 2019.

[65] E. Largy, J.-L. Mergny, and V. Gabelica, *The Alkali Metal Ions: Their Role for Life*, 1st ed., vol. 16. Cham: Springer International Publishing, 2016.

[66] N. Campbell, G. W. Collie, and S. Neidle, 'Crystallography of DNA and RNA

G-Quadruplex Nucleic Acids and Their Ligand Complexes', *Curr. Protoc. Nucleic Acid Chem.*, vol. 50, no. 1, Sep. 2012, doi: 10.1002/0471142700.nc1706s50.

[67] M. Adrian, B. Heddi, and A. T. Phan, 'NMR spectroscopy of G-quadruplexes', *Methods*, vol. 57, no. 1, pp. 11–24, May 2012, doi: 10.1016/j.ymeth.2012.05.003.

[68] M. Webba da Silva, 'NMR methods for studying quadruplex nucleic acids', *Methods*, vol. 43, no. 4, pp. 264–277, Dec. 2007, doi: 10.1016/j.ymeth.2007.05.007.

[69] G. Yuan, Q. Zhang, J. Zhou, and H. Li, 'Mass spectrometry of G-quadruplex DNA: Formation, recognition, property, conversion, and conformation', *Mass Spectrom. Rev.*, vol. 30, no. 6, pp. 1121–1142, Nov. 2011, doi: 10.1002/mas.20315.

[70] J. Carvalho, J. A. Queiroz, and C. Cruz, 'Circular Dichroism of G-Quadruplex: a Laboratory Experiment for the Study of Topology and Ligand Binding', *J. Chem. Educ.*, vol. 94, no. 10, pp. 1547–1551, Oct. 2017, doi: 10.1021/acs.jchemed.7b00160.

[71] J. Carvalho and C. Cruz, 'Forster resonance energy transfer for studying nucleic acids denaturation: A chemical and biological sciences laboratory experiment', *Biochem. Mol. Biol. Educ.*, no. February, pp. 1–8, Apr. 2020, doi: 10.1002/bmb.21353.

[72] A. Moutsiopoulou, D. Broyles, E. Dikici, S. Daunert, and S. K. Deo, 'Molecular Aptamer Beacons and Their Applications in Sensing, Imaging, and Diagnostics', *Small*, vol. 15, no. 35, p. 1902248, Aug. 2019, doi: 10.1002/smll.201902248.

[73] J. E. Ladbury and B. Z. Chowdhry, 'Sensing the heat: the application of isothermal titration calorimetry to thermodynamic studies of biomolecular interactions', *Chem. Biol.*, vol. 3, no. 10, pp. 791–801, Oct. 1996, doi: 10.1016/S1074-5521(96)90063-0.

[74] S. Tyagi and F. R. Kramer, 'Molecular Beacons: Probes that Fluoresce upon Hybridization', *Nat. Biotechnol.*, vol. 14, no. 3, pp. 303–308, Mar. 1996, doi: 10.1038/nbt0396-303.

[75] C. J. Yang and W. Tan, 'Molecular beacons', *Mol. Beacons*, no. 8, pp. 1–194, 2013, doi: 10.1007/978-3-642-39109-5.

[76] N. Hamaguchi, A. Ellington, and M. Stanton, 'Aptamer Beacons for the Direct Detection of Proteins', *Anal. Biochem.*, vol. 294, no. 2, pp. 126–131, Jul. 2001, doi: 10.1006/abio.2001.5169.

[77] S.-X. Han, X. Jia, J. Ma, and Q. Zhu, 'Molecular Beacons: A Novel Optical Diagnostic Tool', *Arch. Immunol. Ther. Exp. (Warsz).*, vol. 61, no. 2, pp. 139–148, Apr. 2013, doi: 10.1007/s00005-012-0209-7.

[78] G. Luka *et al.*, 'Microfluidics Integrated Biosensors: A Leading Technology towards Lab-on-a-Chip and Sensing Applications', *Sensors*, vol. 15, no. 12, pp. 30011–30031, Dec. 2015, doi: 10.3390/s151229783.

[79] B. Srinivasan and S. Tung, 'Development and Applications of Portable Biosensors', *J. Lab. Autom.*, vol. 20, no. 4, pp. 365–389, Aug. 2015, doi: 10.1177/2211068215581349.

[80] R. S. Marks, D. C. Cullen, I. Karube, C. R. Lowe, and H. H. Weetall, *Handbook of Biosensors and Biochips*, 1st ed., vol. 26, no. 1. John Wiley & Sons, Ltd., 2008.

[81] A. P. F. Turner, 'Biosensors: sense and sensibility', *Chem. Soc. Rev.*, vol. 42, no. 8, p. 3184, Mar. 2013, doi: 10.1039/c3cs35528d.

[82] N. Bhalla, P. Jolly, N. Formisano, and P. Estrela, 'Introduction to biosensors', in *Biosensor Technologies for Detection of Biomolecules*, 1st ed., vol. 60, no. 1, P. Estrela, Ed. London: Portland Press, 2016, pp. 1–8.

[83] C. Justino, A. Duarte, and T. Rocha-Santos, 'Recent Progress in Biosensors for Environmental Monitoring: A Review', *Sensors*, vol. 17, no. 12, p. 2918, Dec. 2017, doi: 10.3390/s17122918.

[84] J. Kim, A. S. Campbell, B. E.-F. de Ávila, and J. Wang, 'Wearable biosensors for healthcare monitoring', *Nat. Biotechnol.*, vol. 37, no. 4, pp. 389–406, Apr. 2019, doi: 10.1038/s41587-019-0045-y.

[85] N. Gupta, V. Renugopalakrishnan, D. Liepmann, R. Paulmurugan, and B. D. Malhotra, 'Cell-based biosensors: Recent trends, challenges and future perspectives', *Biosens. Bioelectron.*, vol. 141, no. June, p. 111435, Sep. 2019, doi: 10.1016/j.bios.2019.111435.

[86] X. Jiang, C. Bai, and M. Liu, *Nanotechnology and Microfluidics*, 1st ed. Weinheim, Germany: Wiley-VCH, 2020.

[87] T. Baldacchini, 'Three-Dimensional Microfabrication by Two-Photon Polymerization', *Gener. Micro- Nanopatterns Polym. Mater.*, pp. 107–140, Mar. 2011, doi: 10.1002/9783527633449.ch7.

[88] N. Bhalla, H.-J. Chiang, and A. Q. Shen, 'Cell biology at the interface of nanobiosensors and microfluidics', in *Methods in Cell Biology*, 1st ed., vol. 148, Elsevier Inc., 2018, pp. 203–227.

[89] C. K. Dixit and A. Kaushik, *Microfluidics for Biologists: Fundamentals and Applications*, 1st ed. Cham: Springer International Publishing, 2016.

[90] G. M. Whitesides, 'The origins and the future of microfluidics', *Nature*, vol. 442, no. 7101, pp. 368–373, Jul. 2006, doi: 10.1038/nature05058.

[91] M. I. H. Ansari, S. Hassan, A. Qurashi, and F. A. Khanday, 'Microfluidic-integrated DNA nanobiosensors', *Biosens. Bioelectron.*, vol. 85, pp. 247–260, Nov. 2016, doi: 10.1016/j.bios.2016.05.009.

[92] N. Convery and N. Gadegaard, '30 years of microfluidics', *Micro Nano Eng.*, vol. 2, no. May 2018, pp. 76–91, Mar. 2019, doi: 10.1016/j.mne.2019.01.003.

[93] E. K. Sackmann, A. L. Fulton, and D. J. Beebe, 'The present and future role of microfluidics in biomedical research', *Nature*, vol. 507, no. 7491, pp. 181–189, Mar. 2014, doi: 10.1038/nature13118.

[94] I. F. Pinto *et al.*, 'The application of microbeads to microfluidic systems for enhanced

detection and purification of biomolecules', *Methods*, vol. 116, pp. 112–124, Mar. 2017, doi: 10.1016/j.ymeth.2016.12.005.

[95] S. Kumar *et al.*, 'Microfluidic-integrated biosensors: Prospects for point-of-care diagnostics', *Biotechnol. J.*, vol. 8, no. 11, pp. 1267–1279, Nov. 2013, doi: 10.1002/biot.201200386.

[96] C. M. Pandey *et al.*, 'Microfluidics Based Point-of-Care Diagnostics', *Biotechnol. J.*, vol. 13, no. 1, p. 1700047, Jan. 2018, doi: 10.1002/biot.201700047.

[97] S. N. Bhatia and D. E. Ingber, 'Microfluidic organs-on-chips', *Nat. Biotechnol.*, vol. 32, no. 8, pp. 760–772, Aug. 2014, doi: 10.1038/nbt.2989.

[98] E. M. Reyes-Reyes, F. R. Šalipur, M. Shams, M. K. Forsthoefel, and P. J. Bates, 'Mechanistic studies of anticancer aptamer AS1411 reveal a novel role for nucleolin in regulating Rac1 activation', *Mol. Oncol.*, vol. 9, no. 7, pp. 1392–1405, Aug. 2015, doi: 10.1016/j.molonc.2015.03.012.

[99] L. Farzin, M. Shamsipur, L. Samandari, and S. Sheibani, 'Signalling probe displacement electrochemical aptasensor for malignant cell surface nucleolin as a breast cancer biomarker based on gold nanoparticle decorated hydroxyapatite nanorods and silver nanoparticle labels', *Microchim. Acta*, vol. 185, no. 2, p. 154, Feb. 2018, doi: 10.1007/s00604-018-2700-2.

[100] L. Feng, Y. Chen, J. Ren, and X. Qu, 'A graphene functionalized electrochemical aptasensor for selective label-free detection of cancer cells', *Biomaterials*, vol. 32, no. 11, pp. 2930–2937, Apr. 2011, doi: 10.1016/j.biomaterials.2011.01.002.

[101] D. W. Hwang *et al.*, 'A Nucleolin-Targeted Multimodal Nanoparticle Imaging Probe for Tracking Cancer Cells Using an Aptamer', *J. Nucl. Med.*, vol. 51, no. 1, pp. 98–105, Jan. 2010, doi: 10.2967/jnumed.109.069880.

[102] J. J. Li, X. Fang, and W. Tan, 'Molecular Aptamer Beacons for Real-Time Protein Recognition', *Biochem. Biophys. Res. Commun.*, vol. 292, no. 1, pp. 31–40, Mar. 2002, doi: 10.1006/bbrc.2002.6581.

[103] J. Carvalho *et al.*, 'Aptamer-guided acridine derivatives for cervical cancer', *Org. Biomol. Chem.*, vol. 17, no. 11, pp. 2992–3002, Mar. 2019, doi: 10.1039/C9OB00318E.

[104] N. Q. Do, W. J. Chung, T. H. A. Truong, B. Heddi, and A. T. Phan, 'G-quadruplex structure of an anti-proliferative DNA sequence', *Nucleic Acids Res.*, vol. 45, no. 12, pp. 7487–7493, Jul. 2017, doi: 10.1093/nar/gkx274.

[105] B. A. Bondesen and M. D. Schuh, 'Circular Dichroism of Globular Proteins', *J. Chem. Educ.*, vol. 78, no. 9, p. 1244, Sep. 2001, doi: 10.1021/ed078p1244.

[106] S. Arumugam, M. Clarke Miller, J. Maliekal, P. J. Bates, J. O. Trent, and A. N. Lane, 'Solution structure of the RBD1,2 domains from human nucleolin', *J. Biomol. NMR*, vol. 47, no. 1, pp. 79–83, May 2010, doi: 10.1007/s10858-010-9412-1.

[107] J. Y. Park *et al.*, 'Gemcitabine-Incorporated G-Quadruplex Aptamer for Targeted Drug Delivery into Pancreas Cancer', *Mol. Ther. - Nucleic Acids*, vol. 12, pp. 543–553, Sep. 2018, doi: 10.1016/j.omtn.2018.06.003.

[108] J. Mergny and L. Lacroix, 'UV Melting of G-Quadruplexes', *Curr. Protoc. Nucleic Acid Chem.*, vol. 37, no. 1, pp. 1–15, Jun. 2009, doi: 10.1002/0471142700.nc1701s37.

[109] D. Renčiuk, J. Zhou, L. Beaurepaire, A. Guédin, A. Bourdoncle, and J.-L. Mergny, 'A FRET-based screening assay for nucleic acid ligands', *Methods*, vol. 57, no. 1, pp. 122–128, May 2012, doi: 10.1016/j.ymeth.2012.03.020.

[110] J. Figueiredo *et al.*, 'AS1411 derivatives as carriers of G-quadruplex ligands for cervical cancer cells', *Int. J. Pharm.*, vol. 568, p. 118511, Sep. 2019, doi: 10.1016/j.ijpharm.2019.118511.

[111] J. Carvalho *et al.*, 'Aptamer-based Targeted Delivery of a G-quadruplex Ligand in Cervical Cancer Cells', *Sci. Rep.*, vol. 9, no. 1, pp. 1–12, Dec. 2019, doi: 10.1038/s41598-019-44388-9.

[112] E. Tosoni *et al.*, 'Nucleolin stabilizes G-quadruplex structures folded by the LTR promoter and silences HIV-1 viral transcription', *Nucleic Acids Res.*, vol. 43, no. 18, pp. 8884–8897, Oct. 2015, doi: 10.1093/nar/gkv897.

[113] S. Soundararajan, W. Chen, E. K. Spicer, N. Courtenay-Luck, and D. J. Fernandes, 'The Nucleolin Targeting Aptamer AS1411 Destabilizes Bcl-2 Messenger RNA in Human Breast Cancer Cells', *Cancer Res.*, vol. 68, no. 7, pp. 2358–2365, Apr. 2008, doi: 10.1158/0008-5472.CAN-07-5723.

[114] P. J. Bates, J. B. Kahlon, S. D. Thomas, J. O. Trent, and D. M. Miller, 'Antiproliferative activity of G-rich oligonucleotides correlates with protein binding', *J. Biol. Chem.*, vol. 274, no. 37, pp. 26369–26377, Sep. 1999, doi: 10.1074/jbc.274.37.26369.

[115] R. Chapanian *et al.*, 'Enhancement of biological reactions on cell surfaces via macromolecular crowding', *Nat. Commun.*, vol. 5, Aug. 2014, doi: 10.1038/ncomms5683.

[116] E. Heyduk and T. Heyduk, 'Nucleic Acid-Based Fluorescence Sensors for Detecting Proteins', *Anal. Chem.*, vol. 77, no. 4, pp. 1147–1156, Feb. 2005, doi: 10.1021/ac0487449.

[117] S. Centi, L. Bonel Sanmartin, S. Tombelli, I. Palchetti, and M. Mascini, 'Detection of C Reactive Protein (CRP) in Serum by an Electrochemical Aptamer-Based Sandwich Assay', *Electroanalysis*, vol. 21, no. 11, pp. 1309–1315, Jun. 2009, doi: 10.1002/elan.200804560.

Appendices

Appendix A

P54. G-QUADRUPLEX APTAMER BEACONS FOR THE DETECTION OF NUCLEOLIN

André Miranda [1(*)], Tiago Santos [1], Josué Carvalho [1], Virgínia Chu [2], João A. Conde [2,3], Carla Cruz [1(*)]
[1] CICS-UBI – Centro de Investigação em Ciências da Saúde, Universidade da Beira Interior, Covilhã, Portugal; [2] INESC Microsistemas e Nanotecnologias and IN-Institute of Nanoscience and Nanotechnology, Lisbon, Portugal; [3] Department of Bioengineering, Instituto Superior Técnico, Technical University of Lisbon, Lisbon, Portugal.
[(*)] Email: carlacruz@fcsaude.ubi.pt; andre.miranda@ubi.pt

ABSTRACT

Nucleolin is a cancer-selective target because it is found preferentially in cancer cells, namely in cytoplasm and particularly on the cell surface, and mediates functions that are essential for cancer cell survival. Several studies reported the overexpression of cell surface nucleolin on prostate cancer cell lines. Also, nucleolin binds specifically G-rich quadruplex (G4) sequences, namely DNA G4 structures typically with 15 to 30 nucleotides long. DNA G4 aptamers, like AS1411, can be modified to incorporate a fluorophore and quencher pair, acting as a molecular beacon to detect its target, the protein nucleolin. In absence of nucleolin, the molecular beacon forms a stem-loop structure that keeps the fluorophore so close to the quencher that the donor fluorescence emission is not observed due to FRET phenomena. When the molecular beacon recognizes nucleolin, it is prompted to undergo a conformational change, separating the fluorophore from the quencher and restoring fluorescence.

In this study we presented two molecular beacons, derivatives of aptamer AS1411, for detecting nucleolin. The circular dichroism studies indicated that these molecular beacons formed parallel G4 structures. FRET-melting experiments revealed specific recognition by the molecular beacons and a concentration-dependent stabilization of the beacons G4 structures, evidencing strong interaction. Finally, the cellular uptake and localization of molecular beacons was assessed in PC-3 and PNT1A cell lines, further demonstrating the ability of the beacons to recognize and bind cell surface nucleolin.

Acknowledgements: C. Cruz acknowledges the FCT project reference MIT-EXPL/BIO/0008/2017.

Keywords: Nucleolin, G-quadruplex, Aptamer Beacons, Prostate Cancer.

G-Quadruplex Aptamer Beacons for the Detection of Nucleolin

André Miranda[1(*)], Tiago Santos[1], Josué Carvalho[1], Virgínia Chu[2], João P. Conde[2,3], Carla Cruz[1(*)]

[1] CICS-UBI – Centro de Investigação em Ciências da Saúde, Universidade da Beira Interior, Covilhã, Portugal;
[2] INESC Microsystems and Nanotechnologies and IN-Institute of Nanoscience and Nanotechnology, Lisbon, Portugal;
[3] Department of Bioengineering, Instituto Superior Técnico, Technical University of Lisbon, Lisbon, Portugal;
[(*)] *Email:* carlacruz@fcsaude.ubi.pt; andre.miranda@ubi.pt

Introduction

- Nucleolin (NCL) mediates functions that are essential for cancer cell survival and it is reported like a cancer-selective target. In prostate cancer, NCL is overexpressed in cell surface;
- Moreover, NCL binds specifically G-rich quadruplex (G4) sequences, namely DNA G4 structures. These aptamers, like AS1411, can be modified to incorporate a fluorophore and quencher pair acting as a molecular beacon to detect its target;
- In absence of NCL, FRET phenomena is not observed due to stem-loop structures, but can be re-established when G4 binds to its target;
- In this study we will present and evaluate two molecular beacons (AS1411N5 and AS1411N6), derivatives of aptamer AS1411, for detecting NCL.

Methodology

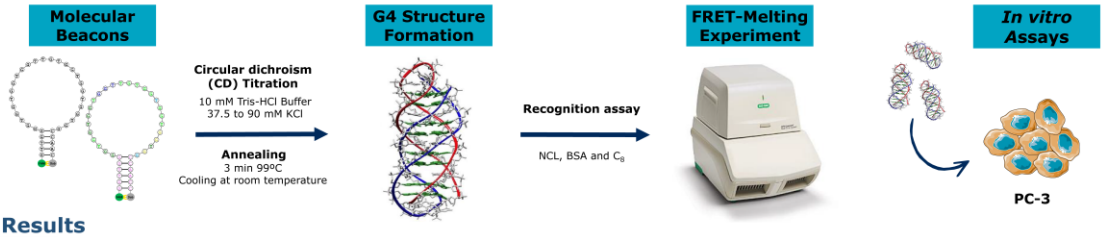

Results

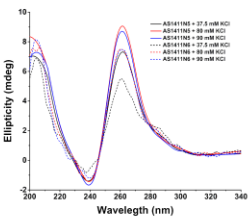

Fig. 1 – CD titration spectra of AS1411 derivatives: AS1411N5 (A) and AS1411N6 (B).

Table 1. Melting temperatures (T_m) of beacons by Circular Dichroism.

AS1411N5		AS1411N6	
[KCl]	T_m (ºC)	[KCl]	T_m (ºC)
80 mM KCl	49.32	80 mM KCl	48.49
90 mM KCl	50.38	90 mM KCl	49.40

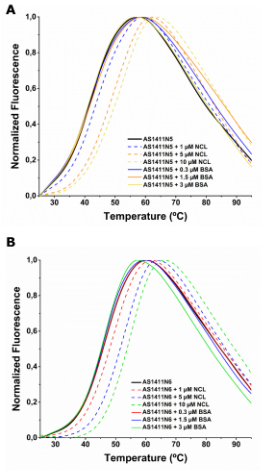

Fig. 2 – FRET melting curves of (A) AS1411N5 and (B) AS1411N6 to NCL and Bovine Serum Albumin (BSA).

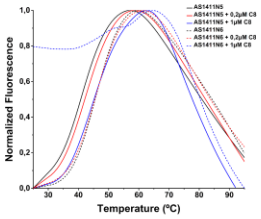

Fig. 3 – FRET melting curves of AS1411N5 and AS1411N6 in presence of compound C_8 at two concentrations.

Table 2. NCL- and C_8-induced thermal stabilization (ΔT_m) measured by FRET melting experiments.

	AS1411N5	AS1411N6
[ ] (µM)	ΔT_m (ºC)	ΔT_m (ºC)
-----	41.46	46.18
1 µM NCL	2.46	2,29
5 µM NCL	7.42	5,91
10 µM NCL	9.17	7.99
0.3 µM BSA	-0.14	0.05
1.5 µM BSA	0.35	-0.4
3 µM BSA	-0.18	-0.26
0.2 µM C_8	0.88	-0.44
1 µM C_8	3.89	0.33 13.41

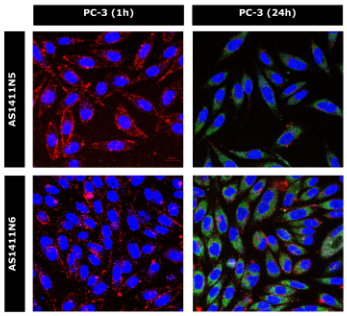

Fig. 4 – Confocal Laser Scanning Microscopy (CLSM) images of PC-3 at different time incubation with G-quadruplex beacons (*Blue channel*: nucleus; *Red channel*: nucleolin; *Green channel*: molecular beacons).

Conclusions

- AS1411N5 and AS1411N6 beacons formed parallel G4 conformation as shown in CD spectra, with positive and negative bands at 260 nm and 240 nm;
- NCL and C_8 ligand, at 10µM and 1µM concentrations, interacted and had a stabilization effect on AS1411N5 and AS1411N6 beacons, increasing their melting temperature;
- The experiments with BSA suggested that AS1411N5 and AS1411N6 beacons are selective to NCL, since no stabilization effect observed in the presence of the protein;
- *In vitro* assays demonstrated that aptamer beacons, after 24h of incubation, internalized prostate cancer cells.

Acknowledgements

C. Cruz acknowledges the FCT project reference MIT-EXPL/BIO/0008/2017

Appendix B

AS1411 Derived Molecular Beacon to Nucleolin Detection

André Miranda[1*]; Josué Carvalho[1]; Tiago Santos[1]; Virgínia Chu[2]; João P. Conde[2,3]; Carla Cruz[1*]
[1] CICS-UBI – Centro de Investigação em Ciências da Saúde, Universidade da Beira Interior, Covilhã, Portugal;
[2] INESC Microsistemas e Nanotecnologias and IN-Institute of Nanoscience and Nanotechnology, Lisbon, Portugal;
[3] Department of Bioengineering, Instituto Superior Técnico, University of Lisbon, Lisbon, Portugal;
[*] *Email:* carlacruz@fcsaude.ubi.pt; andre.miranda@ubi.pt

Nucleolin is a cancer-selective target as it is found preferentially in cancer cells, particularly on the cell surface, and mediates functions that are essential for cancer cell survival and proliferation. Studies reported the overexpression of cell surface nucleolin on prostate cancer cell lines. Also, nucleolin binds specifically G-rich sequences, namely DNA G-quadruplex (G4) structures typically with 15-30 nucleotides long. DNA G4 aptamers, like AS1411, can be modified to incorporate a fluorophore and quencher pair, acting as a molecular beacon to detect its target, nucleolin. In absence of nucleolin, the molecular beacon forms a stem-loop structure that keeps the fluorophore so close to the quencher that the donor fluorescence emission is not observed due to FRET phenomena. When the molecular beacon recognizes nucleolin, it undergoes a conformational change, separating the fluorophore from the quencher and restoring emission. The main objective of this work is characterizing all biophysical parameters of molecular beacon, for its posterior immobilization on a sensor chip for detection of nucleolin.

In this study we present a molecular beacon, derivative of aptamer AS1411, capable of detecting nucleolin. To characterize biophysical parameters, we use several techniques like Circular Dichroism (CD), Nuclear Magnetic Resonance (NMR), FRET-melting and Fluorometric assays. To assess localization and ability of molecular beacons to recognize and bind cell-surface nucleolin, we resorted to PC-3 and PNT1A cell lines.

CD indicated that this molecular beacon forms a parallel G4 structure. This result is supported by NMR that further suggests a single G4 conformation, unlike its precursor AS1411, which is polymorphic. FRET-melting experiments revealed specific recognition by the molecular beacon and a concentration-dependent stabilization of its G4 structure, evidencing interaction with nucleolin. Furthermore, to quantify the target-beacon affinity, we resorted to a fluorometric assay, that indicated low dissociation constant values in the nM range. Finally, cell lines showed recognition and binding of AS1411 derivative to cell-surface nucleolin.

With these preliminary experiments, we can have biophysical information about aptamer beacon, which is important for a successful immobilization on the sensor. The main conclusion of this work is the specific recognition of nucleolin by the AS1411 derivative, as evidenced by KDs

cuf
Academic and Research Medical Center

Participação em Eventos Científicos

Certificado

Certifica-se que **André Filipe Rodrigues Miranda**, titular do Cartão de Cidadão com o nº de identificação **15350622**, frequentou o seguinte evento científico:

2nd Portuguese Symposium on Research and Innovations in Urology

que decorreu a **9 de Novembro de 2019**, com a duração de 9 horas, no seguinte local: Porto Business School

Carnaxide, 9 de Novembro de 2019

Cláudia Silveira

Código de Certificado: C-5da04a2092fb8

Av. do Forte, nº3 – Edifício Suécia III, Piso 2 - Carnaxide

academiacuf.up.events

Comprovativo de Emissão de Certificado Electrónico

Decreto-Lei n.º 290-D/99 e 62/2003 — European Union Directive 1999/93/CE

Conteúdo Programático

Uro - Oncology

Interactive learning session with lwcturers on how to market my research

Moderated Posters

Research by university students in urology field

Innovative technologies in surgery

Appendix C

P9. MOLECULAR BEACON DERIVED FROM AS1411 FOR NUCLEOLIN DETECTION

AUTHORS: Miranda, A. [1], Santos, T. [1], Carvalho, J. [1], Chu, V. [2], Conde, JP. [2,3], Cruz, C. [1]

PRESENTER: André Filipe Rodrigues Miranda

AFFILIATION(S):

[1] CICS- UBI, Health Sciences Research Centre, University of Beira Interior, Covilhã, Portugal

[2] INESC, Microsistemas e Nanotecnologias and IN-Institute of Nanoscience and Nanotechnology, Lisboa, Portugal

[3] Department of Bioengineering, Instituto Superior Téc nico, University of Lisboa, Lisboa, Portugal;

ABSTRACT

Nucleolin is a cancer-selective target because it is found preferentially in cancer cells, particularly on the cell surface, and mediates functions that are essential for cell survival. Studies reported the overexpression of cell surface nucleolin on prostate cancer cell lines. Also, nucleolin binds specifically G-rich sequences, namely DNA G-quadruplex (G4) structures typically with 15-30 nucleotides long. DNA G4 aptamers, like AS1411, can be modified to incorporate a fluorophore and quencher pair, acting as a molecular beacon to detect its target, nucleolin. In absence of nucleolin, the molecular beacon forms a stem-loop structure that keeps the fluorophore so close to the quencher that the donor fluorescence emission is not observed due to FRET phenomena. When the molecular beacon recognizes nucleolin, is prompted to undergo a conformational change, separating the fluorophore from the quencher and restoring fluorescence. In this study we presented a molecular beacon, derivative of aptamer AS1411, capable of detecting nucleolin. Circular dichroism indicated that this molecular beacon forms a parallel G4 structure. This result is supported by Nuclear Magnetic Resonance that further suggests a single G4 conformation, unlike its precursor AS1411, which is polymorphic. FRET-melting experiments revealed specific recognition by the molecular beacon and a concentration-dependent stabilization of the beacon G4 structure, evidencing interaction with nucleolin. Furthermore, to quantify the target-beacon affinity, through the dissociation constant, we resorted to a fluorometric assay. Finally, the cellular uptake and localization of molecular beacons were assessed in PC-3 and PNT1A cell lines, further demonstrating the ability of the beacons to recognize and bind cell-surface nucleolin.

Acknowledgements: The authors acknowledge FCT project reference MIT-EXPL/BIO/0008/2017.

Molecular Beacon Derived From AS1411 to Nucleolin Detection

Miranda, A. [1*]; **Santos, T.** [1]; **Carvalho, J.** [1]; **Chu, V.** [2]; **Conde, JP.** [2,3]; **Cruz, C.** [1*]

[1] CICS-UBI – Centro de Investigação em Ciências da Saúde, Universidade da Beira Interior, Covilhã, Portugal;
[2] INESC Microsystems and Nanotechnologies and IN-Institute of Nanoscience and Nanotechnology, Lisbon, Portugal;
[3] Department of Bioengineering, Instituto Superior Técnico, University of Lisbon, Lisbon, Portugal;
*Email: carlacruz@fcsaude.ubi.pt; andre.miranda@ubi.pt

Introduction

- Nucleolin (NCL) mediates functions that are essential for cancer cell survival and it is reported like a cancer-selective target. In prostate cancer, NCL is overexpressed in cell surface;
- Moreover, NCL binds specifically G-rich sequences, namely DNA G-quadruplex (G4) structures. DNA G4 aptamers, like AS1411, can be modified to incorporate a fluorophore and quencher pair acting as a molecular beacon to detect its target;
- In absence of NCL, FRET phenomena is not observed due to stem-loop structures, but can be re-established when G4 binds to its target;
- In this study we will present and evaluate a molecular beacon, called AS1411N5, derivative of aptamer AS1411 for detecting NCL.

Methodology

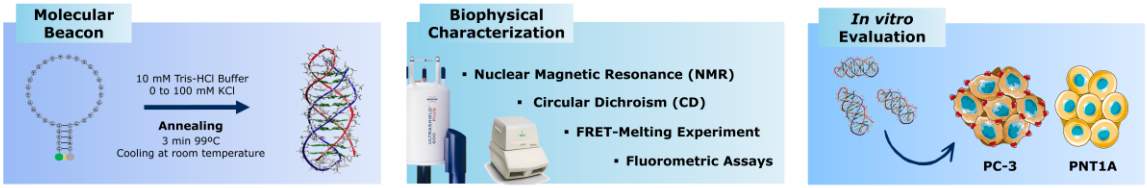

Results

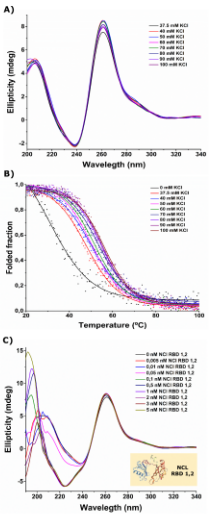

Fig. 1 – CD titration spectra of AS1411N5 (A) and CD melting assays (B). Interaction studies of NCL-AS1411N5 (C).

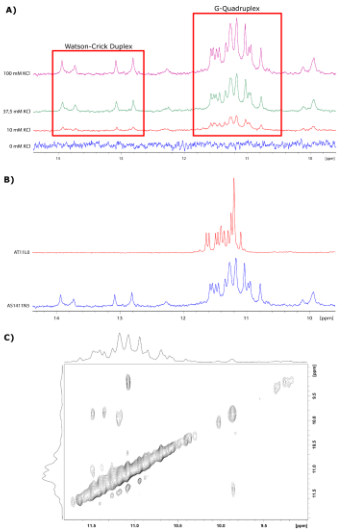

Fig. 2 – NMR titration spectra of molecular beacon (A). Comparison between AS1411N5 and AT11L0 suggest that beacon have a single conformation (B). 2D NOESY spectrum showing G4 imino protons (C).

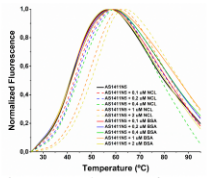

Fig. 3 – FRET–melting curves of AS1411N5 to NCL and Bovine Serum Albumin (BSA).

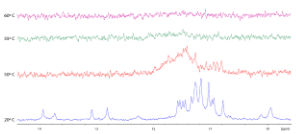

Fig. 4 – ^{1}H NMR spectra of AS1411N5 at different temperatures.

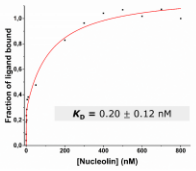

Fig. 5 – Quantification of target-beacon affinity, through the determination of dissociation constant (K_D) by fluorometric assay.

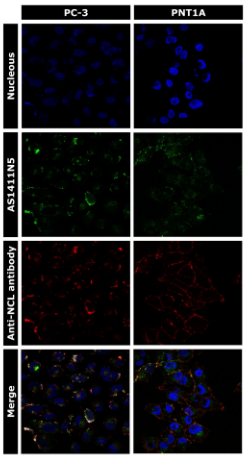

Fig. 6 – Confocal Laser Scanning Microscopy (CLSM) images of PC-3 and PNT1A cell lines with AS1411N5 at incubation of 24h.

Conclusions

- AS1411N5 formed a parallel G4 conformation as shown in CD spectra, with positive and negative bands at 260 nm and 240 nm;
- NMR spectra of AS1411N5 did not show polymorphism, suggesting that have a single conformation, allowing to determine and define its structure;
- FRET-melting experiments suggested that AS1411N5 recognize NCL instead of BSA;
- High affinity to NCL by AS1411N5, as evidenced by K_D determination and co-localization evidenced *in vitro* assays;
- AS1411N5 revealed to be a potential candidate to NCL detection on a microfluidic system.

Acknowledgements
The authors acknowledge the FCT project reference MIT-EXPL/BIO/0008/2017